Simulation of DBD plasma actuators, and nanoparticle-plasma interactions in argon-hydrogen CCP RF discharges

A DISSERTATION

SUBMITTED TO THE FACULTY OF THE GRADUATE SCHOOL

OF THE UNIVERSITY OF MINNESOTA

BY

Meenakshi Mamunuru

IN PARTIAL FULFILLMENT OF THE REQUIREMENTS

FOR THE DEGREE OF

Doctor of Philosophy

Uwe R Kortshagen

August, 2014

Acknowledgements

This work marks an end to a journey I started in 2007, and when I look back, I am filled with gratitude for the grad school experience that enriched me in every way. I would firstly like to thank my advisor, Dr. Uwe Kortshagen for his endless patience with me, and for not giving up hope on me even as I doubted myself. I learnt from him the importance of asking the right questions, and not losing sight of them while attempting to answer them. His articulation and clarity of expression are things I have tried to imbibe over these years. Thank you, Dr. Kortshagen for giving me an opportunity to get this education.

I would like to thank my committee members: Dr. Douglas Ernie for the invaluable discussions and inputs to my work; Dr. Terry Simon for guidance in the plasma actuator work, and for being an exemplary researcher; and Dr. Steven Girshick for teaching me kinetic theory, that made this work possible. The people at MENet and Minnesota Supercomputing Institute have provided resources, and support, and I appreciate that. I had the opportunity to be in the company of, and work with wonderful colleagues in the HTPL and I thank everyone of them. Special thanks to Juan Pablo Trelles, Marco Gatti, Federico Galli, Venkat Raman, Pulkit Agarwal, Rebecca Anthony, David Rowe, Nic Kramer, and Narula Bilik.

I can't be thankful enough for the friends I made here; Rohini BC, Aditi Arur,

Durbha, Thavil, Ranga, Coma, Pulkit, Thaseem - the time I spent with them is unforgettable and precious. My room mates over the years, Parul Varma, Rashmi Prasad, and Annu Kath made the apartment a home. I am grateful for the love and kindness that Jagdish Uncle, Lakshmi Aunty, Teja and Sridevi Aunty have shown me. They treated me like one of their own.

My extended family and in-laws are incredible people who have been a solid part of my support system. I thank my sister Madhu who means the world to me, and though seven years younger, inspires me with her qualities. I'd be nothing without the sacrifices made by my mother, father, and grandmother; their unconditional love, and the values they have stood for and tried to instilled in me. I can't believe how lucky I am to be married to Sree. His positivity, calmness, enthusiasm for adventure, and above all, his love are invaluable to me, and have kept my spirits up during the hardest of times.

Dedication

To my mother Padma Shankar, and my father Mamunuru Shankar

Abstract

The focus of this work is modeling and simulation of low temperature plasma discharges (LTPs). The first part of the thesis consists of the study of dielectric barrier (DBD) plasma actuators. Use of DBD plasma actuators on airfoil surfaces is a promising method for increasing airfoil efficiency. Actuators produce a surface discharge that causes time averaged thrust in the neutral gas. The thrust modifies the boundary layer properties of the flow and prevents the occurrence of separation bubbles. In simulating the working of an actuator, the focus is on the spatial characteristics of the thrust produced by the discharge over very short time and space scales. The results provide an understanding of the causes of thrust, and the basic principles behind the actuator operation.

The second part of this work focusses on low pressure plasma discharges used for silicon nanoparticle synthesis. When reactive semiconductor precursor gases are passed through capacitively coupled plasma (CCP) radio frequency (RF) reactors, nano sized particles are formed. When the reactors are operated at high enough powers, a very high fraction of the nanoparticles are crystallized in the chamber. Nanoparticle crystallization in plasma is a very complex process and not yet fully understood. It can be inferred from experiments that bulk and surface processes initiated due to energetic ion impaction of the nanoparticles are responsible for reordering of silicon atoms, causing crystallization. Therefore, study of plasma-particle interactions is the first step towards understanding how particles are crystallized. The specific focus of this work is to investigate the experimental evidence that hydrogen gas presence in argon discharges used for silicon nanocrystal synthesis, leads to a superior quality of nanocrystals. Influence of hydrogen gas on plasma composition and discharge characteristics is studied. Via Monte Carlo

simulation, distribution of ion energy impacting particles surface is studied. It is seen that hydrogen ions cause a reduction in particle floating potential, thereby lowering the ion impaction energies. The hydrogen ion current is also effective in delivering increased number of atomic H radicals to the particle surface, which are known to promote particle crystallization. The work therefore sheds light on the ways in which trace amount of hydrogen gas participates in silicon nanoparticle crystallization in argon silane plasma.

Contents

Acknowledgements **i**

Dedication **iii**

Abstract **iv**

List of Tables **ix**

List of Figures **x**

Nomenclature **1**

1 Introduction **7**

1.1 Plasma 7

1.1.1 Applications of LTPs 9

1.2 Motivation 10

1.3 Outline of thesis 12

2 Basic equations of plasma discharge **13**

2.1 Governing equations 13

2.1.1 Fluid approximation 15

2.1.2 Nonmagnetized discharges 16

2.1.3 Atmospheric pressure LTPs 17
2.1.4 Zero D models of low pressure discharges 19
2.1.5 Particle in Cell Monte Carlo simulations 21

3 Simulation of Plasma Actuator **23**
3.1 Introduction 23
3.2 Description of Model 29
3.2.1 System of Equations 29
3.2.2 Boundary Conditions 32
3.3 Simulation results 33
3.4 Conclusion 43

4 Volume averaged simulations of argon-hydrogen CCP RF dusty plasmas **45**
4.1 Introduction 45
4.2 Argon hydrogen plasma chemistry 46
4.3 Description of Model 50
4.3.1 Bulk plasma 51
4.3.2 Plasma Sheaths 53
4.3.3 Conduction current at the plasma-sheath boundary 55
4.3.4 Electron heating 58
4.3.5 Electron power balance 59
4.3.6 Total power balance 60
4.3.7 Current to nanoparticles 60
4.3.8 Electron energy distribution 60
4.4 Simulation results 61
4.4.1 Effect of hydrogen addition 61

4.4.2 Effect of increasing nanoparticle density 63
4.4.3 Comparison with experiments 68
4.5 Conclusion 77

5 Particle Charging and Ion Impaction in $Ar - H_2$ Dusty Plasmas 78

5.1 Introduction 78
5.1.1 Motivation 79
5.1.2 Background 82
5.2 Monte Carlo simulations 83
5.2.1 Collision tracking 85
5.2.2 Ion-neutral Collisions 86
5.3 Results and discussion 88
5.3.1 PIC-MC simulations: Pure argon discharge 88
5.3.2 PIC-MC simulations: Argon hydrogen discharge 90
5.3.3 Analytical model 96
5.4 Conclusion and scope 109

6 Conclusion and Discussion 110

References 112

List of Tables

3.1 Boundary conditions for continuity equations 32

3.2 Boundary conditions for Poisson's equation 33

4.1 List of ion - atom/molecule reactions 47

4.2 Plasma discharge parameters for simulation and experiment 74

5.1 Normalized ion current to particle in pure argon discharge 90

List of Figures

1.1 Schematics of typical dielectric barrier discharges. 9

3.1 Schematic of a basic plasma actuator. 24

3.2 Schematic of the working of an actuator. 24

3.3 Schematic depicting the resultant force on an airfoil immersed in a flowing fluid. 25

3.4 Streamlines of flow over an airfoil, depicting no separation. 26

3.5 Effect of plasma actuator on boundary layer separation seen in flow visualization over an airfoil at 16 degrees angle of attack: $Re = 158 \times 10^3$ [1]. 26

3.6 A high speed photograph showing the difference in the spatial structure of discharge caused by negative half cycle of voltage (above) and positive half cycle (below)[2]. The top view of the actuator is seen. 28

3.7 Schematic of a the simulation domain. 30

3.8 Boundaries of the simulation domain. Boundary conditions given by numbers are given in Tables 3.1 and 3.8. 32

3.9 Positive ion density and potential of a discharge during the application of a positive pulse (seen in the inset), denoting the propagation of a cathode directed streamer. 35

3.10 Positive ion density and potential of a discharge during the application of a negative pulse (seen in the inset), denoting the propagation of a anode directed streamer. 36
3.11 Streamwise direction force per unit volume for positive and negative applied voltage pulses at the exposed electrode, seen in Figure 3.9 and Figure 3.10, respectively. 38
3.12 Normal direction force per unit volume for positive and negative applied voltage pulses at the exposed electrode, seen in Figure 3.9 and Figure 3.10, respectively. 39
3.13 Component of the electric field in the direction parallel to the actuator surface during the application of, (a) positive pulse, and (b) negative pulse seen in figures 3.9 and 3.10, respectively. 41
3.14 Component of the electric field in the normal direction to the actuator surface during the application of, (a) positive pulse, and (b) negative pulse seen in figures 3.9 and 3.10, respectively. 42
4.1 Cross sections for electron interaction with ground state argon atoms. . 47
4.2 Cross sections for electron impact ionization, and momentum transfer of ground state hydrogen molecules. 48
4.3 Cross sections for electron excitation of ground state hydrogen molecules. 48
4.4 Cross sections for electron impact ionization, and elastic scattering of ground state H atoms. 49
4.5 Cross sections for electron excitation of ground state H atoms. 49
4.6 Schematic of CCP RF discharge chamber. 50
4.7 Plasma density profiles in different pressure regimes, compared to the profile assumed in the volume averaged simulation. 51
4.8 Plasma density profile as assumed in the global model. 52

4.9 Schematic of an RF sheath. 54
4.10 Plasma density as a function of $H_2 : Ar$ ratio. Power absorbed: 3 W, nanoparticle density: $10^3\ cm^{-3}$. 64
4.11 Ion composition of plasma as a function of $H_2 : Ar$ ratio. Power absorbed: 3 W, nanoparticle density: $10^3\ cm^{-3}$. 65
4.12 Electron energy distribution at different fractions of H_2 gas. Power absorbed: 3 W, nanoparticle density: $10^3\ cm^{-3}$. 66
4.13 Electron energy distributions shown in Figure 4.12 zoomed at lower energies. 67
4.14 Particle floating potential as a function of H_2 fraction. Power absorbed: 3 W, nanoparticle density: $10^3\ cm^{-3}$. 68
4.15 Fractions of ion species in the ion current to nanoparticles at (a) 1 percent H_2, and at (b) 4 percent H_2, in argon. Discharge pressure: 50 Pa, power absorbed: 3 W, nanoparticle density: $10^3 cm^{-3}$. 69
4.16 Plasma density as a function of nanoparticle density. Pressure: 50 Pa, Power absorbed: 3 W. 70
4.17 Ion composition of plasma as a function of nanoparticle density. Pressure: 50 Pa, Power absorbed: 3 W. 71
4.18 EEDF's at different nanoparticle densities for two different concentrations of H_2. 72
4.19 EEDF's in Figure 4.18 zoomed in the low energy region. 73
4.20 Particle potential as a function of nanoparticle density. Pressure: 50 Pa, Power absorbed: 3 W. 74
4.21 Fractions of ion species in the ion current to nanoparticles at nanoparticle density of (a) $10^3\ cm^{-3}$ and, (b) $1.7 \times 10^7\ cm^{-3}$, in argon. Discharge pressure: 50 Pa, power absorbed: 3 W, 1 percent H_2 concentration. . . . 75

4.22 The variation of plasma density with H_2 concentration in Ar gas. 76
4.23 The variation of EEDF with H_2 concentration in Ar gas. (a) Simulation, (b) Experiment. 76
5.1 A schematic of the spherically symmetric one dimensional domain used for MC simulations. 84
5.2 Figure describing collision tracking in PIC MC simulations. 86
5.3 Cross sections for ion natural collisions between argon and Ar^+ ions and argon and H_3^+ ions. 87
5.4 Floating potential versus pressure for a $R_p = 500nm$ particle, for a discharge containing $n_{Ar^+} = 1 \times 10^{16}\ m^{-3}$, $T_e = 3.4$ eV. 91
5.5 Steady state ion flux versus pressure for a $R_p = 500nm$ particle, for a discharge containing $n_{Ar^+} = 1 \times 10^{16}\ m^{-3}$, $T_e = 3.4$ eV. 91
5.6 Ion energy distributions, and distributions of energy associated with radial and tangential ion velocity components for $500nm$ particle a pure argon discharge, $n_{Ar^+} = 1 \times 10^{16}\ m^{-3}$, $T_e = 3.4$ eV. 92
5.7 Histogram of collisions in the capture sphere undergone by ions constituting flux to the nanoparticle surface when only the charge exchange collision are present (column 1), only elastic scattering is present (column 2) and both are present. $500nm$ particle for the discharge containing $n_{Ar^+} = 1 \times 10^{16}\ m^{-3}$, $T_e = 3.4$ eV. 93
5.8 Ion energy distribution in pure argon discharge when only the charge exchange collisions are considered (left column) and only when elastic scattering is considered (right column). 94
5.9 Floating potential versus pressure for a $R_p = 500nm$ particle, for a discharge containing $n_{Ar^+} = 1 \times 10^{16}\ m^{-3}$, $T_e = 3.4$ eV. 95

5.10 Steady state floating potential for a $500nm$ particle. $n_{Ar^+} = 5{\times}10^{15}\ m^{-3}$, and $n_{H_3^+} = 5 \times 10^{15}\ m^{-3}$, $T_e = 3.4$ eV. 97
5.11 Steady state floating potential comparison for pure Ar discharge in Figure 5.4 , and $Ar - H_2$ discharge. $R_p = 500nm$ particle. $n_{Ar^+} = 5{\times}10^{15}\ m^{-3}$, and $n_{H_3^+} = 5 \times 10^{15}\ m^{-3}$, $T_e = 3.4$ eV. 98
5.12 Steady state ion flux for a , $R_p = 500nm$ particle. $n_{Ar^+} = 5 \times 10^{15}\ m^{-3}$, and $n_{H_3^+} = 5 \times 10^{15}\ m^{-3}$, $T_e = 3.4$ eV. 99
5.13 Ion energy distributions for each type of ion for a $500nm$ particle, $n_{Ar^+} = 5 \times 10^{15}\ m^{-3}$, $n_{H_3^+} = 5 \times 10^{15}\ m^{-3}$,$T_e = 3.4$ eV. 100
5.14 Histogram of collisions undergone by ions forming the current, inside the capture sphere for a $500nm$ particle. $n_{Ar^+} = 5 \times 10^{15}\ m^{-3}$, and $n_{H_3^+} = 5 \times 10^{15}\ m^{-3}$, $T_e = 3.4$ eV. 101
5.15 Comparison of particle potential obtained through PIC-MC simulations and analytical model for $500nm$ particle. $n_{Ar^+} = 1 \times 10^{16}\ m^{-3}$, $T_e = 3.4$ eV. 105
5.16 Comparison of steady state ion flux obtained through PIC-MC simulations and analytical model for $500nm$ particle. $n_{Ar^+} = 1 \times 10^{16}\ m^{-3}$, $T_e = 3.4$ eV. 106
5.17 Comparison of particle potential obtained through PIC-MC simulations and analytical model for $500nm$ particle. $n_{Ar^+} = 5 \times 10^{15}\ m^{-3}$, and $n_{H_3^+} = 5 \times 10^{15}\ m^{-3}$,$T_e = 3.4$ eV. 107
5.18 Comparison of steady state ion flux obtained through PIC-MC simulations and analytical model for $500nm$ particle. $n_{Ar^+} = 1 \times 10^{16}\ m^{-3}$, and $n_{H_3^+} = 5 \times 10^{15}\ m^{-3}$, $T_e = 3.4$ eV. 108

Nomenclature

α Townsend ionization coefficient for electrons $[m^{-1}]$

$\bar{P_{ohm}}$ Ohmic heating of electrons in plasma bulk [W]

$\bar{P}_{abs}$ Total power absorbed by plasma [W]

$\bar{P}_{stoc}$ Power absorbed by electrons due to stochastic heating [W]

$\bar{V}$ Time averaged potential drop in sheath [V]

ϵ_0 Permittivity of free space [F/m]

η Townsend attachment coefficient for electrons $[m^{-1}]$

Γ Flux $[m^{-2}s^{-1}]$

γ Secondary electron emission coefficient

κ_T Thermal conductivity [W/mK]

λ_D Debye length [m]

λ_i Mean free path [m]

λ_{RMS} Root mean square displacement [m]

π Pressure tensor [N/m]

B Magnetic field [T]

E Electric field [V/m]

F Force [N/m]

H Magnetic field strength [A/m]

J Current density $[A/m^2]$

q Heat flow vector $[W/m^2]$

r Position vector [m]

u Average velocity [m/s]

v Velocity vector [m/s]

μ_0 Permeability of free space [H/m]

μ_i Ion mobility $[m^2/V-s]$

ν_m Momentum transfer collision frequency $[s^{-1}]$

ν_{iz}, ν_{ex} Ionization and excitation collision frequency of electrons $[s^{-1}]$

$\nu_{loss-np,i}$ Frequency of ion loss to nanoparticles $[s^{-1}]$

ω Frequency of applied voltage [rad/s]

ϕ Electrostatic potential [V]

ρ Charge density $[C/m^3]$

σ Accumulated charge on surface [C]

σ_{dc} DC plasma conductivity [S/m]

τ Ion energy relaxation time [s]

$\varepsilon_{e,n}$ Energy loss due to electron neutral collisions [eV]

$\varepsilon_{i,w}$ Energy carried by every ion to the wall [eV]

$\varepsilon_{iz}, \varepsilon_{ex}$ Energies associated with ionization and electronic excitation processes of atoms and molecules [eV]

A Area [m]

A_{eff} Affective area of quasineutral bulk plasma [m^2]

$B_{e,i}$ Electron-ion recombination coefficient [m^3/s]

$B_{i,n}$ Positive-negative ion recombination coefficient [m^3/s]

D, D_k, D_e Diffusivity, of ions and electrons [m^2/s]

D_a Ambipolar diffusion [m^2/s]

e Unit charge [C]

E/N Reduced electric field [Vm^2]

E_v Kinetic energy of an ion after one collision inside capture sphere [eV]

E_v^* Kinetic energy of neutral gas atoms [eV]

$E_{v,0}$ Initial kinetic energy of an ion inside capture sphere [eV]

f Distribution function

G, L Gain and loss terms in mass balance [$m^{-3}s^{-1}$]

h_L Ratio of ion sheath edge density to centerline density

I Conduction current [A]

I_e, I_i Electron and ion currents to nanoparticle [A]

$I_{i,CEC}$ 'Collision enhanced ion current' [A]

$I_{i,HYD}$ Hydrodynamic ion current [A]

$I_{i,OML}$ Orbital Motion Limited ion current [A]

J_1 Total current density $[A/m^2]$

J_i Ion current density $[A/m^2]$

K Numerical constant obtained by integrating the capture radius over Maxwellian distribution of ions

k Boltzmann constant [J/K]

k_{cx} Rate coefficient for charge transfer between ions, and neutrals $[m^3/s]$

L Characteristic length scale [m]

l Distance between electrodes in a cylindrical plasma chamber [m]

L_c Power lost by electrons due to collisions in bulk [W]

$L_{e,np}$ Electron power lost due to current to nanoparticles [W]

$L_{e,w}$ Electron power lost to walls due to flux [W]

$L_{i,w}$ Power loss due to ion flux to chamber walls [W]

$L_{t,np}$ Power loss due to electron and ion currents to plasma [W]

m Mass [kg]

m_i Ion mass [kg]

N Neutral gas density [m^{-3}]

n Number density of a species [m^{-3}]

n_e Electron density [m^{-3}]

n_e, n_k Electron, and ion density [m^{-3}]

n_p Nanoparticle density [m^{-3}]

n_s Plasma density at sheath edge [m^{-3}]

$n_{i,0}$ Ion density at the centerline of the discharge [m^{-3}]

$n_{i,s}, n_{e,s}$ Ion and electron densities at sheath edge [m^{-3}]

p Pressure [N/m]

P_{abs} Power absorbed by plasma discharge [W]

$P_{i,c=0}, P_{i,c=1}, P_{i,c>0}$ Probability that an ion performs zero, one, and more than one collisions in the capture sphere

q Unit charge [C]

R Radius of the plasma chamber [m]

R_0 Radius of capture sphere [m]

R_p Radius of nanoparticle [m]

s_m Thickness of ion sheath [m]

S_{ph} Photoionization source term [$m^{-3}s^{-1}$]

T Temperature [K]

t_c Time between two successive collisions of an ion with gas atoms [s]

T_e Electron temperature [eV]

u_B Bohm velocity [m/s]

$u_{i,s}$ Ion velocity at sheath edge [m/s]

V Volume [m^3]

V_1 Amplitude of applied voltage across sheath [V]

V_p Floating potential of nanoparticle [V]

V_{rf} Peak to peak RF voltage [V]

$v_{s,i}$ Velocity with which ions enter the sheath [m/s]

V_{sh} Wall floating potential [V]

Z_k Steady state charge on nanoparticle [C]

CCP RF Capacitively coupled plasma radio frequency

DBD Dielectric barrier discharges

LTE Local thermal equilibrium

LTP Low temperature plasma

PECVD Plasma enhanced chemical vapor deposition

Subscript k Pertaining to ions of either polarity

Subscripts i, n Pertaining to positive and negative ions

Chapter 1

Introduction

The main focus of this thesis is the study of low temperature plasma discharges including atmospheric pressure plasmas, and low pressure dusty plasmas used for nanoparticle synthesis, via simulation and analysis. In this introductory chapter, a brief description is given of low temperature plasmas and their relevance to processes technology, lighting and other uses. This is followed by a description of the discharges that are the focus of the thesis, and the motivation to study them. In the subsequent section, the outline of the thesis is explained.

1.1 Plasma

Plasmas can be loosely described as ionized gases. They consist of neutral gas, and a fraction of it dissociated into charged species such as electrons and ions. At macroscopic length scales, plasmas exhibit charge neutrality, i.e., there are as many positive charges as negative charges in the plasma volume. When plasma is in contact with a surface, the charge neutrality disappears in the vicinity of the surface. The highly mobile electrons charge up the surface negatively, creating an electric field pointing from the plasma

volume to the surface. However, the charged species in the plasma volume arrange themselves so as to shield this electric field. The order of length over which electrostatic field is shielded by the plasma is called its 'Debye length', $\lambda_D \approx \left(\epsilon_0 k T_e / n_e q^2\right)^{1/2}$ [3]. Here, ϵ_0 is the permittivity of free space, n_e is the electron number density, T_e is the electron temperature, q is the unit charge in Coulomb, and k is the Boltzmann constant. A defining property of plasmas is that $\lambda_D << L$, the characteristic length scale of the chamber; i.e., there is enough charge to shield a perturbation in the electric field within a short length of its origin [4].

Plasmas constitute the most energized and the fourth state of matter. It turns out that most of the universe is made up of plasma. Naturally occurring plasmas, due to the high energy needed to sustain them, are hard to find on earth. A few examples are lightning, and St. Elmo's fire during storms. Plasmas can be created in the laboratory, however, by ionizing gases under the influence of electro magnetic fields between electrodes.

Discharges in the laboratory can be classified into local thermal equilibrium (LTE) or non-LTE plasmas. In LTE plasmas, the charged species and the neutral gas are at thermal equilibrium with each other. These plasmas are characterized by large currents $\sim 1 - 10^5$A [5], and by temperatures between 4,000 K to 80,000 K and often occur at high pressures, where there is enough collisionality between the plasma species to attain thermal equilibrium. On the other hand, typically at low pressures, the electric field transfers energy most efficiently to electrons. The electrons reach a very high temperature, with the mean between 20,000 K to 80,000 K. Energy transfer between electrons and the heavier ions, atoms/molecules is inefficient due to collisionality, and as a result, the heavy particles remain at much lower temperature. This results in non-LTE plasma discharges. The electrons are not in thermal equilibrium with other species or even with each other. Non-LTE plasmas shall hereafter be referred to as low

temperature plasmas (LTPs).

The exception to LTPs are dielectric barrier discharges (DBD) because they can occur at room temperature at atmospheric pressure. DBDs provide the convenience of producing LTP without controlling the pressure. The schematics of typical DBD configurations is shown in Figure 1.1 [6]. When the plasma discharge occurring in the gap between the electrodes reaches the dielectric barrier, charged particles accumulate on its surface and reduce the electric field that caused the breakdown in the first place, thus extinguishing the discharge. Thus, atmospheric pressure DBDs are in fact a series of localized, short lived micro discharges. DBDs operate at low currents due to the current limiting nature of the dielectric layer. Low current implies low degree of ionization. Consequently there is low interaction between electrons and heavy particles that precludes equilibration of temperatures, giving rise to an LTP.

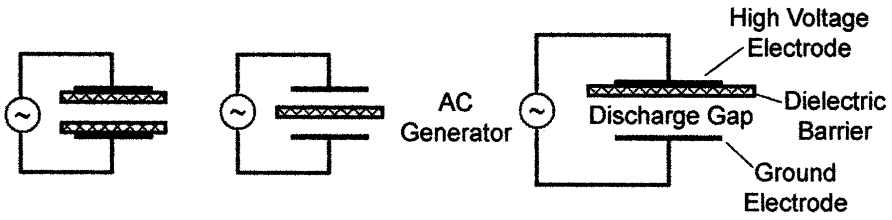

Figure 1.1: Schematics of typical dielectric barrier discharges.

1.1.1 Applications of LTPs

Owing to their wide range of controllability via operating parameters, LTPs can be tailored for many applications. LTPs have the unique ability to interact with their bounding surfaces while not causing thermal damage to them. LTPs at very low pressures are used for surface etching, plasma enhanced chemical vapor deposition and

surface treatments, and in vapor lamps. LTPs at atmospheric pressure are used for air and water treatment [7]. The property of DBDs at atmospheric pressure to spread on surfaces has led to their use in wound healing, and sterilization [8]. Under certain configurations, DBDs were seen to induce flow in the neutral gas; giving rise to DBD plasma actuators. They have been employed for active flow control over aerodynamic surfaces [9].

For most applications, it is desirable that the plasma discharge consists only of ion and electrons. However, particulate formation was seen in LTPs when reactive gases were added in the feed, or due to sputtering of material from chamber/substrate surfaces [10]. Plasmas containing particles are called dusty plasmas, while those that do not are pristine plasmas. While extensive efforts are made to eliminate particulate formation in plasmas used for etching, nanocrystal synthesis takes advantage of this very phenomenon. LTPs at very low pressures have become an attractive medium of synthesizing a variety of semiconductor nanocrystalline materials [11]. Capacitively or inductively coupled flow-through reactors are used for the gas phase synthesis of nanoparticles. A reactive precursor gas is mixed with an inert gas and passed through the plasma reactor. The precursor dissociates and coagulates to form nanosized particles. When the discharges are operated at high enough powers, the particles crystallize. A high fraction of crystals in very narrow size ranges are produced by RF plasma discharges.

1.2 Motivation

Experimental studies have shed light on the working of DBD plasma actuators. The smallest time scale phenomena in the actuator operation is that of micro discharge creation and propagation lasting over a few nanoseconds, while the largest corresponds to the response of neutral fluid to the plasma-produced thrust. The small time scale events

are best studied via simulation, providing a thorough understanding of plasma actuation. The work done in this thesis aims for that understanding, which has corroborated the findings of several groups.

The second part of the work focuses on importance of hydrogen presence in argon-silane ($Ar : SiH_4$) capacitively coupled plasma radio frequency (CCP RF) discharges used for the synthesis of hydrogen terminated silicon nanocrystals. The influence of hydrogen gas can be inferred from various experimental studies.

Kortshagen's lab has reported the highest photoluminescence quantum yield from gas phase synthesized silicon nanoparticles that are subjected to hydrogen gas in the afterglow part of the discharge [12]. Groups that have added hydrogen to the argon silane mixture in the feed gas stage, for plasma enhanced chemical vapor deposition (PECVD) have reported higher crystallinity in the deposited Si film [13]. Molecular dynamic simulations of H radical interaction with Si films during PECVD showed the role of H in crystallizing the films [14].

Hydrogen gas is released into the plasma discharge due to the dissociation of silane gas, even in the absence of external addition. It plays a role in causing particle crystallization and terminating the surface bonds [12]. However, there has been very little work done in the past with regard to gas phase synthesis of nanocrystals. Conclusions from studies of PECVD cannot be extended to gas phase synthesis of nanocrystals. The effect of hydrogen ionization in argon plasma on the nanoparticle-plasma interaction was not studied before. Hydrogen and argon ions have vastly different masses and collision characteristics. Ion flux to surfaces (in this case nanoparticle surfaces) in plasmas containing multiple species of ions is very different from a single ion case. It becomes important to determine the nanoparticle charge, current constitution and impaction energies if we want to better understand the process of nanocrystal formation.

The objectives of this thesis can be summed up as follows:

1. Simulate the working of an atmospheric pressure DBD plasma actuator and explain the cause, and the spatial and temporal nature of the thrust generated by it.

2. Study the effect of H_2 gas presence in Ar CCP RF discharge, and observe its effect on charging and energy interactions of nanoparticles with plasma.

1.3 Outline of thesis

In chapter 2 of the thesis, the system of equations governing plasma discharges are described. These equations seldom need to be solved in their most rigorous form, and depending on the specific discharge under consideration, several simplifying assumptions can be made, reducing the equations to more easily solvable forms. The assumptions pertaining to discharges simulated in the thesis and the resulting simplified equations are discussed.

Chapter 3 describes DBD plasma actuator simulations. It presents the discharge characteristics for positively and negatively pulsed electrodes and explains the mechanism of thrust generation in an actuator.

Chapter 4 describes volume averaged simulation of argon hydrogen plasma in the presence of nano sized dust. Plasma composition, electron energy distribution and nanoparticle charging are studied as a function of the operating conditions of a cylindrical CCP RF discharge chamber.

Chapter 5 describes the study of nanoparticle interaction with plasma in the presence of more than one type of ion. Ar^+ and H_3^+ ions are considered in argon gas to illustrate that the constitution of ion current, and the energy distribution functions of ions impacting the nanoparticles are dependent on pressures as well as the collision characteristics of constituent species of ions.

Chapter 2

Basic equations of plasma discharge

In this chapter, the system of basic equations required for describing a plasma discharge are discussed. In section 2.1, equations that describe the discharge most rigorously are stated. In the subsequent sections, the sets of equations used in this thesis for describing atmospheric pressure discharges, volume averaged simulations, and Monte Carlo simulations are derived from the basic equations and the simplifying assumptions made during the derivations are justified.

2.1 Governing equations

A given charged species in plasma is most accurately described by a distribution function in six dimensional phase space $f(\mathbf{r}, \mathbf{v}, t)$ of positions and velocities. The conservation equation of the distribution function is given by the Boltzmann equation.

$$\frac{\partial f}{\partial t} + \mathbf{v} \cdot \nabla_{\mathbf{r}} f + \frac{\mathbf{F}}{m} \cdot \nabla_{\mathbf{v}} f = \left(\frac{\partial f}{\partial t} \right)_c \tag{2.1}$$

In Equation 2.1, m is the mass and $\mathbf{v}$ is the velocity of the species. The right hand side of the equation keeps track of the instantaneous changes to the distribution function occurring due to very short time scale collisions. The term $\mathbf{F}$ consists of the forces acting on the charged particles. Considering that the particles are being acted on only by electric and magnetic fields, $\mathbf{E}$ and $\mathbf{B}$, the force term is expressed as the following equation (q is the unit charge):

$$\mathbf{F} = m\frac{d\mathbf{v}}{dt} = q\left[\mathbf{E}(\mathbf{r},t) + \mathbf{v}\times\mathbf{B}(\mathbf{r},t)\right] \tag{2.2}$$

The charged particles in the plasma respond to, as well as influence, the electromagnetic fields. Therefore, describing a plasma self-consistently involves the simultaneous solution of transport equations of charged particles, along with Maxwell's equations.

$$\nabla\times\mathbf{E} = -\mu_0\frac{\partial\mathbf{H}}{\partial t} \tag{2.3}$$

$$\nabla\times\mathbf{H} = \epsilon_0\frac{\partial\mathbf{E}}{\partial t} + \mathbf{J} \tag{2.4}$$

$$\epsilon_0\nabla\cdot\mathbf{E} = \rho \tag{2.5}$$

$$\mu_0\nabla\cdot\mathbf{H} = 0 \tag{2.6}$$

In the above equations, μ_0 and ϵ_0 are permeability and permittivity of free space, $\mathbf{H}$ is the magnetic field strength, $\mathbf{J}$ is the current density, and ρ is the charge density. This set of coupled equations is extremely cumbersome to solve. Thankfully, for most situations needing plasma simulations, the equations can be simplified and yet describe the physics sufficiently accurately. We shall examine a few such cases in the following sections, that are pertinent to the discharges modeled in this thesis.

2.1.1 Fluid approximation

In this section we discuss the fluid approximation of plasma, and situations where it can be applied to describe the plasma. The distribution function can be integrated over the velocity space to obtain its 'moment'. The zeroth moment would be the integration of the distribution multiplied by $1(\mathbf{n} = \int_{-\infty}^{\infty} f(\mathbf{v})d\mathbf{v})$. This yields the total number of particles in the considered volume. The first moment is the velocity averaged over the distribution ($\mathbf{u} = \int_{-\infty}^{\infty} \mathbf{v}f(\mathbf{v})d\mathbf{v}$); the second is the square of velocity averaged over the distribution, and so forth. Mean values of quantities such as density, velocity and energy are obtained from the moments of the distribution. When the Boltzmann equation is integrated this way, we obtain transport equations for the mean quantities, given by the following equations. Equation 2.7 is for mass conservation, and Equation 2.8 for momentum conservation.

$$\frac{\partial n}{\partial t} + \nabla \cdot (n\mathbf{u}) = G - L \tag{2.7}$$

$$mn\left[\frac{\partial \mathbf{u}}{\partial t} + (\mathbf{u} \cdot \nabla)\mathbf{u}\right] = qn\left(\mathbf{E} + \mathbf{u} \times \mathbf{B}\right) - \nabla \cdot \mathbf{\Pi} + f|_c \tag{2.8}$$

G and L are species gain and loss. It can be seen that in order to solve equation 2.7, knowledge of mean velocity is required. The equation for obtaining mean velocity (Eq. 2.8) requires the knowledge of the pressure tensor $\mathbf{\Pi}$, related to the mean energy of the particles. This way, we would have an infinite number of moments of the Boltzmann equation without having a closed system. It is impractical to describe the system using more than three moments; mass, momentum and energy. The equations are closed, by using the equation of state for ideal gas to relate pressure, p to number density, n via temperature, T. We assume here that the species are in *an equilibrium Maxwellian distribution.*

$$p = nkT \tag{2.9}$$

Using Equation 2.9 and multiplying the Boltzmann equation (2.1) with $1/2mv^2$ and integrating over velocity, we get the energy conservation equation.

$$\frac{\partial}{\partial t}\left(\frac{3}{2}p\right) + \nabla \cdot \frac{3}{2}(p\mathbf{u}) + p\nabla \cdot \mathbf{u} + \nabla \mathbf{q} = \frac{\partial}{\partial t}\left(\frac{3}{2}p\right)|_c \tag{2.10}$$

Here $\mathbf{q}$ is the heat flow vector, $\mathbf{q} = -\kappa_T \nabla T$, where κ_T is the thermal conductivity of the fluid. The RHS term includes changes to thermal energy due to all types of collisions.

How do we decide when it is alright to apply the fluid model? In most instances, we are interested in studying the plasma over time and length scales much larger than those over which collisions occur. The characteristic length scale, L of the discharge (which is typically the size of the chamber in which the discharge is ignited) needs to be much larger than the collision length $\lambda = v_{mean}/\nu_m$, where v_{mean} and ν_m are the mean velocity and collision frequency respectively. The transport time scale $\tau \approx (L/\lambda)^2/\nu_m$ should be much longer than the time between collisions $1/\nu_m$. Another common assumption is that the charged particles in the extremities of the velocity space are behaving no differently from the particles having the mean velocity. This assumption would not hold good for electrons, for instance, because electrons in the high energy tail of the distribution tend to participate in inelastic collisions and are responsible for ionization, while the lower energy electrons participate in elastic and excitation collisions. In addition to the above assumptions, multiple collisions over the time and length scale of interest cause the microscopic patterns in the plasma to 'average out', allowing us to treat the species as a fluid.

2.1.2 Nonmagnetized discharges

When the time variation of electric field, and current density are small in the discharge, the magnetic fields can be neglected. In such a case, $\nabla \times E \approx 0$ and the electric field can be expressed as the gradient of a scalar potential. Equation 2.5 remains of the

Maxwell's equations, which is the Poisson's equation for the electrostatic field.

$$\epsilon_0 \nabla \cdot (-\nabla \phi) = \rho \tag{2.11}$$

2.1.3 Atmospheric pressure LTPs

This section pertains to the modeling of atmospheric pressure dielectric barrier discharges, where magnetic fields are absent. The high collisionality in the discharge, and the fact that the plasma is a low temperature discharge enables us to make further simplifications to the fluid equations. Let us consider the momentum conservation (2.8) equation first. The charged species are being acted upon only by the electric field, so $\mathbf{F} = q\mathbf{E}$. The collisions of charged species with neutral gas atoms/molecules act as friction, dissipating the energy gained in the field. It is valid to assume at high pressures, that the work done by the electric field on the charged particle is completely consumed in overcoming the friction due to collisions, and the spatial gradients in concentration. Therefore, the left hand side of Equation 2.8 is neglected. The friction due to collisions is related to the frequency of momentum transfer collisions and the velocity of the species $f|_c = m\nu_m \mathbf{u}$. The momentum equation thus reduces to Equation 2.12, which is called the drift-diffusion approximation.

$$\mathbf{u} = \frac{q\mathbf{E}}{m\nu_m} - \frac{kT}{m\nu_m}\frac{\nabla n}{n} \tag{2.12}$$

This leads to the expression of flux Γ, given by Equation 2.13, where $\mu = |q|/m\nu_m$ is the mobility and $D = kT/m\nu_m$ is the diffusivity of that species.

$$\Gamma = \pm \mu n E - D \nabla n \tag{2.13}$$

It is seen that diffusivity and mobility have temperature dependence (mobility has temperature dependence because collision frequency is temperature dependent). In LTPs, charged particles which are as heavy as the gas medium, such as ions, can be

assumed to be at the gas temperature in the bulk of the discharge. Using the drift-diffusion approximation for electrons, and coming up with the transport coefficients is more involved. Electrons in LTPs are much hotter than the room temperature ions. The electron energy relaxation time is much larger than time scales of interest, therefore much of the energy gained by electrons along the electric field ends up as heat, due to the momentum transfer collisions with gas molecules that randomize the electron velocity. Clearly, we need to solve an equation for electron energy balance to determine their temperature. Of the Boltzmann equation, and the fluid equation for energy balance, which one do we choose?

The electron-electron collisions which help the electrons to thermallly equilibrate are very rare in weakly ionized plasma implying that their distribution strongly deviates from Maxwellian. Another important observation is that most electrons possess an energy lower than that needed for ionizing the gas (ionization potentials are usually above 10 eV). Therefore it becomes very important to know exactly what fraction of electrons are capable of ionization. Clearly, the fluid equation that assumes a Maxwellian distribution is not suitable. We need to solve the Boltzmann equation, to obtain the electron energy distribution function.

A simplified form of the steady state Boltzmann equation in zero dimensions (the electron kinetic equation) is solved to obtain the electron energy distribution function (EEDF). We shall only discuss the main assumptions that are made in the kinetic equation. The electron energy distribution is assumed to be a function only of the reduced electric field (E/N where E is the electric field, and N is the number density of the gas). This is applicable if E/N can be assumed to be constant over the distance travelled by an election between two collisions, and if the field does not change over the time it takes for the electron to be heated under its influence. The EEDF is assumed to have no directional dependence. All the relevant collision cross sections between electrons and

the gas are considered for calculating the electron energy losses. Finally, EEDFs are obtained for a given gas pressure, and composition, for a range of electric fields. The distribution functions are then integrated to obtain the mean energy, ionization rates, and transport coefficients of electrons as a function of the electric fields.

The above functions are used to determine the diffusivity and mobility of electrons, and reaction rates, based on the electric field at each point in space. The set of self consistent equations describing an atmospheric pressure LTP for singly charged ions n_k, and electrons n_e, at gas density N, therefore, reduce to the following.

$$\frac{\partial n_k}{\partial t} + \nabla \cdot (\pm \mu_k n_k E - D_k \nabla n_k) = G - L \tag{2.14}$$

$$\frac{\partial n_e}{\partial t} + \nabla \cdot (-\mu_e (E/N) n_e E - D_e (E/N) \nabla n_e) = G - L \tag{2.15}$$

$$\epsilon_0 \nabla \cdot E = q \left(\sum \pm n_k - n_e \right) \tag{2.16}$$

The above set of equations is used for modeling the atmospheric pressure dielectric barrier discharge on a plasma actuator, as seen in Chapter 3.

2.1.4 Zero D models of low pressure discharges

Volume averaged, or zero dimensional models of plasma discharges are used in order to study qualitative discharge characteristics and obtain approximate values of relevant quantities such as plasma density, and electron temperature. They are useful tools because they are computationally inexpensive, and easy to set up. Discharges that can be solved self-consistently by volume averaging need to be in simple closed geometries, and at low pressures, such that micro-discharge and streamer formations are absent. Low pressure RF discharges are most suited to study with the help of volume averaged simulations. Chapter 4 describes in detail the derivation of the volume averaged model

to describe a CCP RF discharge in the presence of dust particles. In the present section, we merely speak about the general assumptions that are made to arrive at the equations.

The most important feature of zero dimensional models is that spatial profile of the discharge has to be assumed, as it cannot be computed. Consequently, the Poisson's equation for electrostatic field is not solved either. As a result, the equations describing the quasi-neutral, bulk plasma cannot describe the sheaths. A sheath is a thin region in the plasma, that forms adjacent to a surface; in this case the chamber containing the discharge. Sheaths are typically deficient in electrons. In electropositive plasma sheaths produce an electric field pointing towards the surface, and create a balance between the flux of highly mobile electrons and the heavier ions. Different sets of equations are used to describe the sheath characteristics, and the bulk plasma characteristics; the quantity that connects them both is the electric current continuity in the discharge. A steady state equation for species transport, now representing only the bulk of plasma is reduced to Equation 2.17.

$$\nabla \cdot (\pm \mu n \mathbf{E} - D \nabla n) = G - L \tag{2.17}$$

A diffusion coefficient (D_a) is obtained by equating the flux of elections and ions, and eliminating the electric field; this is called the ambipolar diffusion coefficient. This way, the electric field is eliminated and we obtain Equation 2.18.

$$\nabla \cdot (-D_a \nabla n) = G - L \tag{2.18}$$

The flux at the edge of quasineutral part of the discharge, i.e. at the plasma sheath boundary can be assigned a Bohm velocity $-D(\nabla n)_s = n_s u_B$, $u_B = \sqrt{kT_e/M}$. Consider a cylindrical discharge chamber with radially uniform plasma. Assuming the plasma to be uniform in the bulk of the discharge, with the density sharply falling to n_s at the plasma sheath boundary, we can integrate Equation 2.18, along the cylinder length l . We obtain Equation 2.19 where the ions lost to area A of the electrodes are generated

in volume V of bulk plasma.

$$n_s u_B A = (G - L)V \tag{2.19}$$

The density of the species, at the plasma sheath boundary $n_s(n, l, \lambda_i)$ is determined by heuristic relations obtained from steady state plasma solutions over a wide range of pressures [3]. Under the specification of total power absorbed in steady state, the energy balance equation, Equation 2.10 reduces to Equation 2.20 where all absorbed power is considered to be consumed by electron atom collisions denoted by subscript (e, n), and species loss to wall denoted by (i, w), as they fall through the sheath potential. The term $\varepsilon_{e,n}$ denotes the energy associated with every type of inelastic collision process i. $\varepsilon_{i,w}$ denotes the energy carried by every ion as it accelerates within the sheath and is lost to the wall.

$$P_{abs} = \sum_i \varepsilon_{e,n} \nu_{e,n}(f(E)) + n_s u_B A \varepsilon_{i,w} \tag{2.20}$$

The dependence of electron processes on the EEDF requires us to have knowledge of the EEDF, or include the electron kinetic equation in the system of equations. Since we do not have knowledge of the EEDF we include time dependent Boltzmann equation solver in the equation system.

This system of equations is further developed in Chapter 4, accounting for RF sheaths, and presence of nanoparticles. The model is useful for estimating discharge characteristics as functions of operating conditions of the plasma.

2.1.5 Particle in Cell Monte Carlo simulations

Particle in Cell Monte Carlo (PIC-MC) methods are useful in simulating plasma discharges when microscopic details of the discharge need to be obtained. In MC simulations plasma particles are followed over multiple collisions and their position, velocity, and acceleration are constantly monitored. The behavior of a large number of particles

over multiple collision events over time can be considered as the time averaged behavior of the system. Collisions are considered to occur instantaneously and are determined by the Null Collision method [15]. Between collisions the position, velocity and acceleration of the particles are calculated using Newton's equations of motion.

The goal of MC simulations in the present work is to obtain histograms of energies with which ions impinge nanoparticles in low pressure discharges. We consider a spherically symmetric system to reduce the independent variables to (r, θ, t). Therefore the simulation domain is one dimensional; one end of the domain is the surface of the spherical nanosized particle. The other end is situated inside the undisturbed plasma volume. Electrons are considered to be a fluid in Maxwellian distribution. Ions are considered to be discrete particles; they enter the domain at Maxwellian distribution from the undisturbed part of the discharge and are tracked until they exit the domain. The electric field in the domain is obtained by solving Poisson's equation.

MC simulations enable us to capture features that are otherwise lost while performing averaging operations. Further, due to the very few assumptions made on transport equations of plasma species, MC simulations can be used as a benchmark to check the validity of fluid equations and analytical models, as shall be seen in Chapter 5.

Chapter 3

Simulation of Plasma Actuator

3.1 Introduction

A dielectric barrier discharge (DBD) plasma actuator, in its most basic design, consists of two electrodes attached to opposite sides of a dielectric sheet, with an offset in their positions. A schematic is shown in Figure 3.1. Typically, the dielectric material consists of glass, kapton, alumina, or ceramics, and its thickness ranges from 0.1 to a few millimeters. One side of the actuator faces a nonconducting material, while one side is exposed to air. The electrodes are typically a few millimeters long. When the electrodes are powered with a high enough amplitude of time-varying voltage, air break down occurs and plasma is formed on the dielectric surface as shown in Figure 3.2. Typically, an AC voltage of a few kV amplitude is applied at a frequency of 3-15 kHz. The discharge is seen to impart a time-averaged net force, inducing a flow in the neutral quiescent fluid in its vicinity. The component of this force vector parallel to the actuator surface points away from the exposed electrode; this direction shall be called 'streamwise' direction hereafter. The force inducing property of plasma actuators is useful for active flow control over airfoils and other flow passage surfaces.

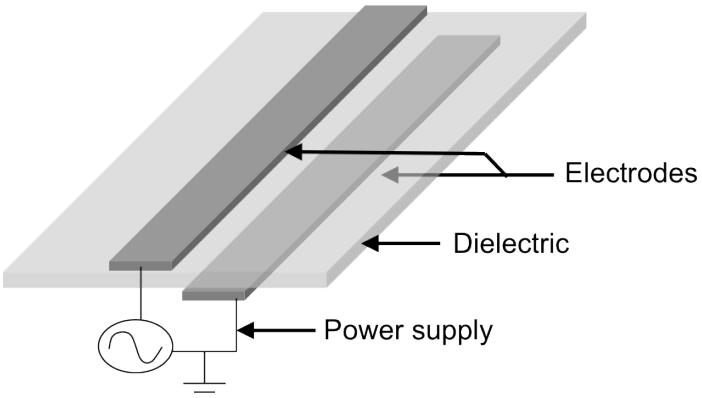

Figure 3.1: Schematic of a basic plasma actuator.

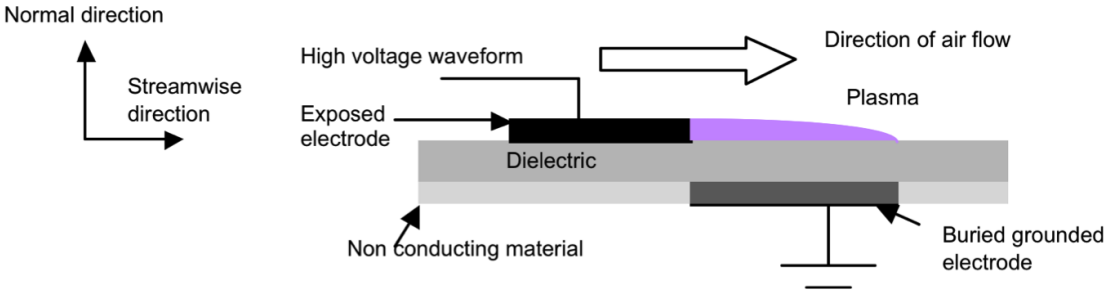

Figure 3.2: Schematic of the working of an actuator.

When fluid flows past an airfoil, lift is generated in the direction perpendicular to the fluid motion (Figure 3.3). An airfoil is most efficient if the streamlines follow the shape of the foil, as seen in Figure 3.4. In many flow situations, this is hard to achieve. The flow creates a boundary layer over the foil surface where viscous effects on the fluid momentum are predominant. The fluid accelerates as it flows from the leading edge of the foil, which is a higher pressure region, to the upper surface, a lower pressure region. As it continues to flow from this low pressure region back to the high pressure region in the downstream portion of the foil, the fluid encounters an adverse pressure gradient. In a situation where the adverse pressure gradient is sufficiently large, the fluid in the boundary layer (where viscous forces are also present) decelerates. At a point where the velocity drops to zero, the boundary layer separates from the foil surface, creating reverse flow eddies, adversely affecting the performance of the foil. Preventing this boundary layer detachment is an important part of improving airfoil performance.

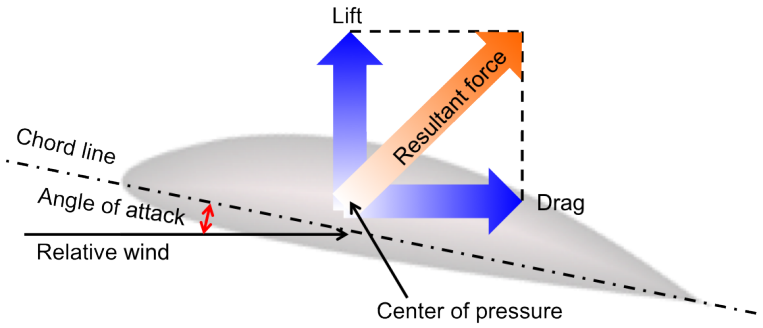

Figure 3.3: Schematic depicting the resultant force on an airfoil immersed in a flowing fluid.

A DBD plasma actuator is an attractive option for this purpose. The plasma actuator is flush mounted on the trailing edge of the foil, where the fluid flow experiences deceleration. The force imparted by the surface discharge to the flowing fluid induces

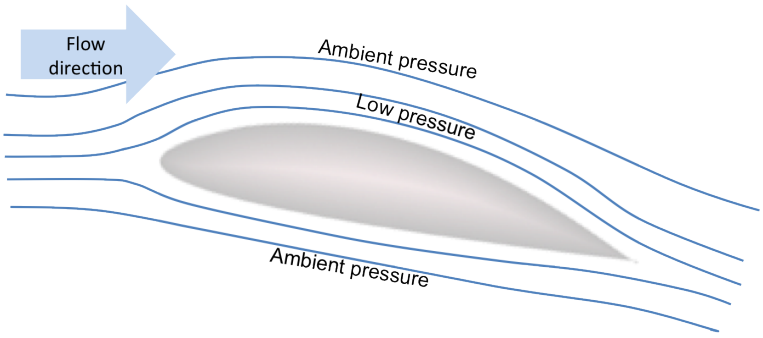

Figure 3.4: Streamlines of flow over an airfoil, depicting no separation.

additional streamwise momentum to the stalling flow.

As a result of the acquired momentum, the flow continues to stick to the foil surface. This is depicted in the flow visualization image taken from Post *et al.* [1] in Figure 3.5, where fluid flowing past a 16 degree angle-of-attack airfoil at $Re = 158 \times 10^3$ separates from the foil. When a plasma actuator on the airfoil surface is turned on, it is seen to prevent the separation. The actuator can also be operate to perturb the boundary layer flow, affecting its stability.

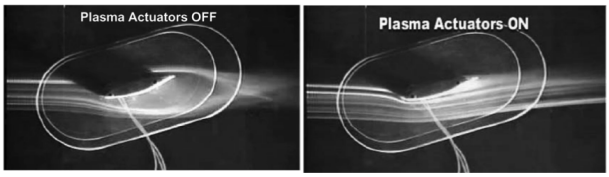

Figure 3.5: Effect of plasma actuator on boundary layer separation seen in flow visualization over an airfoil at 16 degrees angle of attack: $Re = 158 \times 10^3$ [1].

Study of DBD plasma actuators is multidisciplinary. The fluid mechanics aspect of the study, which is beyond the scope of this discussion, focusses on placement of the actuators on airfoils, frequency of plasma ignition, and the resultant effects on boundary

layer characteristics [16, 17, 18, 19]. The plasma physics aspect of the study, which shall be discussed herein, focusses on understanding the discharge physics responsible for force generation, and ways to manipulate the discharge in order to maximize the same. Several groups conducted experiments on plasma actuators powered by AC sinusoidal voltage, to observe the space and time evolution of the DBD, and measure the thrust produced [20, 21, 2, 22, 23]. It was observed that the gas breakdown occurred over a small part of the voltage cycle, and the plasma consisted of several microdischarges that formed and extinguished on times scales much smaller than the voltage frequency. Moreover the characteristics of the discharge formed during the positive half of the cycle (exposed electrode is anode) were markedly different from the one formed during the negative half cycle. A relatively weak field is required to extract electrons from the exposed electrode, when it is negatively biased, compared to the high field needed to extract electrons from the vicinity when the electrode is positively biased. Therefore, when the exposed electrode was positively biased, the microdischarges were streamer like, characterized by high electric field. During the negative cycle, the plasma discharge ignited at a lower electric field and resembled a glow discharge, constituted by weak short-lived microdischarges. Figure 3.6 [2] is a high speed photograph (20 μs exposure) of the discharge during positive and negative voltage half cycles; it shows a dramatic difference in the spatial structure. This spatial dissimilarity between the discharge during the two halves of the cycle was the cause of the time-averaged streamwise direction of the thrust.

The basic understanding of the DBD actuator physics led to experiments that studied optimization of the actuator geometry and operating parameters [24, 25, 26]. The thrust increased with increased voltage frequency and amplitude of AC voltage. Actuators powered by nanosecond pulses superimposed on a biased voltage were seen to produce more force compared to the standard sinusoidal AC voltage, at the cost of

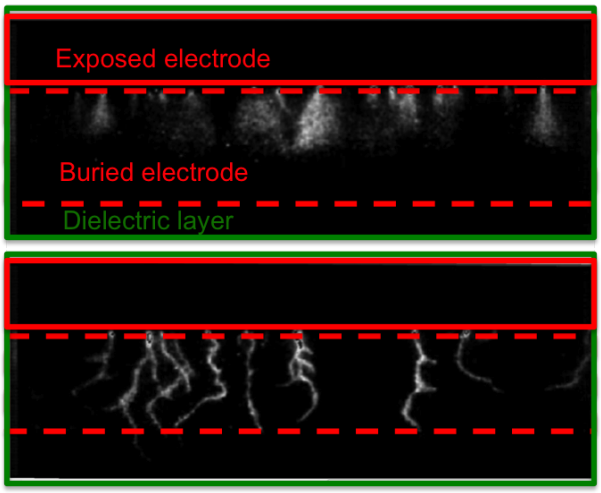

Figure 3.6: A high speed photograph showing the difference in the spatial structure of discharge caused by negative half cycle of voltage (above) and positive half cycle (below)[2]. The top view of the actuator is seen.

power consumption [27].

Plasma actuator performance is marked by phenomena occurring over a vast range of time scales. The time scale for a microdischarge formation is tens of nanoseconds. The charging of dielectric surface occurs over multiple microdischarge events, over a few microseconds. The period of a voltage cycle is of the order of 0.1 ms. Finally, the response time of the quiescent fluid to the thrust is in the order of milliseconds. Experimental studies of the actuator operation, especially those focussed on understanding the discharge physics tend to be limited by the spatial and temporal resolution of the measurement apparatus. Therefore the small timescale phenomena are better understood when aided by modeling and simulation studies. Equivalent electrical circuit models, two dimensional fluid models, Monte-Carlo simulations have been used to describe DBD discharge on the actuator. Orlov *et al.* [28] have used a circuit model to correlate the actuator thrust to the applied voltage amplitude and frequency. However, the circuit

model is not self-consistent and requires proportionality factors obtained through experiments. Boeuf and coworkers have used fluid models to simulate the actuator discharge for time varying voltage [29, 24, 30, 31, 32]. In a recent paper [32], they simulated the discharge over multiple cycles of AC voltage, reproducing the streamer-like and diffuse plasma, as seen in experiments. However, photoionization, which plays a crucial role in creating the discharge was not considered. Likhanskii *et al.* [33] have included photoionization as a source term for electrons and ions, and have modeled discharge caused by nanosecond pulses.

The present work is confined to the simulation of a single microdischarge event when a positive and negative voltage pulse is applied to the exposed electrode, and discussion of the resultant discharge characteristics. The results obtained herein corroborate the conclusions of Boeuf and Miles (Likhanskii *et al*) groups. COMSOL Multiphysics version 3.5 in conjunction with MATLAB was used for the simulation.

3.2 Description of Model

A simulation of DBD plasma actuator was performed on a two dimensional domain as shown in Figure 3.7. The medium was atmospheric air. A simplified air chemistry model, which consists of generic species of singly charged positive ions, negative ions, and electrons, was used. The air chemistry was taken from Kang *et al* [34]. A dielectric of 0.1 mm thickness was considered.

3.2.1 System of Equations

As discussed in the previous chapter, the transport of charged species at atmospheric pressure can be described by the fluid equations, using the drift-diffusion approximation

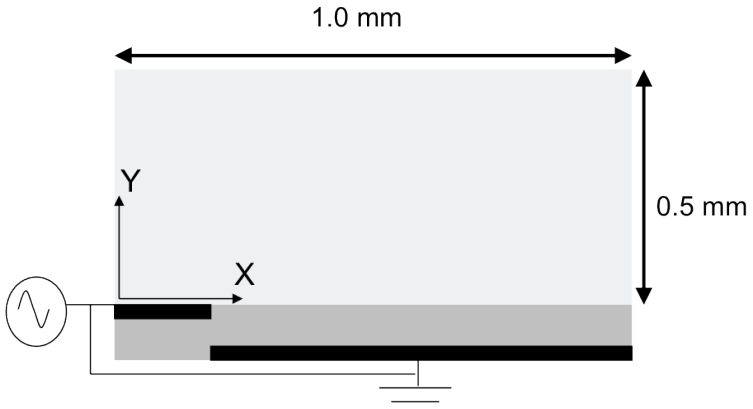

Figure 3.7: Schematic of a the simulation domain.

to calculate the flux.

$$\frac{\partial n_e}{\partial t} + \nabla \cdot (-D_e \nabla n_e + n_e \mathbf{v_e}) = \alpha n_e \left|v_e\right| - \eta n_e \left|v_e\right| - B_{ei} n_e n_i + S_{ph} \tag{3.1}$$

$$\frac{\partial n_i}{\partial t} + \nabla \cdot (-D_i \nabla n_i + n_i \mathbf{v_i}) = \alpha n_e \left|v_e\right| - B_{ei} n_e n_i - B_{in} n_i n_n \tag{3.2}$$

$$\frac{\partial n_n}{\partial t} + \nabla \cdot (-D_n \nabla n_n + n_n \mathbf{v_n}) = \eta n_e \left|v_e\right| - B_{in} n_e n_i \tag{3.3}$$

n_e, n_i, n_n denote the densities of electrons, positive ions and negative ions respectively. $\alpha = 3.5{\times}10^3 \exp\left(-1.65 \times 10^5 E^{-1}\right)$ $[cm^{-1}]$, and $\eta = 1.5{\times}10 \exp\left(-2.5 \times 10^4 E^{-1}\right)$ $[cm^{-1}]$ are the field dependent Townsend ionization coefficient, and attachment coefficient respectively (E is in V/cm). The electron ion recombination rate $B_{ei} = 2 \times 10^{-7}\ cm^3/s$, and S_{ph} is the rate of electron production due to photoionization, calculated using the model developed by Bourdon *et al* [35], and used for plasma actuator simulation by Likhanskii *et al* [36]. The negative ion-positive ion recombination rate $B_{in} = 2 \times 10^{-7}\ cm^3/s$. The mobilities of each species are given as $\mu_e = 6.06 \times$

$10^3\ E^{-0.25}\ cm^2/Vs$ (E is in V/cm), $\mu_i = 2.43\ cm^2/Vs$, and $\mu_n = 2.7\ cm^2/Vs$. Diffusivities of the species are given by $D_e = 1800\ cm^2/s$, $D_i = 0.062\ cm^2/s$, $D_n = 0.69\ cm^2/s$. Positive and negative ions are assumed to be at room temperature, and electron temperature is calculated using Einstein's relation (Equation 3.4).

$$T_e = \frac{eD_e}{\mu_e k} \tag{3.4}$$

The velocity of each species, was calculated as in Equation 3.5.

$$\mathbf{v_k} = sgn(q_k)\mu_k \mathbf{E} \tag{3.5}$$

The transport equations are coupled with Poisson's equation (Eq. 3.6) for the electric field. Here ϵ_r is 1 in air, and it is equal to the relative dielectric permittivity in the dielectric medium, taken to be 6 in the present work.

$$\nabla \cdot \nabla (\epsilon_r V) = \frac{e}{\epsilon_0} (n_i - n_e - n_n) \tag{3.6}$$

The current to the dielectric layer (Equation 3.7) is integrated over time to calculate the accumulated charge (Equation 3.8). Here γ is the secondary electron emission coefficient. It is the fraction of positive ions that cause the desorption of an electron from the dielectric surface, due to their energy of impaction. Its value is taken to be 0.01 on the dielectric surface, and 0.1 on the exposed electrode. We assume that recombination occurs between species of opposite charge on the dielectric surface. Total current to the actuator surface is given by Equation 3.7. Charge accumulated on the dielectric surface is given by integration of this current over time (Equation 3.8).

$$I = q\left(-\left(-D_e \nabla n_e + n_e \mathbf{v_e}\right) + (1+\gamma)\left(-D_i \nabla n_i + n_i \mathbf{v_i}\right) - \left(-D_n \nabla n_n + n_n \mathbf{v_n}\right)\right) \tag{3.7}$$

$$\sigma = \int_0^t I\ dt \tag{3.8}$$

3.2.2 Boundary Conditions

The boundary conditions for the species continuity equations solved only in the region of the domain where air is present are tabulated in Table 3.1. Poisson's equation is solved in the air as well as the dielectric regions; its boundary conditions are tabulated in Table 3.2. The boundaries are numbered in Figure 3.8.

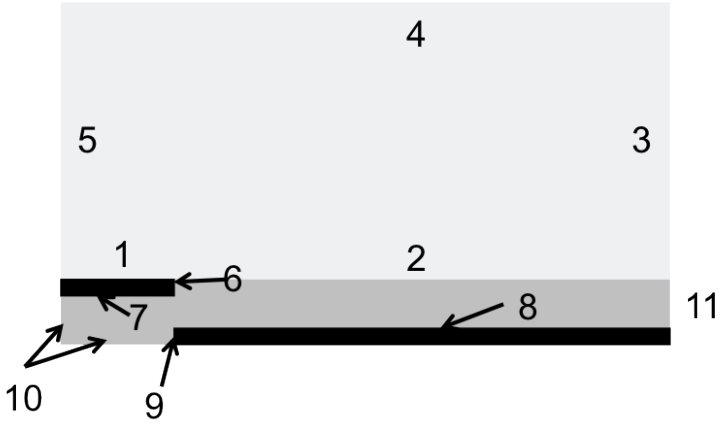

Figure 3.8: Boundaries of the simulation domain. Boundary conditions given by numbers are given in Tables 3.1 and 3.8.

Table 3.1: Boundary conditions for continuity equations

Boundary	Electrons	Positive/Negative ions
3,4,5	Flux = 0	Flux = 0
1,2	Flux = $n_e v_{th}/4 + \gamma\left(-D_i \nabla n_i + n_i \mathbf{v_i}\right)$	Flux = $-D_k \nabla n_k + n_k \mathbf{v_k}$

The continuity equations and Poisson's equation are solved simultaneously, subject to the above boundary conditions. An initial uniform background density of $10^5\ cm^{-3}$ is set for all species. A time dependent solver called the Direct Pardiso (a solver available in COMSOL) is used. The BDF method is selected for time stepping; the minimum

Table 3.2: Boundary conditions for Poisson's equation

Boundary	Boundary condition
3,4,5	$\nabla V \cdot \hat{n} = 0$
1,6,7	$V(t) = V_{applied}$
2	$(\nabla V)_+ - (\nabla V)_- = \sigma/\epsilon_0$
8,9	$V = 0$
10,11	$\epsilon_r \nabla V \cdot \hat{n} = 0$

size of time step is determined by the solver. The relative and absolute tolerances are set to 10^{-3}, and 10^{-4} respectively. A non uniform triangular mesh was used; with the finest elements of the mesh close to the dielectric surface and of the size $\approx 10^{-6}\ m$.

The time step needs to be of the order of picoseconds to simulate the streamer event. Due to constraints on computational time, our work is limited to the simulation of streamer events over a time period of a few nanoseconds.

3.3 Simulation results

A Gaussian pulse of 3.5 kV amplitude, and 3 nanoseconds Full Width at Half Maximum (FWHM) is applied to the exposed electrode. When the pulse is positive with respect to the grounded electrode, a streamer originates at the edge of the exposed electrode when the electric field becomes high enough. The streamer consists of mainly electrons and positive ions, with the negative ions having a density two orders of magnitude less than the other two. Figure 3.9 shows the origin and propagation of the cathode directed streamer at different times during the pulse (seen in the inset). The plasma is denoted by the positive ion density in the figure, whose value reaches $10^{15}\ cm^{-3}$ in the quasineutral region of the discharge. It is seen that the head of the streamer consists of a net positive charge, populated by the positive ions being repelled from the exposed electrode. The accompanying plots of the potential show that the discharge

is a conducting medium, at the same potential as the exposed electrode. Positive ions in the streamer accumulate on the dielectric surface, and this process is slower than the streamer propagation, which is seen to be $\approx 10^8\ cm/s$. The dielectric surface close to the exposed electrode reaches the potential of the electrode, as seen at 5.5 and 6.0 nanoseconds, due to ion accumulation.

A negative pulse of 3.5 kV amplitude produces an anode directed streamer where electrons are emitted from the exposed electrode. Electron emission from metal is easier to achieve, than, for example, electron emission from the dielectric medium and air as is needed during positive biasing. The plasma ignites at a lower electric field value in this instance. Figure 3.10 shows the positive ion density and potential at different times during the voltage pulse, as the anode directed discharge ignites and propagates. It is seen that the discharge ignites not at the edge of the exposed electrode but on the dielectric surface where an electron avalanche is caused by the electrons reaching the dielectric surface, along the yet undistorted field lines. This is followed by a cathode directed streamer seen at 5 nanoseconds. After the streamer strikes the exposed electrode, the plasma begins to propagate on the dielectric surface, as a discharge directed towards the buried grounded electrode which is now positively biased with respect to the exposed electrode. The head of the discharge consists of a net negative charge, populated by electrons. From the potential plot at 5.0 and 5.5 nanoseconds we can see that the surface of the dielectric is at the same potential as the exposed electrode, unlike the corresponding potential plots in Figure 3.9 where the charge accumulation on the dielectric surface was seen to be a slower process. The electrons being more mobile and light are able to charge up the dielectric surface more efficiently than can the heavy positive ions.

As the charged species move along the electric field lines, they are accelerated. We assume that the energy gained by the species is completely transferred to the neutral

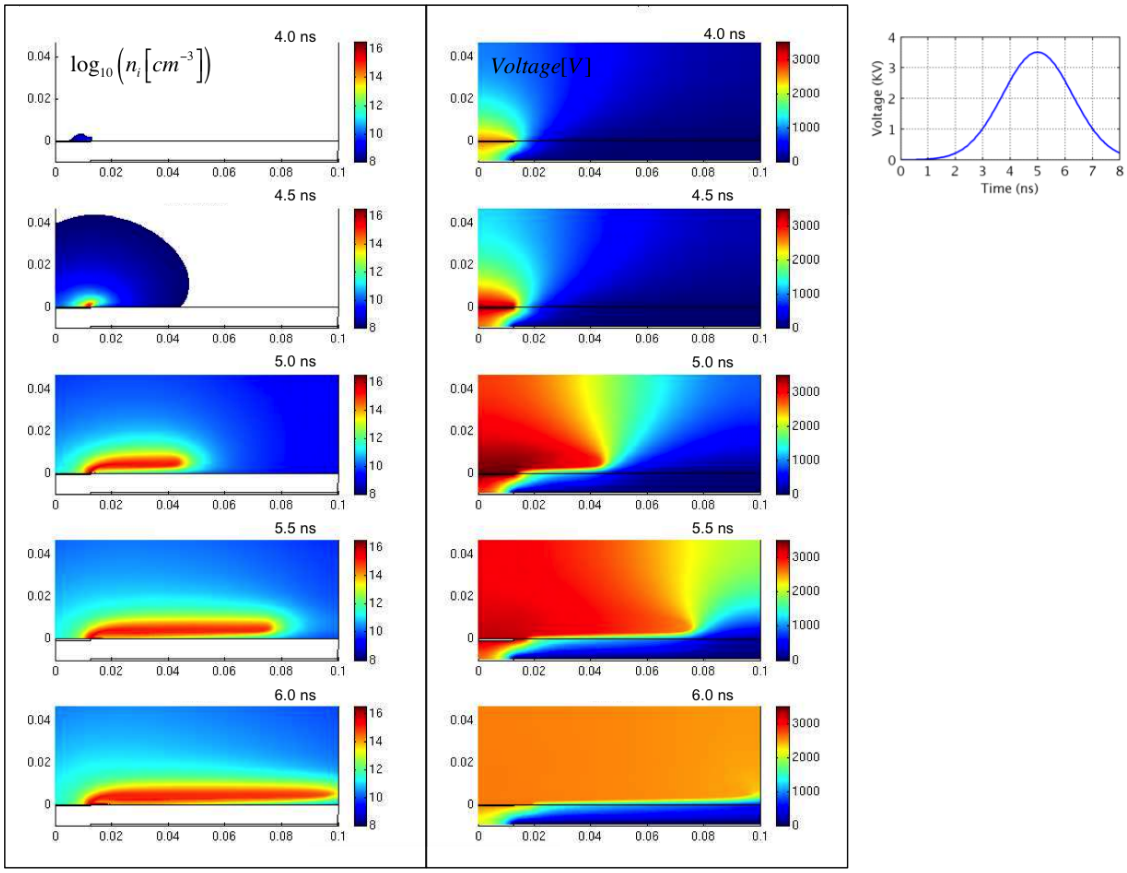

Figure 3.9: Positive ion density and potential of a discharge during the application of a positive pulse (seen in the inset), denoting the propagation of a cathode directed streamer.

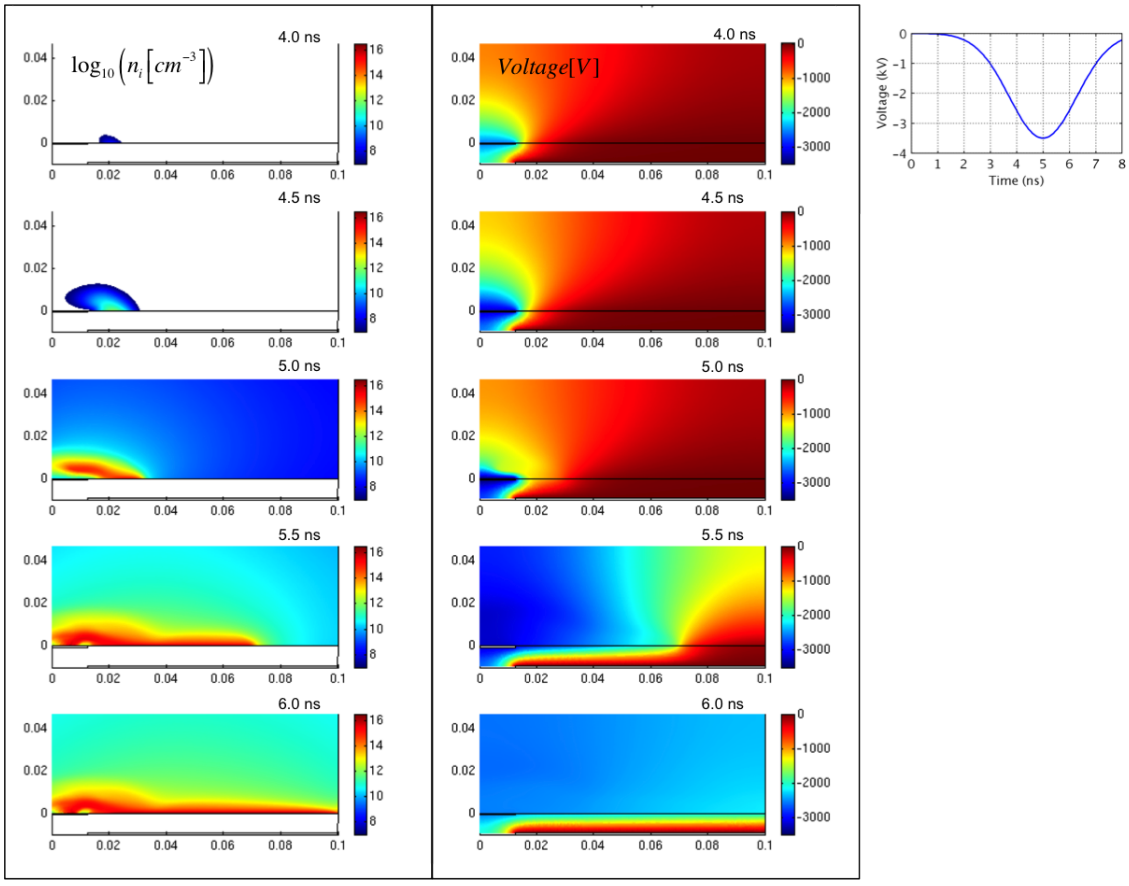

Figure 3.10: Positive ion density and potential of a discharge during the application of a negative pulse (seen in the inset), denoting the propagation of a anode directed streamer.

gas molecules due to collisions. Therefore, the force acting on the neutral gas per unit volume can be calculated by Equation 3.9. This force can be referred to as a 'body force', because it acts on the 'volume' of the neutral gas.

$$f = q\mathbf{E}\left(n_i - n_e - n_n\right) \tag{3.9}$$

Figure 3.11 compares the x-component of body force (parallel to the surface of the actuator) produced by the cathode and anode directed streamers discussed above. The left column depicts the evolution of force as the cathode directed streamer propagates. The quasineutral part of the plasma does not exert a body force because of zero net space charge. However, the plasma sheath on the dielectric surface, and the head of the streamer are non-quasineutral. These regions exert a stream wise direction force.

The right column depicts the x-component of the body force generated by an anode directed plasma. During the ignition of the negative-pulse discharge, a cathode directed streamer is formed, moving towards the exposed electrode, creating an anti-streamwise direction body force. After this streamer strikes the exposed electrode, the plasma propagates on the dielectric with a net negative charge leading the streamer head, exerting a weak force, in the streamwise direction. The anti-streamwise force near the exposed electrode is confined to a small region; the weak streamwise force, on the other hand, arises from the discharge spread over the dielectric. Figure 3.12 compares the normal component of the body force obtained due to the different pulses. Both positive and negative voltage pulses cause a body force directed towards the surface of the actuator.

The variation of x-direction electric field with time on the actuator surface for the positive and negative pulses is shown in Figure 3.13. For the positive pulse (Figure 3.13a), the breakdown of gas is preceded by the creation of a high field at the edge of the exposed electrode. The high field streak on the actuator surface is the field at the head of the propagating streamer. At 6 nanoseconds there begins to be a zero field

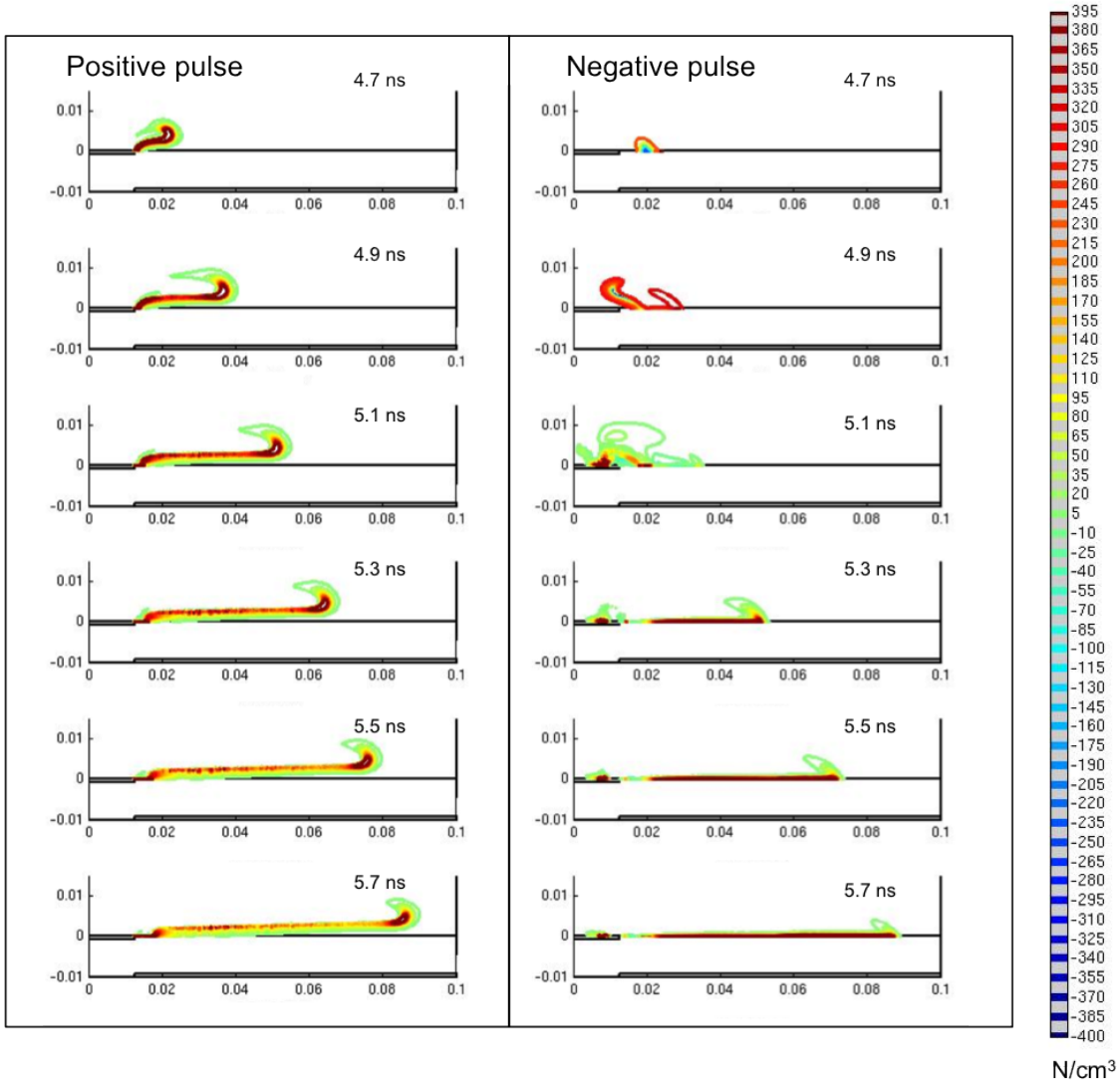

Figure 3.11: Streamwise direction force per unit volume for positive and negative applied voltage pulses at the exposed electrode, seen in Figure 3.9 and Figure 3.10, respectively.

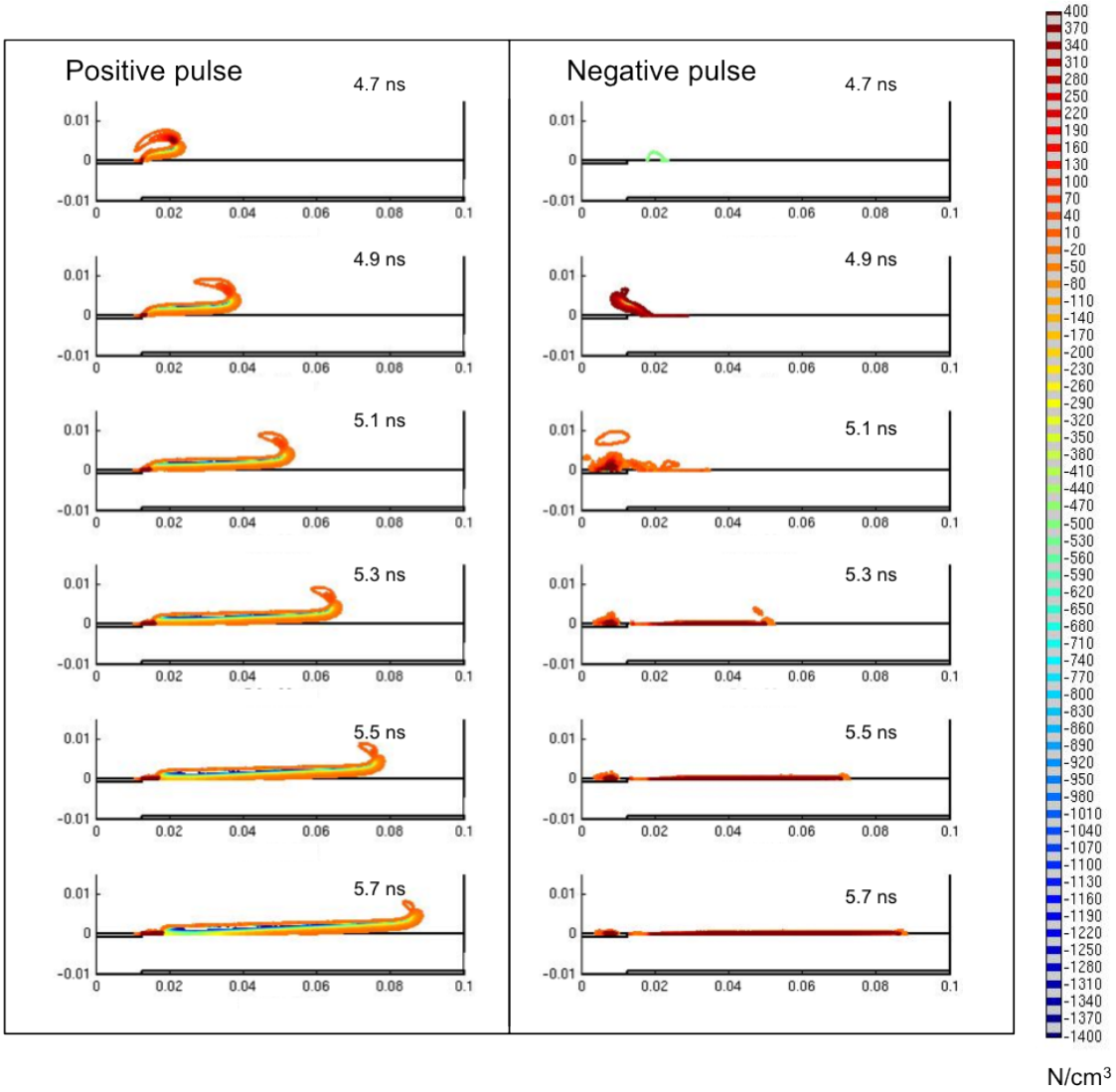

Figure 3.12: Normal direction force per unit volume for positive and negative applied voltage pulses at the exposed electrode, seen in Figure 3.9 and Figure 3.10, respectively.

region extending from the exposed electrode. This is the extension of the electrode caused by positive charge deposition on the dielectric surface. Figure 3.13b reveals that during the the negative pulse the head of the streamer is driven by an electric field whose x-component is in the anti-streamwise direction. During the fall of the voltage pulse, though, a streamwise direction field is seen, indicating a reversal of polarity. The voltage on the exposed electrode falls, while the dielectric remains charged by electrons; the dielectric now behaves as a cathode. The y-direction electric field during the rise and fall of the voltage pulses is seen in Figure 3.14. Figure 3.14a indicates a sheath region with a strong electric field pointing to the dielectric surface. During the negative pulse (Figure 3.14b) the normal field points towards the dielectric surface, but is seen to be weaker.

From the spatial and temporal profiles of body force contours and the electric field, it can be inferred that the plasma actuator provides a strong streamwise force during the part of the time varying voltage cycle when the exposed electrode is positively biased with respect to the dielectric. When the exposed electrode is negatively biased, there is a anti-streamwise force during a part of the plasma discharge, as the cathode directed electrode avalanche grows towards the exposed electrode. Once the plasma strikes the electrode, it propagates on the dielectric, led by a streamer head consisting of net negative space charge, and providing a weak streamwise force to the neutral gas.

In reality, the actuator operates under sinusoidal voltage in the kHz range. Its performance depends on longer scale processes, such as multiple streamer creation and quenching events in each half cycle, and dielectric charging over multiple voltage cycles. From the simulation, however, it is possible to establish the basic reason for creation of the streamwise thrust. During the positive half of the sinusoidal voltage, multiple discharge events occur, consisting of localized, short-lived cathode directed streamers.

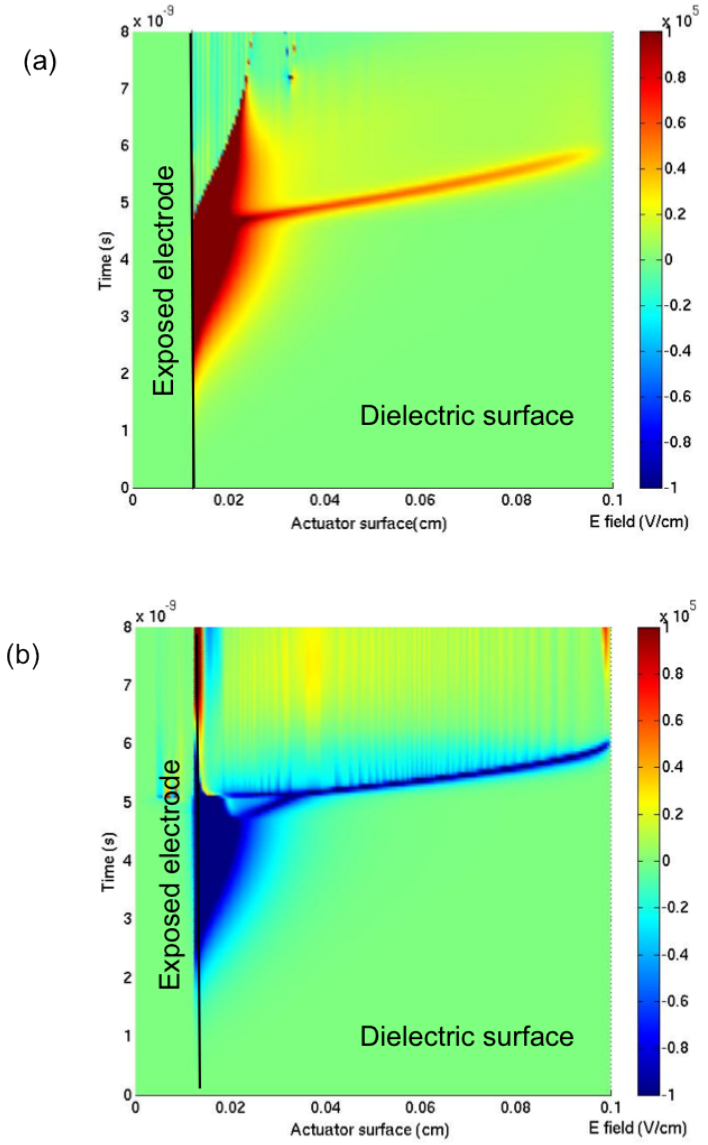

Figure 3.13: Component of the electric field in the direction parallel to the actuator surface during the application of, (a) positive pulse, and (b) negative pulse seen in figures 3.9 and 3.10, respectively.

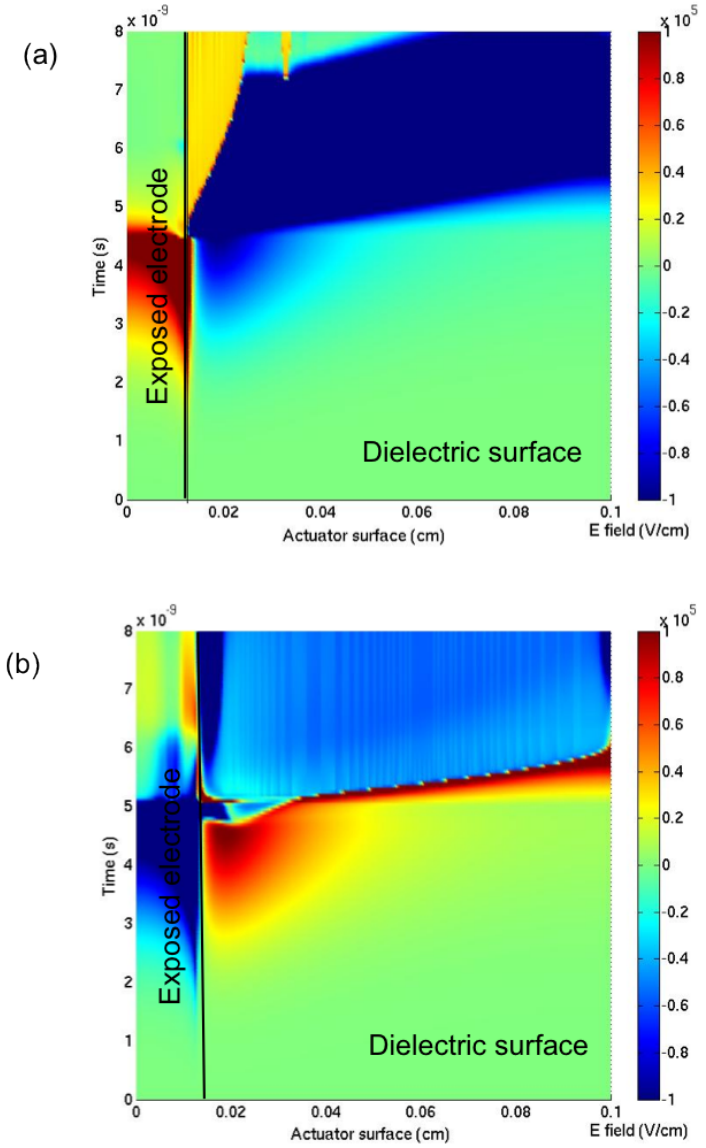

Figure 3.14: Component of the electric field in the normal direction to the actuator surface during the application of, (a) positive pulse, and (b) negative pulse seen in figures 3.9 and 3.10, respectively.

Each produces a strong streamwise force. During the negative half of the voltage, multiple anode directed discharges are formed. These discharges impart anti-streamwise force in the short region near the exposed electrode, and weak streamwise force over the dielectric surface. The force can be described as 'Push-push', the 'Push' denoting a strong streamwise force during the positive voltage, and 'push' denoting a weak streamwise force during the negative voltage.

It can be inferred that when the actuator is operating over multiple AC voltage cycles, charge deposited over the dielectric from the previous discharge event would influence the subsequent discharge. For instance, positive ions accumulated over the dielectric tend to be pulled toward the exposed electrode during the following negative voltage pulse, resulting in an anti-streamwise force. This would cause a small time averaged streamwise thrust. And therefore, controlling/draining the charge accumulated over the dielectric surface would modify the body force. Actuator experiments by Opaits *et al* [37] have indeed shown that draining of charge from the dielectric surface using a semiconducting layer led to an increased time-averaged thrust. Song et al [38] introduced a 100 nm thick amorphous Si:H film and a third downstream electrode. They saw that the charge carrier mobility of the silicon film caused dissipation of the surface charge, influenced the electric field lines, and overall, enhanced the actuator thrust.

3.4 Conclusion

A two dimensional fluid simulation was performed to understand the working of a DBD plasma actuator. The difference in spatial and temporal structures of cathode and anode directed DBD's on the actuator, and dielectric charging characteristics were discussed. A positive voltage pulse on the exposed electrode created a streamer like discharge with high electric field at the head of the streamer, causing a strong streamwise direction force on the neutral gas. A negative voltage on the other hand was seen to create a thin

diffuse discharge propagating on the dielectric surface; the discharge at the edge of the exposed electrode imparted an anti-streamwise force, while the discharge propagating on the dielectric imparted a weak streamwise force. In both cases, a normal force directed to the actuator surface was seen. The thrust creation by actuator was thus explained at the level of the smallest timescale processes.

Chapter 4

Volume averaged simulations of argon-hydrogen CCP RF dusty plasmas

4.1 Introduction

In this chapter we develop a zero dimensional model for calculating discharge characteristics of low pressure, capacitively coupled (CC) radio frequency (RF) dusty plasma in argon hydrogen mixtures, in the presence of nano sized particles (or 'dust' particles).

Presence of trace quantities of hydrogen in low-pressure argon plasma discharge is known to alter the discharge composition and characteristics. Hydrogen ionizes as readily as argon because the ionization potentials of both gases are very close. Bogaerts et al [39],[40] have shown that for H_2 concentration varying between one and ten percent in an argon DC glow discharge at 75 and 133 Pascal, ArH^+, H_3^+ become important ion species along with Ar^+. The plasma composition is both pressure and gas ratio dependent. The effect of H_2 gas presence on electron energy distribution was shown by

Van Dyken et al[15] through Particle in Cell Monte Carlo simulations. The presence of H_2 promoted the content of very low energy electrons, and reduced the average electron energy [40]. Plasma density was seen to reduce with the addition of hydrogen gas to argon[41].

In the light of this knowledge, our concern is with argon silane CCP RF discharges used for the synthesis of silicon nanoparticles. Silane dissociates in argon plasma and forms long chain molecules, which then agglomerate to form silicon nanoparticles[42]. These particles crystallize in the plasma chamber to form hydrogen terminated silicon nanocrystals. The byproduct of this chemical activity is also atomic and molecular hydrogen.

Our goal is to study the role that the trace amount of hydrogen plays in influencing plasma particle interactions. The interaction of nanoparticles with plasma contributes to their crystallization. The type of ions, and the energy distribution of ions impacting the surface of the nano particles may be correlated to their functional properties [43].

The first step in understanding plasma particle interactions is estimating particle charge and plasma composition in the discharge. In the present work we make qualitative estimates of plasma characteristics of a low-pressure RF argon hydrogen plasma discharge containing dust particles. Average particle potential and plasma composition are calculated. We use a volume-averaged model to describe the plasma. While details concerning the spatial non-uniformities of the plasma are not captured in a volume-averaged simulation, it offers the advantage of simple and quickly solvable system of equations that are able to describe the essential physics of the discharge.

4.2 Argon hydrogen plasma chemistry

Argon hydrogen plasma chemistry has been well documented. Reaction rates for ion-gas interaction have been taken from Boagerts[39]. The ions are considered to be at

room temperature and in a Maxwellian distribution. Table 4.1 lists the ion reactions with atoms and molecules and the corresponding rate coefficients. Cross sections of interaction between electrons and neutral molecules and atoms have been taken from LXCAT[44]. Figures 4.1, 4.2, 4.3, 4.4, 4.5 depict the cross sections of interaction of electrons with ground state argon atoms, H_2 molecules, and H atoms.

Table 4.1: List of ion - atom/molecule reactions

Reaction	Reaction rate $[m^3 s^{-1}]$
$Ar^+ + H_2 \rightarrow ArH^+ + H$	6×10^{-16}
$Ar^+ + H_2 \rightarrow Ar + H_2^+$	8×10^{-17}
$Ar + H_2^+ \rightarrow ArH^+ + H$	1.7×10^{-15}
$ArH^+ + H_2 \rightarrow Ar + H_3^+$	1.5×10^{-15}
$H_2^+ + H_2 \rightarrow H + H_3^+$	2×10^{-15}
$Ar + H_2^+ \rightarrow H_2 + Ar^+$	2.2×10^{-16}

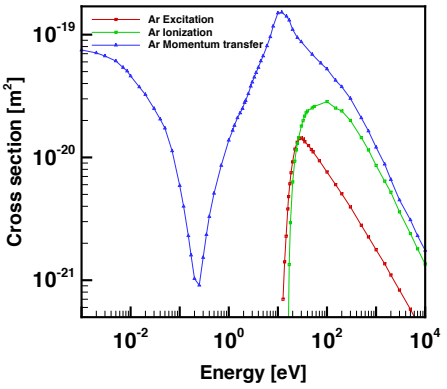

Figure 4.1: Cross sections for electron interaction with ground state argon atoms.

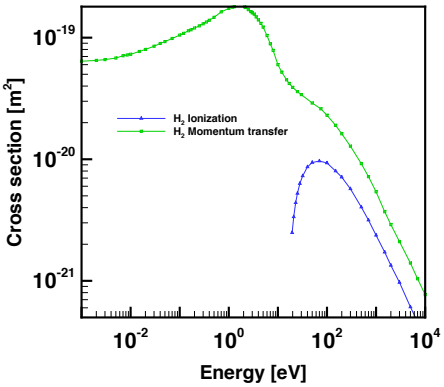

Figure 4.2: Cross sections for electron impact ionization, and momentum transfer of ground state hydrogen molecules.

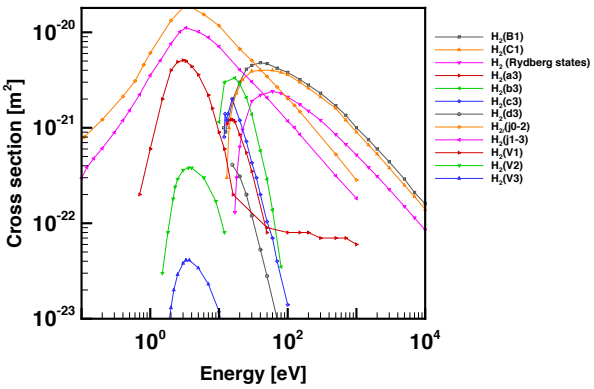

Figure 4.3: Cross sections for electron excitation of ground state hydrogen molecules.

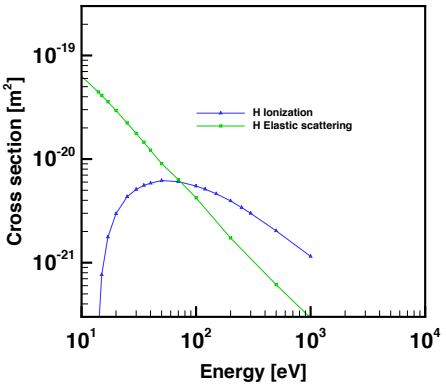

Figure 4.4: Cross sections for electron impact ionization, and elastic scattering of ground state H atoms.

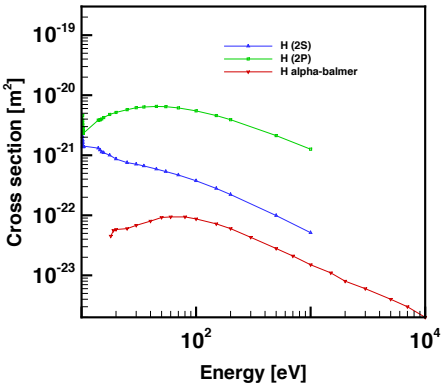

Figure 4.5: Cross sections for electron excitation of ground state H atoms.

4.3 Description of Model

We consider a cylindrical plasma chamber as shown in 4.6 consisting of parallel plane electrodes. One electrode is grounded while another is connected to an RF voltage supply. The chamber has a high aspect ratio, with 6 cm radius and 4 cm width. We assume that the plasma is uniform in the radial direction so that the discharge can be considered one-dimensional.

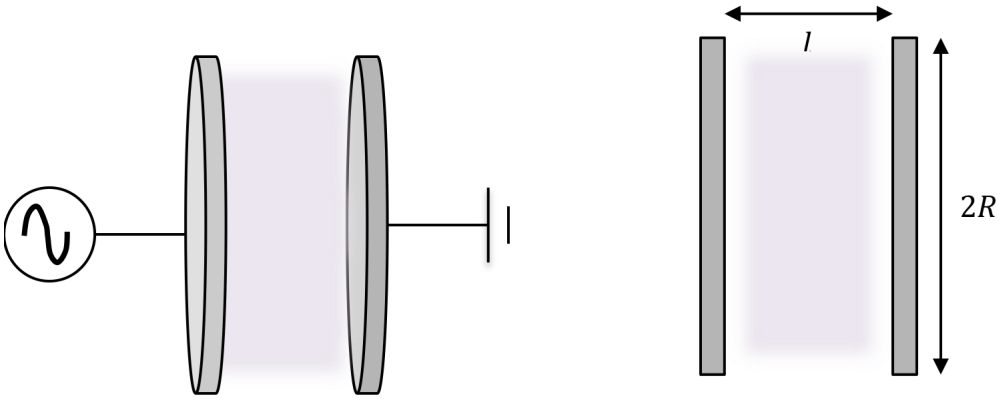

Figure 4.6: Schematic of CCP RF discharge chamber.

We describe this one-dimensional capacitively coupled RF discharge using a global model. The most important feature of the global model is that the analysis of the bulk plasma, or the quasineutral part of the discharge is distinct from the analysis of the sheath region formed close to the surface of the RF electrodes, where a positive space charge is present. The properties of bulk plasma (or just plasma) are coupled to the properties of the sheath via the current flowing through the discharge. The

mathematical model is based on the analysis of capacitive discharges found in 'Principles of Plasma Discharges and Materials Processing'[3].

4.3.1 Bulk plasma

Steady-state analytical solutions exist for the profile of the plasma in the axial direction of the cylinder, for single as well as multiple ion cases. The level of collisionality in the discharge, and the geometry of the chamber govern the shape of the profile. In a highly collisional discharge, the profile follows a cosine function. At reduced collisionality, an arc of a circle approximately describes the profile. These solutions break down in the sheath regions, where plasma is not quasineutral. In our volume-averaged simulation, we assume that the plasma density is uniform throughout the volume (see 4.7). This assumption results in only an approximate estimate of plasma density. The deviation from exact solution reduces as the pressures decreases.

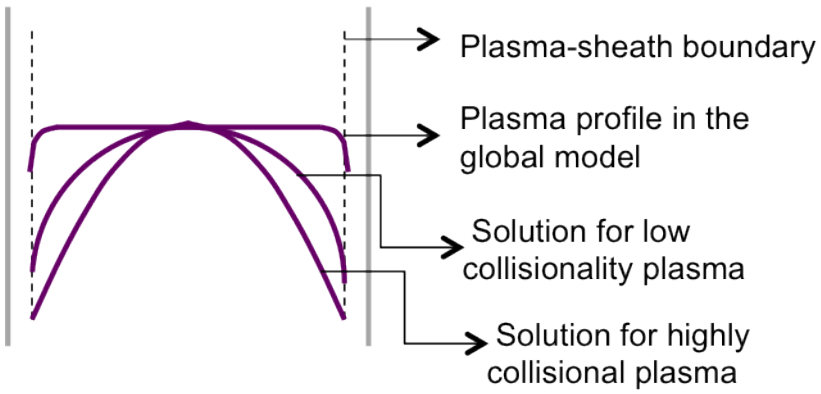

Figure 4.7: Plasma density profiles in different pressure regimes, compared to the profile assumed in the volume averaged simulation.

Additionally, dust particles are present in the discharge under consideration. They are massive and negatively charged. We can assume that they remain in the core of the

chamber, and that there is no dust particle flux to the wall. Electrons are depleted in the core due to the presence of dust. However, the electron and positive ion densities at the plasma-sheath boundary are equal. The sheaths consist of only positive ions and electrons. Figure 4.8 is a depiction of the density profiles assumed in the volume-averaged model.

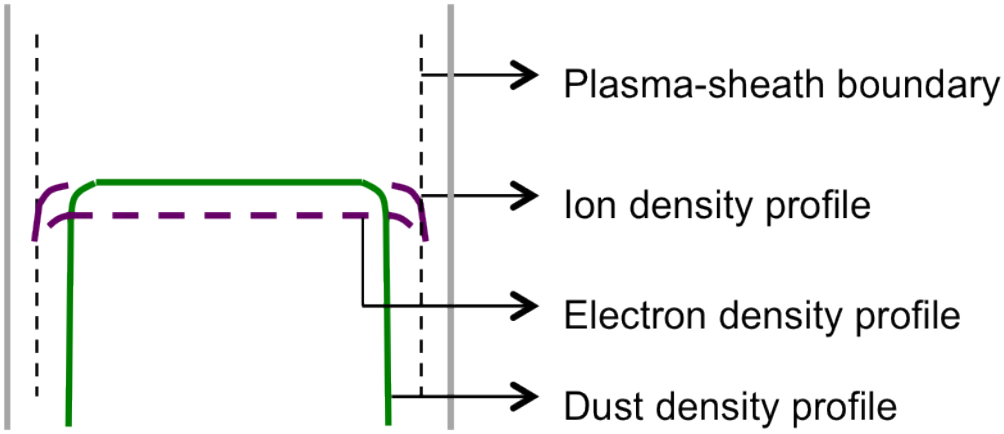

Figure 4.8: Plasma density profile as assumed in the global model.

A mass balance equation is solved in the plasma region for every species of ions and the electrons. In each balance equation, the species is created in the volume of the discharge due to collisions of electrons and ions, with molecules and atoms. The species is lost due to current to nanoparticles in the volume, and due to conduction current to the electrodes. The conduction current to electrodes consists of the flux of ions exiting the boundary between the plasma and the sheath.

$$Vn_e\nu_{iz}(f(E)) + \sum_i k_{cx,ij}n_i n_j = Vn_p\nu_{loss-np,i} + n_i A_{eff} v_{s,i} \tag{4.1}$$

Here V is the effective plasma volume, n_e is the electron density, ν_{iz} is the ionization frequency averaged over the electron energy distribution function, $k_{cx,ij}$ is a rate coefficient for charge transfer with atoms and molecules, n_p is the nanoparticle density, $\nu_{loss-np,i}$ is the ion loss frequency to nanoparticles, A_{eff} is the effective area of the plasma (which shall be discussed later), n_i is the ion density in the plasma, and $v_{s,i}$ is the velocity with which the ions transit the plasma-sheath boundary.

4.3.2 Plasma Sheaths

RF current passes through the sheaths on the surface of the electrodes. Characterizing the current flow through the sheaths and the voltage drop across them is important because these quantities determine the power coupled to the discharge via electron heating (as seen in the later sections). RF sheaths are also considerably thicker than DC sheaths, and their thickness needs to be calculated in order to estimate the effective volume of the plasma. Analysis of RF sheaths is made simpler by the following: (a) Ions in the discharge respond only to time averaged potentials (b) Electrons respond to instantaneous potentials and carry the discharge current. Figure 4.9 is a schematic of an RF sheath. The ion sheath is steady in time, however an electron front oscillates in phase with the applied RF voltage. The time averaged density profile is depicted with a dashed line.

4.3.2.1 Collisionless sheaths

Based on the above assumptions, and using conservation of mass and energy across the collisionless sheath, an analytical solution is obtained for ion and time averaged electron density profiles in the sheath. The profiles depend on the frequency of applied voltage, the total current density, and the sheath edge plasma density.

$$\frac{n_i(x)}{n_s} = \left[1 - H\left(\frac{3}{8}\sin 2\phi - \frac{1}{4}\phi\cos\phi - \frac{1}{2}\phi\right)\right]^{-1} \tag{4.2}$$

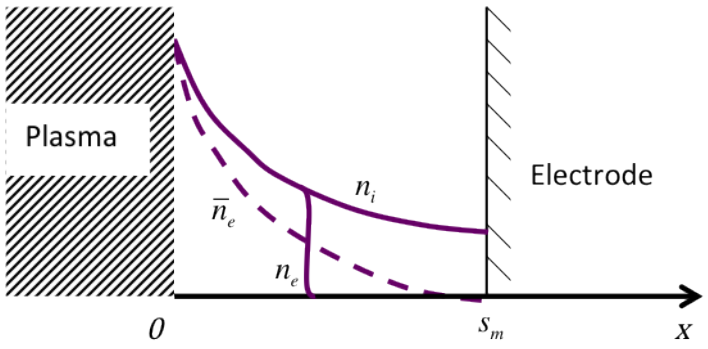

Figure 4.9: Schematic of an RF sheath.

$$H = \frac{J_1^2}{\pi e \epsilon_0 T_e \omega^2 n_s} \tag{4.3}$$

Here n_i is the ion density in the sheath, n_s is the sheath edge density, J_1 is the total current density, e is the unit charge, ϵ_0 is the vacuum permittivity, T_e is the electron temperature, ω is the frequency of applied voltage. Also $2\phi(x) = 2\omega t$.

Using the above solution and solving the Poissons equation in the sheath with appropriate boundary conditions, we obtain the collisionless Child Law sheath [45]. This equation connects the DC ion conduction current crossing the plasma-sheath boundary to the voltage drop across the sheath and the sheath thickness.

$$J_i = K_i \epsilon_0 \left(\frac{2e}{m_i}\right)^{1/2} \frac{\bar{V}^{3/2}}{s_m^2} \tag{4.4}$$

Here J_i is the ion current, $K_i \approx 0.82$ is a numerical constant, M is the mass of the ion, $\bar{V}$ is the time averaged potential drop across the sheath as experienced by the ions and s_m is the thickness of the ion sheath. If V_1 is the amplitude of the RF voltage across the sheath, then $\bar{V} \approx 0.83 V_1$. Additionally, most of the voltage drop can be assumed to occur at the sheath. Hence if V_{rf} is the peak-to-peak RF voltage, $V_1 = 0.5 V_{rf}$.

4.3.2.2 Collisional sheaths

When the mean free path of the ions is smaller than the sheath thickness, then the mass and energy conservation equations for the ions, across the sheath thickness should take into account the collisions undergone by the ions. Carrying out an analysis similar to the collisionless sheaths, a Child Law sheath is obtained for the collisional case, wherein the ion mean free path affects the ion current. The relation between average voltage drop across ion sheath and the RF voltage amplitude across the sheath is modified to $\bar{V} \approx 0.78 V_1$.

$$J_i = 1.68\epsilon_0 \left(\frac{2e}{m_i}\right)^{1/2} \frac{\bar{V}^{3/2}\lambda_i^{1/2}}{s_m^{5/2}} \tag{4.5}$$

4.3.3 Conduction current at the plasma-sheath boundary

The ion current on the right hand side of the Child Law sheath consists of the flux of ions exiting the plasma and entering the sheath. Since we are not solving the Poissons equation to obtain the electric field self consistently, we need to make an estimate of this ion flux. This involves making an estimate of sheath edge velocity and sheath edge density.

4.3.3.1 Sheath edge velocity

Let us begin by commenting on a case where a single type of positive ion is present in a low-collisionality discharge. If the mean free path of collision of the ion is smaller than the width of the sheath, it can be shown that the ion needs to exit the plasma with its Bohm velocity or its sonic speed, in order for a stable sheath to form. This is called the Bohm criterion.

$$u_{B,i} = \frac{eT_e}{m_i}^{1/2} \tag{4.6}$$

In a situation where multiple positive ions are present, the constraint is placed on

the sum of the velocities of the different species for stable sheath formation.

$$\sum \frac{n_{i,s}}{m_i u_{i,s}^2} = \frac{n_{e,s}}{T_e} \tag{4.7}$$

The constraint is satisfied if each type of ion reaches its individual Bohm velocity at the sheath edge. Ions would reach their individual Bohm velocities only if they remain collisionless in the much wider pre-sheath region that precedes the sheath. This occurs only in extremely low-pressure discharges. In most cases, the sheath and pre-sheath become collisional for some species of ions while they remain collisionless for others. In such a situation, individual Bohm velocities cannot be assigned to every species of ions.

Argon hydrogen discharges contain ions such as Ar^+, H_2^+, H^+, H, ArH^+, H_3^+ in different concentrations. In a simple approximation, the most dominant species among the ions was assigned the Bohm velocity. Electric field at the sheath edge was calculated based on the mobility of the most dominant ion, and its Bohm velocity.

$$\bar{E} \approx \frac{u_{B,i}}{\mu_i} \tag{4.8}$$

The velocity of the other ions is calculated based on their mobility and the electric field.

$$u_j = \bar{E} \cdot \mu_j \tag{4.9}$$

4.3.3.2 Sheath edge density

While we consider the ion density to be uniform throughout the plasma volume, the density falls from the centerline to the edges, so that the sheath edge density is only a fraction of the centerline density. In the present model, we assume that the fall in the density occurs sharply close to the sheath edge, as seen in 4.7. We therefore use a heuristic formula that predicts the sheath edge to centerline density in a parallel plane geometry over a wide range of pressures.

$$h_L = \frac{n_{i,s}}{n_{i,0}} = 0.86 \left(3 + \frac{l - 2s_m}{\lambda_i}\right)^{1/2} \tag{4.10}$$

Here, $n_{i,s}$ and $n_{i,0}$ are the plasma-sheath boundary, and centerline densities of a species of ion respectively. l is the distance between the electrodes, λ_i is the ion-neutral mean free path, and s_m is the mean thickness of the sheath.

In the situation where multiple ions are present, we consider the most dominant ion to determine the sheath to centerline density ratio. It is also reasonable to assume that all the species of ions in the system have identical spatial profiles. The effective area of the discharge is the electrode surface area multiplied by the sheath edge to centerline density ratio.

$$A_{eff} = 2\pi R^2 h_L \tag{4.11}$$

Using the sheath edge densities and the ion ion velocities the total ion conduction is estimated as follows.

$$J_i = e \sum_i n_i h_L u_i \tag{4.12}$$

The above expression is used in the left hand side of the Child Law sheath (Equations 4.4, 4.5). Although the Child Law sheath was derived for a single ion reaching Bohm velocity at the plasma-sheath boundary, a current density consisting of multiple ions is being used. This is inexact; however it is a reasonable approximation because the Child Law sheath is being solved using the properties of the most dominant ion in the discharge.

4.3.3.3 Most dominant ion species in discharge

The simulation, at the outset, considers the Ar^+ ion to be the most dominant in the plasma. The species balance equations solved in the bulk plasma yield steady state densities of all species of ions. The H_3^+ ion is seen to be the most dominant of all light ions. When the following relation between the densities of heavy ions (Ar^+,ArH^+) and

the H_3^+ is violated, the simulation begins to consider H_3^+ as the most dominant

$$(n_{Ar^+} + n_{ArH^+}) < 3.6 n_{H_3^+} \tag{4.13}$$

The relation is based on the fact that the Bohm velocities of ions vary as the square root of their masses. In collisionless plasma, therefore, if the fluxes of Ar^+, ArH^+ ($\sim 40amu$) and H_3^+ ($\sim 3amu$) are equal, then their densities must be in the ratio of $\sqrt{40/3}$. The above expression only qualitatively estimates the switch of the plasma from being a heavy ion dominated one to a light ion dominated one. The switch is also an abrupt one, and in reality, we would expect the transition to be smoother.

4.3.4 Electron heating

Electron heating is strongly coupled to the current flowing through the RF discharge. The Ohmic heating of electrons in the bulk, as well as the stochastic heating, due to oscillating sheaths, can be expressed in terms of the total current density. The Ohmic heating can be expressed in terms of the dc plasma conductivity, and the current density.

$$\bar{P}_{ohm} = \frac{1}{2} J_1^2 \frac{l - 2s_m}{\sigma_{dc}} (\pi R^2) \tag{4.14}$$

We can express the total current density in terms of the RF voltage amplitude V_1, the frequency of the applied voltage, the electron temperature, and plasma-sheath boundary density. This expression is valid for single ion plasma, with the ions exiting the plasma sheath boundary with Bohm velocity.

$$\frac{J_1^2}{n_s} \approx 1.73 e \epsilon_0 \omega^2 T_e^{1/2} V_1^{1/2} \tag{4.15}$$

Next, we make following assumptions.

- The heuristic relation holds for the case of multiple positive ions in pristine plasma.
  $h_L = n_s/n_0 = n_{s,e}/n_{0,e} = \sum n_{s,i} / \sum n_{0,i}$

- When nanoparticles are present in the discharge, the ion density profile deviates only slightly from the relation. However, the electron density deviates considerably due to loss to nanoparticles. At the sheath edge though, we assume that the ion and electron densities are equal $n_{s,e} = \sum n_{s,i}$. Therefore, the bulk to sheath edge density of electrons is calculated as follows

$$\frac{n_{s,e}}{n_{0,e}} = \frac{\sum n_{s,i}}{n_{0,e}} = \left[\frac{n_s}{n_0}\sum n_{0,i}\right]\frac{1}{n_{0,e}} \tag{4.16}$$

Using the expression for the current density, Ohmic heating can be expressed as follows.

$$\bar{P}_{ohm} = 1.73\frac{m}{2e}\frac{n_s}{n_0}\frac{\sum n_{0,i}}{n_{0,e}}\nu_m\epsilon_0\omega^2 T_e^{1/2}V_1^{1/2}(l-2s_m)(\pi R^2) \tag{4.17}$$

The expression for stochastic electron heating is derived assuming that the velocity electron sheath oscillation is smaller than the electron thermal velocity. At the two sheaths the collisionless power transfer to electrons can be expressed as the following.

$$\bar{P}_{stoc} = 0.45\left(\frac{m}{e}\right)^{1/2}\epsilon_0\omega^2 T_e^{1/2}V_1(2\pi R^2) \tag{4.18}$$

4.3.5 Electron power balance

In steady state, the power gained by electrons is dissipated via collisions in the plasma L_c, electron current loss to nanoparticles in the volume $L_{e,np}$, and via conduction current loss to electrodes $L_{e,w}$.

$$\bar{P}_{ohm} + \bar{P}_{stoc} = L_c + L_{e,w} + L_{e,np} \tag{4.19}$$

$$L_c = eVn_e\left(\sum \varepsilon_{iz}\nu_{iz}(f(E)) + \sum \varepsilon_{ex}\nu_{ex}(f(E))\right) \tag{4.20}$$

$$L_{e,w} = A_{eff}n_e u_{e,s}\left(\epsilon_e + V_{sh} + \frac{1}{2}T_e\right) \tag{4.21}$$

$$L_{e,np} = \pi e R_p^2 n_p n_e V\int_{-Vp}^{\infty}(E+V_p)\left(1+\frac{V_p}{E}\right)\sqrt{\frac{2eE}{m_e}}f(E)E^{1/2}dE \tag{4.22}$$

Electron flux to the wall is equal to the ion flux.

$$n_e u_{e,s} = n_i u_{i,s} \tag{4.23}$$

The electron conduction current passes through the electrode at a short moment in the RF cycle when the oscillating sheath thickness goes to zero. In Equation 4.21 $\varepsilon_e \approx 2T_e$ is the average energy of the electrons. The electrons carry with them an additional energy of $V_{sh} + 1/2T_e$ as they are lost to the wall. Here V_{sh} is the wall floating potential.

4.3.6 Total power balance

Finally, the total power dissipated in the discharge is given by electron power loss, electron and ion currents to the nanoparticles $L_{t,np}$, well as ion heating in the RF sheaths as the fall through a time averaged potential $\bar{V}$, $L_{i,w}$.

$$\bar{P}_{abs} = L_c + L_{e,w} + L_{i,w} + L_{t,np} \tag{4.24}$$

$$L_{i,w} = A_{eff} \sum n_i u_{i,s} \bar{V} \tag{4.25}$$

$$L_{t,np} = \pi R_p^2 e n_p n_e V \int_{-Vp}^{\infty} \left(1 + \frac{V_p}{E}\right) \sqrt{\frac{2eE}{m_e}} f(E) E^{3/2} dE \tag{4.26}$$

4.3.7 Current to nanoparticles

Steady state current to nanoparticles is calculated using the Orbital Motion Limited(OML) theory [46]. OML theory is valid when the radius of the nanoparticle is much smaller than the linearized Debye length $R_p << \lambda_L$

$$n_e \int_{-Vp}^{\infty} \left(1 + \frac{-V_p}{E}\right) \sqrt{\frac{2eE}{m_e}} f(E) \sqrt{E} dE = \sum_i n_i \left(1 - \frac{eV_p}{kT_i}\right) \sqrt{\frac{8kT_i}{\pi m_i}} \tag{4.27}$$

4.3.8 Electron energy distribution

Electron energy distribution is obtained by using a zero dimensional time dependent Boltzmann equation solver. In addition to the cross sections of interaction between

electrons and gas atoms and molecules, coulomb scattering and inelastic scattering cross sections of electrons with nanoparticles are used by the Boltzmann solver. The Boltzmann equation is not solved simultaneously with the rest of the unknown quantities. Therefore an initial electron energy distribution function (EEDF) is obtained using an arbitrary reduced electric field value. The system of equations is solved for this EEDF. Based on the error obtained, a second guess is made on the reduced electric field, and is input to the Boltzmann solver along with the updated value of electron and ion densities obtained from the solution to the system of equations. This loop is exited after the absolute value of the error goes below a prescribed tolerance.

4.4 Simulation results

The following parameters need specification for the simulation: gas composition in terms of $Ar : H_2$ gas ratio, the gas pressure, the nanoparticle size and density, the chamber and electrode geometry and size. Either the total power absorbed by the discharge or the peak-to-peak amplitude of voltage applied at the powered electrode needs to be specified.

Simulations are performed for conditions typically found in capacitively coupled RF discharges used for silicon nanoparticle synthesis. The radius of the cylindrical discharge chamber is 6 cm, and the width is 4 cm. The chamber has parallel plate electrodes of 6 cm radius. The nanoparticle size is fixed at $R_p = 50$ nm.

4.4.1 Effect of hydrogen addition

In this section, discharge characteristics are examined for different argon hydrogen gas ratios, at different chamber pressures. The nanoparticle density is low at $10^3\ cm^{-3}$. Total power absorbed is fixed at 3 W.

Figure 4.10 shows the reduction of plasma density as hydrogen concentration in argon increases. The plasma quenching as a function of H_2 content is seen to be pressure dependent. At 10 Pa, the quenching is slower compared to the discharge at 50 Pa. Hydrogen gas has the greatest effect on the discharge when it is present in trace quantities; with the increase of H_2 concentration, its effect on plasma density reduces. Figure 4.11 shows the composition of plasma in terms of the constituent ion species at 10, and 50 Pa.

The reduction in plasma density can be explained as follows. In both pure argon and argon-hydrogen discharges, electron impact ionization of Ar is the primary production process. The Ar^+ ion undergoes an efficient H atom transfer reaction with H_2 to produce ArH^+. The ArH^+ ion undergoes a proton transfer reaction with H_2 to produce H_3^+. As the H_2 concentration increases there is an increase in the density of H_3^+, a light ion whose lifetime in the discharge chamber is shorter than the heavy Ar^+, and ArH^+ ions. The presence of shorter lifetime ions leads to reduction of steady state plasma density.

H_3^+ ion fraction becomes predominant for lower fractions of H_2 gas, as the pressure increases. This is because the increased collisionality at higher pressures leads to more ion-molecule collisions that form H_3^+. H^+ and H_2^+ remain less dominant through the investigated pressure range. H_2 has a smaller effect on plasma density and composition at higher concentrations because there is lesser argon available for electron impact ionization, inhibiting plasma production in the first place.

Figures 4.12 and 4.13 plot the electron energy distribution at different fractions of H_2 gas in Ar. There is an increase in the fraction of low energy electrons, accompanied by a reduction of population around the 10 eV range. Clearly these electrons are losing energy to the excitation of hydrogen molecules to various vibrational and rotational levels, because the ionization potentials of both argon and hydrogen are around 15 eV. The high energy tail however shows an increase in the population with increasing H_2.

This is due to the need to keep up the ionization in the discharge as the plasma density, and consequently electron density reduces.

The average particle floating potential reduces due to the presence of hydrogen gas (Figure 4.14). The plasma composition varies differently with H_2 addition at different pressures. This is reflected in the different curve profiles of the particle potential variation. The constitution of ion current to the nanoparticles varies with the ion composition. Figure 4.15 plots the flux of each type of ion normalized to the total ion flux impacting the nanoparticle surface, for 1 percent and 4 percent H_2 gas concentrations. At 1 percent, H_3^+ and Ar^+ ions are equally dominant. At 4 percent H_2, H_3^+ is the most dominant ion.

4.4.2 Effect of increasing nanoparticle density

In this section, discharge characteristics are examined for different nanoparticle densities, at 50 Pa chamber pressure. Total power absorbed is fixed at 3 W.

As the nanoparticle density increases, more electrons are lost to the nanoparticles; this reduces the electron density in the volume. At fixed power, the reduced number of electrons absorb more power (as evidenced in the plots of EEDF, 4.18) and there is an increase in the fraction of high energy electrons. This causes increased ionization, leading to an increased ion density as shown in Figure 4.16. The fraction of different species of ions do not show significant variation with increase in the nanoparticle density, as shown in Figure 4.17. Figure 4.18 compares the EEDFs at different nanoparticle densities for two different concentrations of H_2. With the increase in nanoparticle density, there is an increase in the fraction of electrons in the low energies as well as in the high energy tail. The increase in the high-energy fraction is for maintaining ionization in the discharge even as the electron density in the volume reduces. The increase in the low energy fraction, as seen in Figure 4.19 is due to the coulomb collisions of the electrons

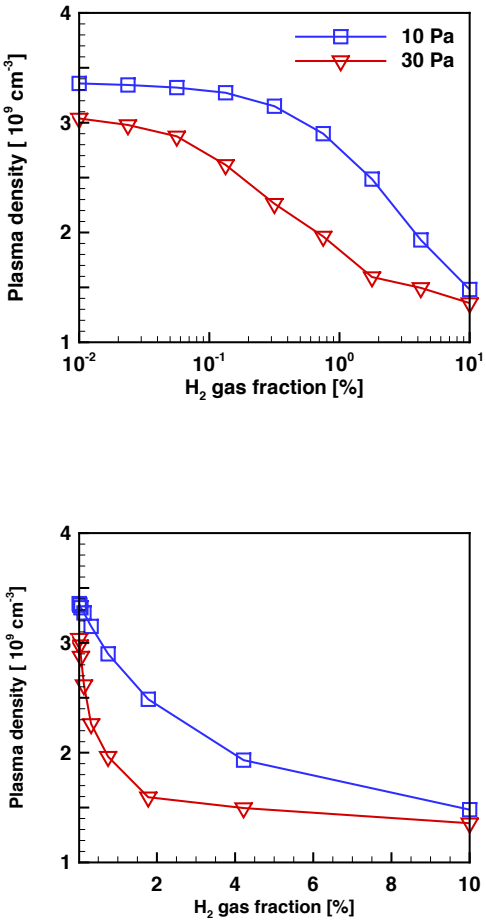

Figure 4.10: Plasma density as a function of H_2 : Ar ratio. Power absorbed: 3 W, nanoparticle density: 10^3 cm^{-3}.

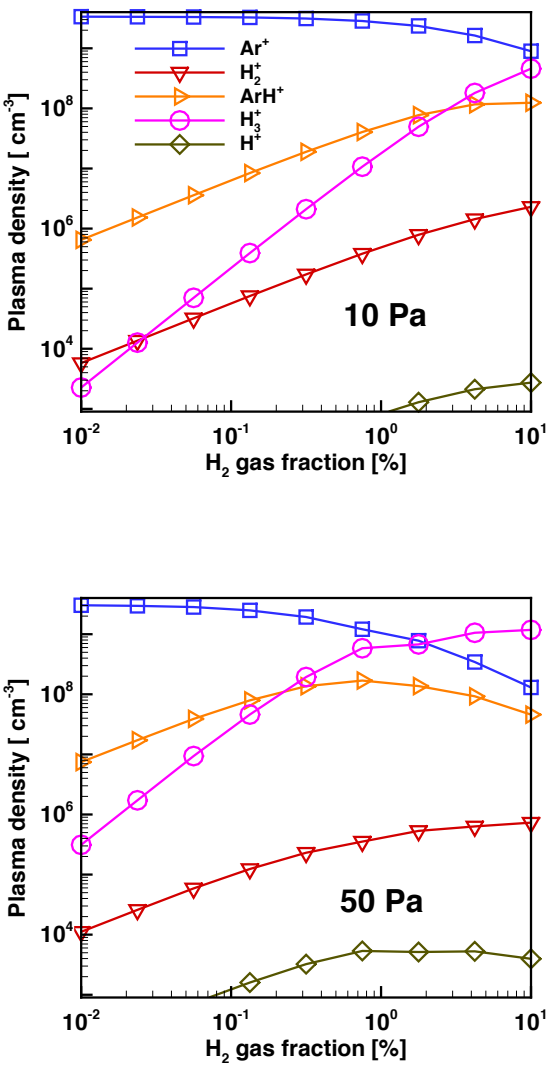

Figure 4.11: Ion composition of plasma as a function of $H_2 : Ar$ ratio. Power absorbed: 3 W, nanoparticle density: 10^3 cm^{-3}.

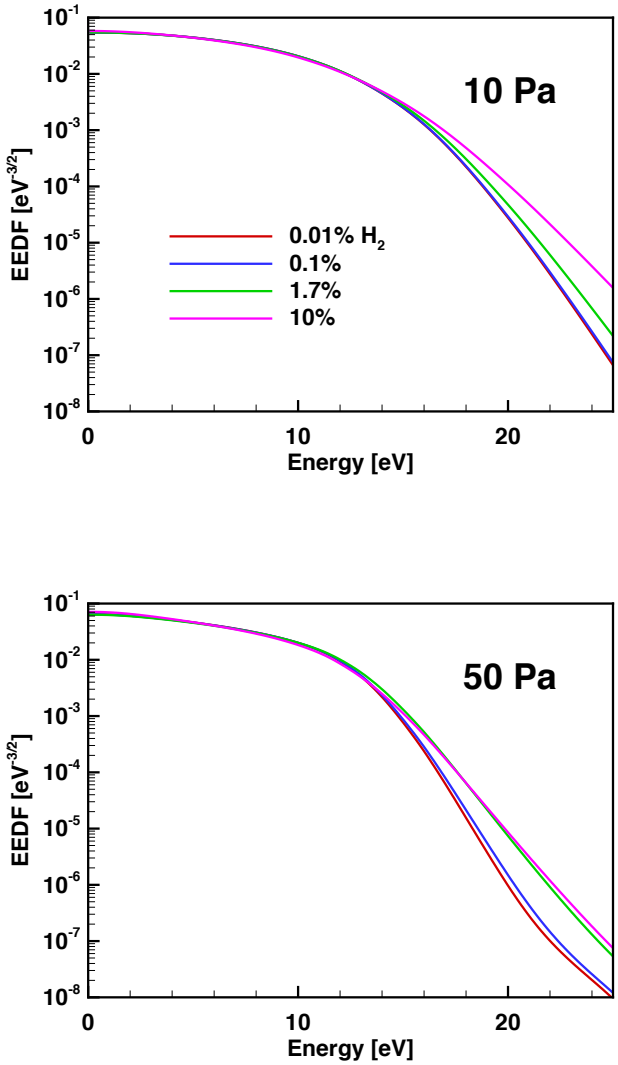

Figure 4.12: Electron energy distribution at different fractions of H_2 gas. Power absorbed: 3 W, nanoparticle density: 10^3 cm^{-3}.

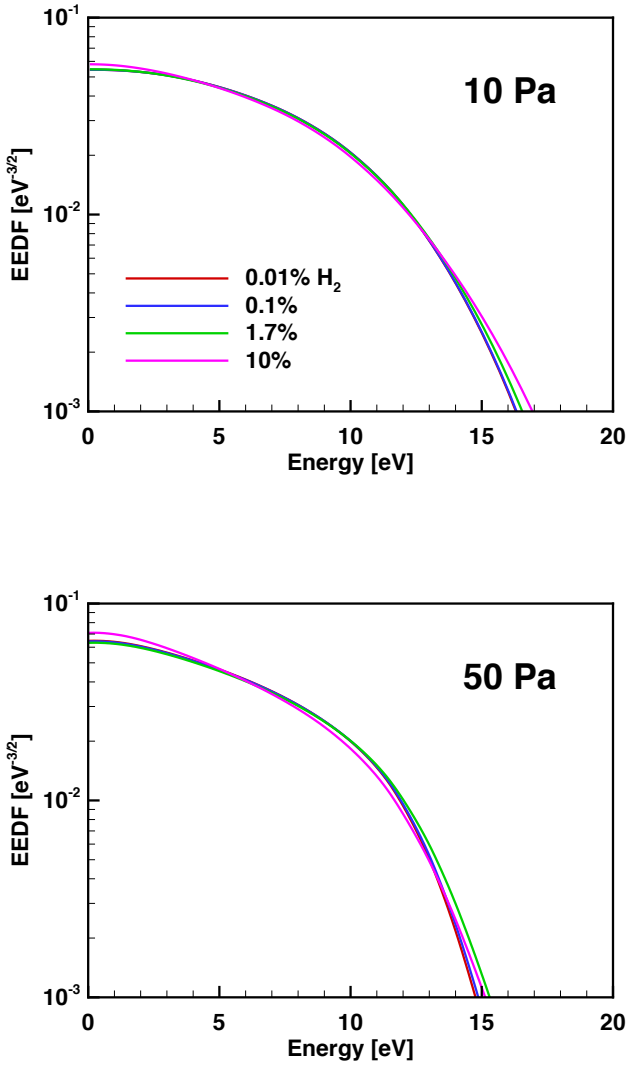

Figure 4.13: Electron energy distributions shown in Figure 4.12 zoomed at lower energies.

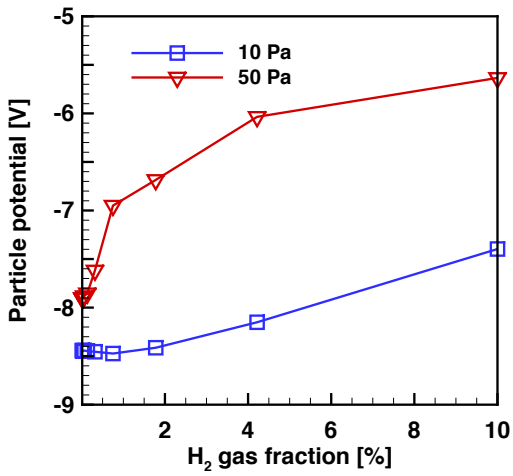

Figure 4.14: Particle floating potential as a function of H_2 fraction. Power absorbed: 3 W, nanoparticle density: 10^3 cm^{-3}.

with the nanoparticles. The coulomb scattering cross section for interaction between electrons and nanoparticles is large for low energy electrons. This scattering prevents the diffusion of electrons in energy space, from low to high energies, leading to the peak seen between 0 and 0.5 eV. Particle potential reduces as the nanoparticle density increases, as seen in Figure 4.20, due to the decrease in electron density. The fraction of each species in the ion current to nanoparticles does not show a significant change with increase in nanoparticle density, as seen in Figure 4.21. The flux of each species has been normalized to the total ion flux, in the figure.

4.4.3 Comparison with experiments

Probe measurements were performed in the laboratory to study discharge characteristic in CCP RF plasmas and their variation with argon hydrogen ratio in the feed gas. Table

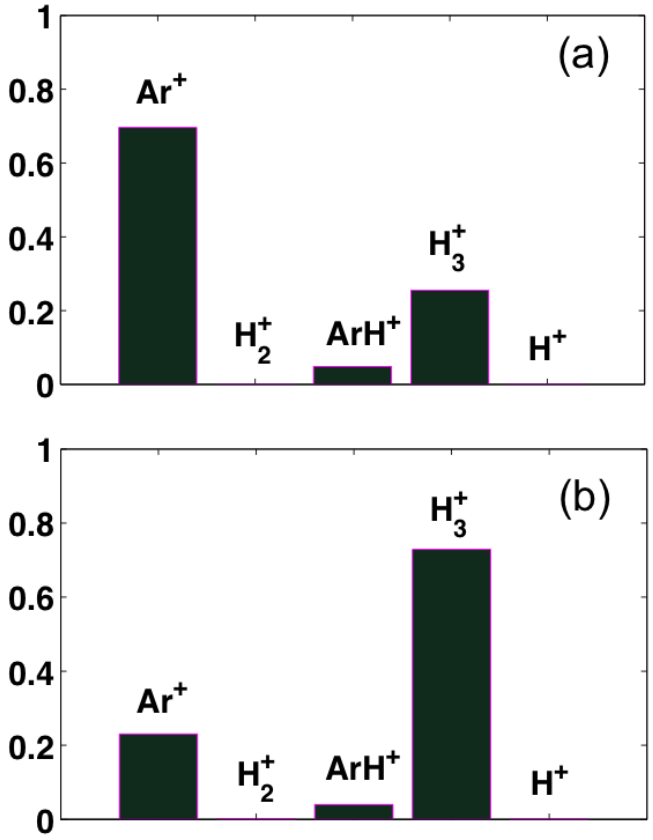

Figure 4.15: Fractions of ion species in the ion current to nanoparticles at (a) 1 percent H_2, and at (b) 4 percent H_2, in argon. Discharge pressure: 50 Pa, power absorbed: 3 W, nanoparticle density: $10^3 cm^{-3}$.

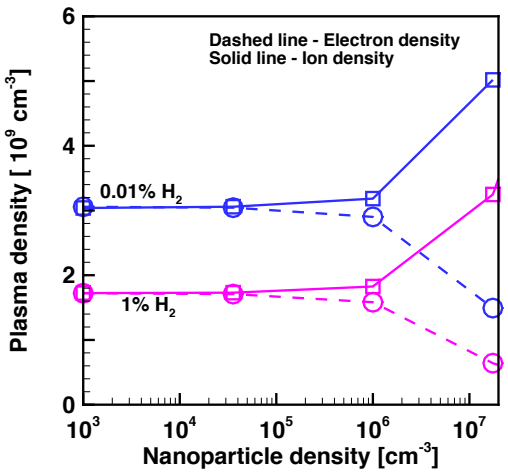

Figure 4.16: Plasma density as a function of nanoparticle density. Pressure: 50 Pa, Power absorbed: 3 W.

4.2 lists the parameters that were fixed in the experiment as well as simulations.

A comparison of measured and calculated plasma density, shown in Figure 4.22 indicates that the simulation is able to calculate the plasma density within a reasonable approximation, as well as capture the trend of density reduction with increased H_2 concentration. The measured and calculated electron energy distributions show a similar trend as well, as seen in Figure 4.23. There is a reduction of electron fraction in the 5-15 eV range with the addition of H_2 because the thresholds for rotational and vibrational excitations undergone by hydrogen molecules fall in that range. The electrons are pushed to lower energies below 5 eV.

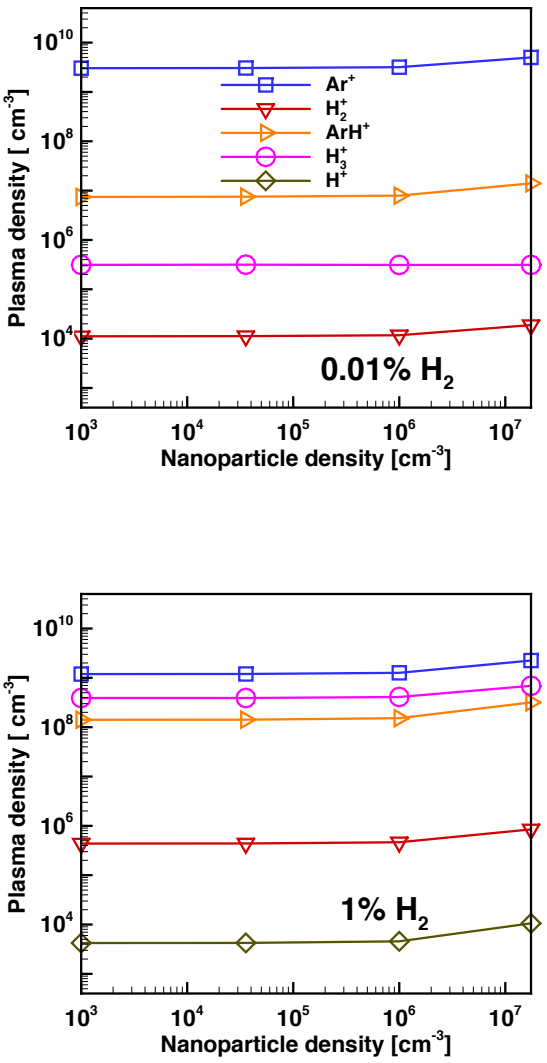

Figure 4.17: Ion composition of plasma as a function of nanoparticle density. Pressure: 50 Pa, Power absorbed: 3 W.

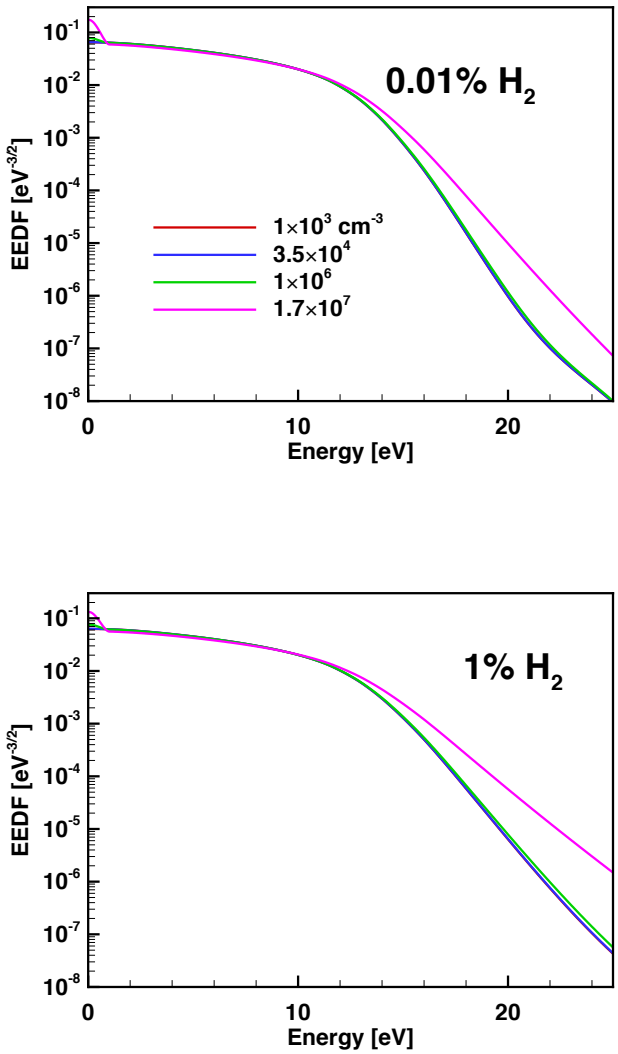

Figure 4.18: EEDF's at different nanoparticle densities for two different concentrations of H_2.

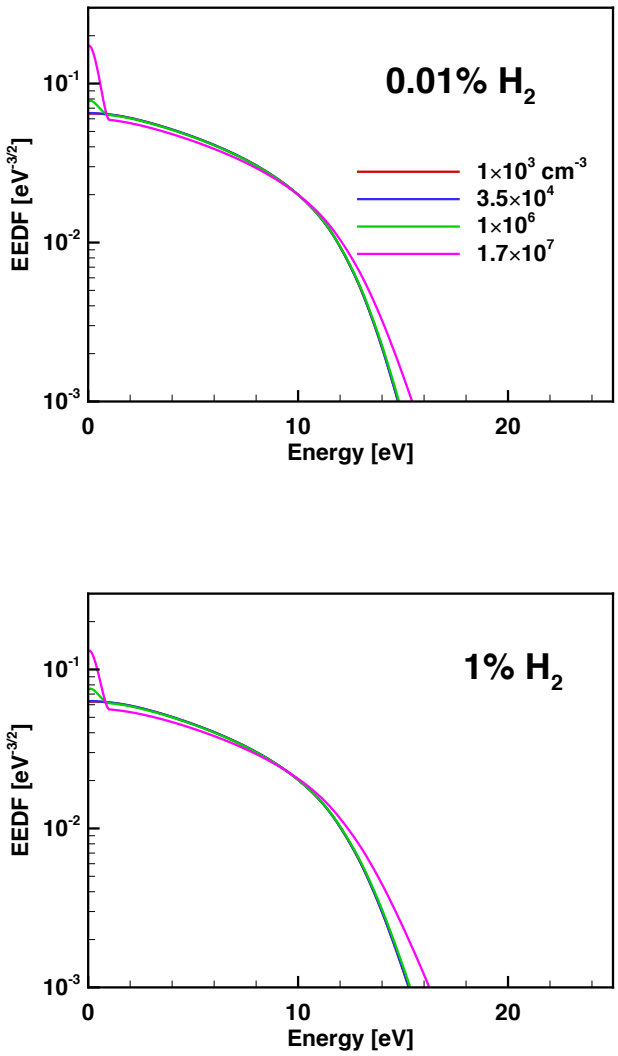

Figure 4.19: EEDF's in Figure 4.18 zoomed in the low energy region.

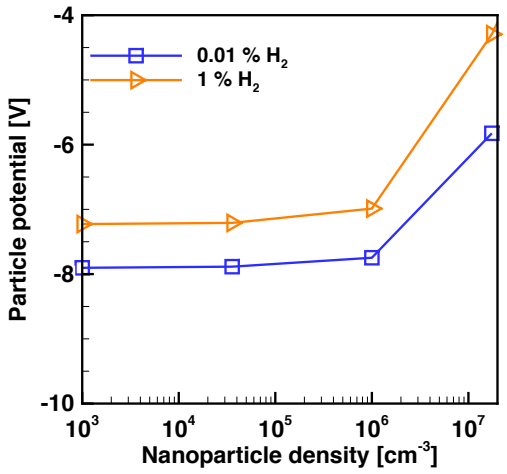

Figure 4.20: Particle potential as a function of nanoparticle density. Pressure: 50 Pa, Power absorbed: 3 W.

Table 4.2: Plasma discharge parameters for simulation and experiment

Parameter	Experiment	Simulation
Cylinder radius	7.62 cm	6.00 cm
Cylinder width	5.08 cm	4.00 cm
RF voltage (peak-to-peak)	300 V	300 V
Nanoparticle density	Zero	Negligible (10^3 cm^{-3}, 50 nm)
Chamber pressure	66 Pa	66 Pa
% H_2 in Ar	0, 10, 20	0.01, 10, 20

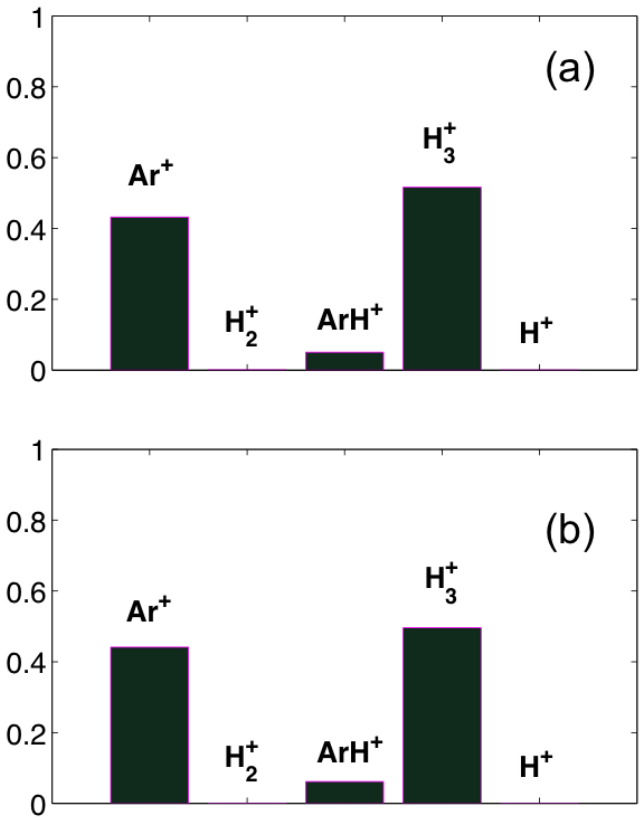

Figure 4.21: Fractions of ion species in the ion current to nanoparticles at nanoparticle density of (a) 10^3 cm^{-3} and, (b) 1.7×10^7 cm^{-3}, in argon. Discharge pressure: 50 Pa, power absorbed: 3 W, 1 percent H_2 concentration.

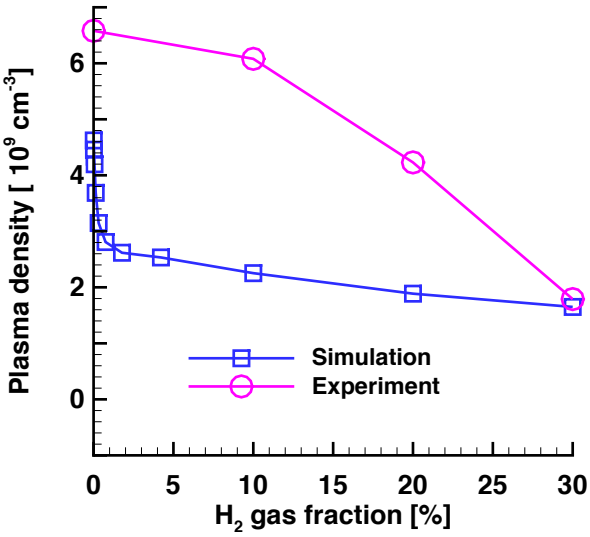

Figure 4.22: The variation of plasma density with H_2 concentration in Ar gas.

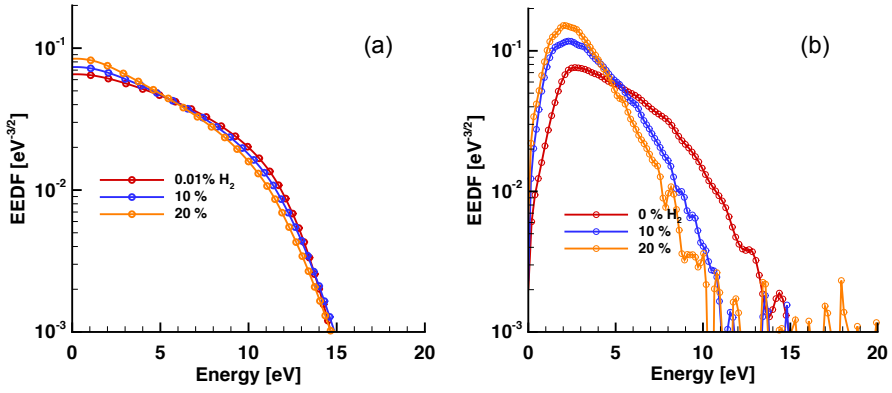

Figure 4.23: The variation of EEDF with H_2 concentration in Ar gas. (a) Simulation, (b) Experiment.

4.5 Conclusion

A self consistent volume averaged model of argon hydrogen dusty plasma was presented in this chapter. Given the operating conditions of the discharge, and the size and density of spherical dust particles inside it, the model predicts the plasma density and composition, the electron energy distribution and the average particle charge. It is seen that trace quantities of hydrogen present in argon discharge alter the plasma density and composition. The average particle potential reduces in the presence of H_2, leading to impaction of ions at lower energies. If H_2 gas concentration is 1 percent or more in the discharge, in pressures between 10-50 Pa, hydrogen ions, especially H_3^+ constitute a considerable fraction of ion current to the nanoparticles. The hydrogen ions may play an important role in the nanoparticle surface reactions. The consequences of H_2 effects on discharge characteristics in the context of influencing nanocrystal synthesis will be discussed in the following chapter.

Chapter 5

Particle Charging and Ion Impaction in $Ar - H_2$ Dusty Plasmas

5.1 Introduction

The focus of this chapter is the study of plasma interaction with nanoparticles in a low temperature discharge. Particle in Cell Monte Carlo (PIC-MC) simulations were performed to determine the steady state charge that a nano-sized particle would acquire in a discharge. The simulations reveal details of how the particle interaction with plasma changes as the discharge pressure is increased. Pure argon plasma was firstly studied. Subsequently, a composition that mimics a discharge in argon gas mixed with trace quantity of hydrogen gas was studied (Ar^+ and H_3^+ ions were considered in this composition). PIC-MC simulations show that ion current to the nanoparticle firstly increases and subsequently decreases as the discharge pressure is increased. In the case where two different types of ions are present as in the case of argon-hydrogen

discharge, the individual ion currents peak at different pressures based on the nature of their collisional interaction with the background gas. Finally an analytical model was developed to calculate the potential of a nano-sized particle if the particle size, plasma pressure and composition are known.

5.1.1 Motivation

With the advent of new technologies in lighting [47], energy conversion [48] and medicinal biology [49], nanocrystalline materials of specific sizes and optical and electronic properties have become important [11]. CCP RF discharges are being used to gas-phase synthesize semiconductor nanocrystals (NCs) with extremely desirable and tunable properties [50]. The reactors are typically flow-through and operate in the pressure ranges of a few hundreds of mTorr through a few tens of Torr. The generic stages in the synthesis process are as follows.

Argon mixed with a small percentage of silane precursor is flowed through a low pressure discharge chamber. Immediately on injection, almost all of the precursor gas dissociates in the plasma to form chemically reactive species. These species nucleate and chemically cluster to form a high density of small size silicon particles. The chemistry of argon silane plasmas, and routes of cluster formation are well described in references [9, 51, 42, 52]. The small sized clusters can be positively or negatively charged. They can also be neutral. Once the clusters reach a critical diameter, they begin to agglomerate to form larger particles. The large particles become negatively charged due to the high mobility of electrons compared to positive ions in the plasma. The similar charge on particles repels them from one another and also from the negatively charged chamber walls, thus preventing diffusion losses to the walls. The similar charge on the particles also prevents further agglomeration resulting in a monodisperse sample of particles. They continue to grow, however, due to the infrequent impingement of reactive positively

charged species from the discharge, until they are convected out of the chamber by the flowing gas, and are collected downstream on a mesh. Depending on the gas flow rate, the particles continue to reside in the chamber after attaining their final size. Their total residence time is typically in the range of a few milliseconds [11]. Depending on the power absorbed by the discharge, either amorphous or crystalline silicon nanoparticles, whose surface is terminated by hydrogen, are obtained. Termination of a silicon bond on the surface of the nanoparticle is called 'passivation'. Surface passivation is seen to improve the electronic properties of the nanocrystal.

Why does plasma synthesis produce highly crystalline mono disperse particles? The answer lies in the complexities of particle formation agglomeration in the discharge. It likely also lies in the interaction of plasma with the agglomerated nano-sized particles. In this context our study becomes relevant. It is also particularly relevant to study particle interaction with plasma in argon-hydrogen discharge for the following reason. Atomic and molecular hydrogen is released in the discharge due to the stepwise dissociation reactions undergone by silane [51] in argon plasma. At typical operating powers, silane completely dissociates in the discharge, implying that if $Ar : SiH_4$ mixture consists of even 1% silane, $\sim 2\%$ H_2 is released in atomic and molecular form. Thus, the clusters and particle aggregates reside in a hydrogen rich environment before they are deposited.

A brief review is presented here of the work done to understand hydrogen interaction with silicon. Molecular dynamics simulations of PECVD by Sriraman and co-workers studied the interaction of Si film surface with H radicals. They indicate that hydrogen atoms diffuse through the silicon surface, causing the silicon matrix to transform from being disordered to an ordered one [14], thus aiding crystallization. Experimental studies of PECVD that added hydrogen gas to the *feed gas mixture*, concluded that the particles constituting Si film became smaller, and more crystalline with significant H_2 addition, and the deposition rate decreased [53, 13]. These effects are in line with the theory that

excess hydrogen suppresses dissociation reactions of silane, causes smaller agglomerates which in turn, are easier to crystallize. Surface hydride coverage also varied with the change in feed gas constitution. Particles formed in pure argon silane discharge were seen to be terminated by di-, and trihydrides, while under the effect of excess H_2 dilution, silicon mono-hydride was predominant on the surface [54]. The silicon surface could also contain a 'dangling bond' also called a defect due to its undesirability, where the silicon atom is not terminated by any entity. A general trend of increasing defect density with the atomic weight of the inert gas was observed [55].The most interesting results, however, are seen in experiments of gas phase Si NC synthesis in flow through plasma reactors [12]. Hydrogen was added, not at the gas inlet stage, but in a region of the discharge where the particles have already attained their final size. We could call this region the afterglow region because the experiment was conducted in a vertical flow through reactor, and hydrogen was added to the discharge below the electrodes, and just above the area where particles are collected. The chamber pressure was at 1.4 Torr, the discharge was powered by a 13.56 MH radiofrequency power supply. This experimental setup produced SiNC with the highest ever recorded photoluminescence quantum yield (PLQY). The H_2 gas is added after the particle formation stage was seen to be cooling the particles, due to its high thermal conductivity, thus locking their crystal structure. Additionally an excess of H radicals were delivered to the particle surface, aiding in passivation. Thus, hydrogen plays a complex role in determining the properties of the nanoparticles.

The scope of the present work is however, limited to understanding how the most basic interaction of a nano-sized particle in plasma, namely, particle charging, is effected when hydrogen ions are present. No simulation work, to the knowledge of the author, was done to understand the role of hydrogen in effecting plasma-particle interactions in flow-through argon discharges. Experimental and simulation work on plasma enhanced

chemical vapor deposition (PECVD) using argon silane discharges, that is available in the literature [56, 57], cannot be extended to flow through reactors. PECVD involves the formation of a planar Si film on an electrode that may be biased. While in the flow-through discharges, Si is present as spherical particles immersed in the discharge at a floating potential. Given that considerable H_2 is released in $Ar - SiH_4$ discharge, and the experimental evidence of effects on Si properties depending on $Ar : H_2 : SiH_4$ ratios in the feed gas mixture, study of hydrogen gas influence becomes important. In case of the nanoparticles, the particle potential limits the energy with which ions impact its suface. Collisions, on the other hand, effect the standard deviation of the energy distribution. When a heavy atom like argon impacts the particle, its energy is efficiently transferred. When a light ion like triatomic hydrogen impacts it, the energy transfer is inefficient due to difference in the masses of the particle and ion. Additional energy from the impaction may be consumed in disassociation of the ion into atomic hydrogen, or in creating a dangling bond[58]. In this context, study of particle charging in a plasma containing a mixture of argon and hydrogen ions becomes relevant.

5.1.2 Background

A small sized particle (whose radius is much smaller than the Debye length) immersed in plasma quickly becomes negatively charged due to the highly mobile electrons accumulating on its surface. An electric field develops around it to repel further influx of electrons and attract the positively charged ions. The ions, on impacting the particle can be assumed to combine with the available free electrons on the surface and get neutralized. In a quasi-steady state a balance is created between the electron and the ion fluxes to the particle, and the particle is said to acquire a steady state charge. The net resultant charge, though, is typically negative. The particle is therefore at a lower potential compared to the undisturbed part of the plasma around it. There are well

established theories to calculate the floating potential of a dust particle. Among them, OML theory is the most frequently used [59]. The basic premise of OML theory is that motion of ions moving towards the nanoparticle is only governed by energy and angular momentum conservation. Therefore, an ion would either reach the nanoparticle surface or just be deflected by the field and not reach the surface. By this definition, ion-neutral and electron neutral collisions are ignored. OML theory also ignores the fact that the interaction potential between an ion and the nanoparticle consists of two components; one comprising the attractive potential due to the unlike charges of the ion and the particle, and a repulsive potential associated with the angular momentum of the ion. As a result of these competing potentials, some ions become trapped in potential wells around the particle. The presence of these trapped ions causes the potential drop around the particle to be 'shielded' from the rest of the plasma. Therefore, the applicability of OML theory becomes severely restricted to very low pressure, collisionless plasmas. As the pressure begins to increase, even when the ion mean free path is greater than the Debye length, collisions begin to effect the particle charge. Several works have studied effect of trapped ions, and ion-neutral collisions on particle charging[**?**, **?**]. No work to the knowledge of this author however, was done to study charging in the presence of multiple types of ions.

In the following sections, particle charging in argon discharge is studied via PIC-MC. Subsequently, charging in the presence of two different ions is studied. The aim is to understand the role of collisions in effecting particle charging.

5.2 Monte Carlo simulations

A PIC-MC simulation is carried out on a spherically symmetrical one dimensional domain; the schematic is seen in Figure 5.1. One end of the domain is the particle surface, while the other is located in the undisturbed part of the plasma where ions and electrons

are in a Maxwellian distribution. The nanoparticle being considered in the simulation is perfectly spherical and does not experience the presence of other particles in its vicinity; i.e. it is an isolated particle. The domain is 5 Debye Lengths long, and is discretized into 1000 cells with the cell size increasing slightly exponentially towards the outer edge. A detailed description of the PIC-MC simulation algorithm is given in Gatti et al [60]. In this section the same is discussed very briefly to familiarize the reader with the code.

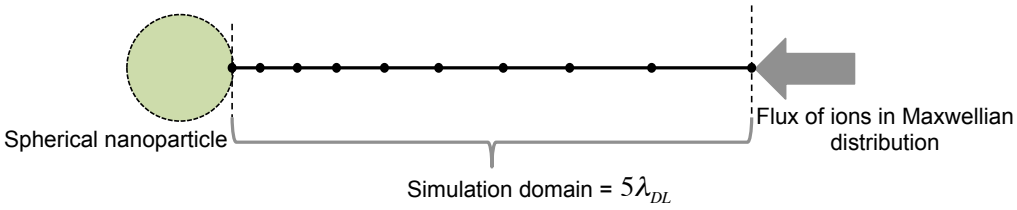

Figure 5.1: A schematic of the spherically symmetric one dimensional domain used for MC simulations.

At time zero, the nanoparticle is assigned the potential calculated by the OML theory. The initial potential profile in the domain is given by the Debye-Huckel theory. No ions are present at time zero, and the domain is gradually populated with ions entering from the outer edge. Equations of motion are solved for every ion, and its position, velocity and acceleration is tracked. The electrons are considered to be in maxwellian distribution and are treated as a fluid. Collisions of ions with neutral gas are considered. Null collision method [61] is used to determine if an ion has collided with a gas atom after every time step. Two types of collision are considered: charge exchange, and elastic scattering. In case of an elastic collision, random collision angles are generated, and new ion velocity and acceleration are calculated. In case of an inelastic collision, such as charge exchange, the newly formed ion is assigned a velocity from the Maxwellian distribution of the neutral gas.

After marching in time for half a micro second, once the ions relax into the potential, the simulation switches to a self-consistent mode, with the Poisson's equation being solved to obtain the potential profile at every time step. For the boundary conditions of the Poisson's equation, the potential on the particle surface is determined by the electron and ion currents, and thus, the net charge on the surface. On the outer boundary, the gradient of the potential is considered zero. The density profile of ions is obtained form the spatial location of the individual ions being tracked. However, electron density profile is being determined by the Boltzmann relation, and is therefore dependent on the potential profile. Since the potential profile and electron density profile depend on each other, the Poisson's equation is solved by iteratively updating the electron density and potential profiles.

At the end of a time step, the ion reaching the particle surface are tracked and a histogram of the energies of ion impaction is recorded. The simulation runs for 80 microseconds, by which time the particle potential obtains a time averaged steady state value. The size of the time step is limited by the need for resolving the ion motion in the region closest to the particle surface, where there is maximum acceleration. It turns out to be about 1 picosecond.

5.2.1 Collision tracking

Gatti and coworkers had defined a region around the nanoparticle called the 'capture sphere'. It shall be described in detail in section 5.3.3. The radius of this sphere is the distance at which the Debye-Huckel potential around the nanoparticle drops to a 'small' value. At the edge of the capture sphere, a charged particle born in that location would have a potential energy equal to the gas kinetic energy. Once an ion enters the capture sphere, the collisions it undergoes are tracked until (a) the ion reaches the nanoparticle surface, or (b) leaves the capture sphere. Figure 5.2 describes the kind of collision

information collected.

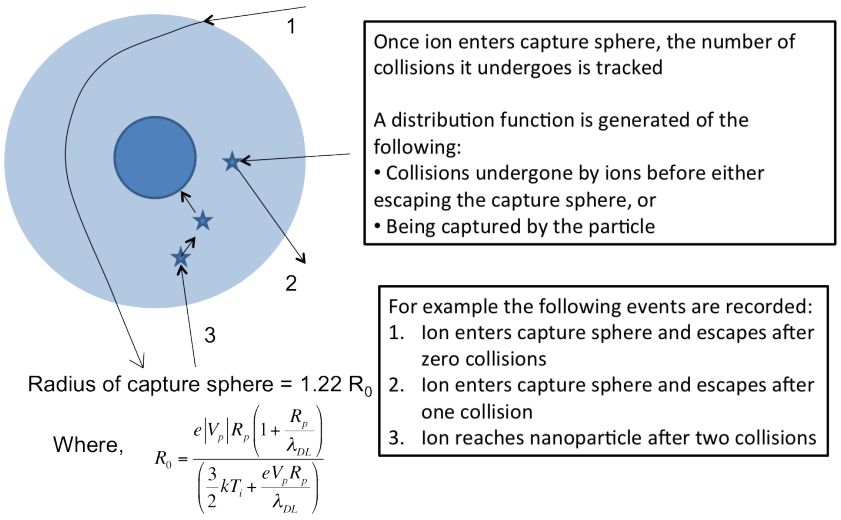

Figure 5.2: Figure describing collision tracking in PIC MC simulations.

5.2.2 Ion-neutral Collisions

The ion-neutral interactions in the discharge are determined by the collision cross sections. Two types of collisions are considered between argon ions and argon gas atoms: resonant charge transfer and elastic scattering. Both types of collision are equally likely to occur, and are described using the same cross-section [60]. The elastic scattering was considered to be isotropic. Energy and momentum of the center of mass were conserved. in the event of a charge exchange collision, the ion acquired the pre-collision kinetic energy and momentum of the neutral gas atom. Among the hydrogen ions, only the triatomic hydrogen was considered. The neutral gas consisted only of argon. Since the most dominant type of interaction between H_3^+ and argon is elastic scattering [39] at low energies, it was the only type of collision that was considered. The cross-sections for $Ar - Ar^+$ collisions and $Ar - H_3^+$ collisions are seen in Figure 5.3

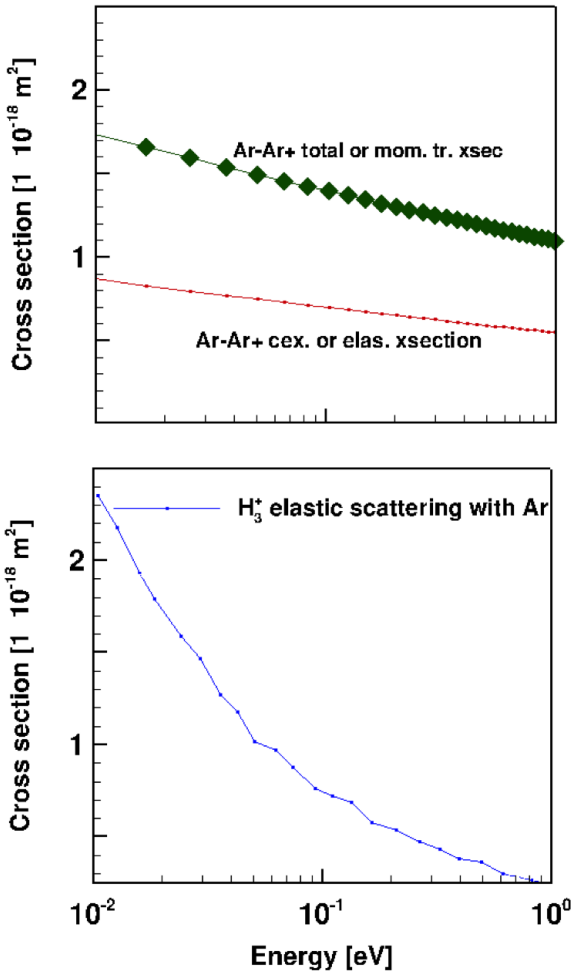

Figure 5.3: Cross sections for ion natural collisions between argon and Ar^+ ions and argon and H_3^+ ions.

From the PIC-MC simulations the steady state charge of the nanoparticle was calculated. The energy distribution of ions impacting the particle were recorded. The role of charge-exchange and elastic scattering to particle charging was studied.

5.3 Results and discussion

5.3.1 PIC-MC simulations: Pure argon discharge

Consider the case of a pure argon discharge where the Ar^+ ion density at 10^{16} m^{-3}. The electrons are at a mean temperature of 3.4 eV. The steady state floating potential acquired by a 500 nm particle over a wide range of pressures is shown in Figure 5.4. The corresponding variation of ion flux to the particle is shown in Figure 5.5. It is seen that as the pressure is increased, the magnitude of floating potential reduces and reaches a minimum; subsequently it increases again.

Corresponding to these plots, the distribution of ion energies impinging on the particle (ion energy distributions or IEDF) are plotted in Figure 5.6. There are two 'components' of the IEDF on the plots, which correspond to ion energy due to the radial velocity component and the tangential velocity component respectively. At all pressures, the IEDF is limited by the particle potential (marked by a dashed line). At 1 Pascal, when the mean free path of ions is >> than the Debye length, the ions reach the nanoparticle surface at an energy corresponding to the particle potential. As the pressure increases, the considerable fraction of low energy ions impact the particle. The tangential component begins to reduce and the radial component increases. The IEDF plot clearly suggest that ion collisions are responsible for the particle potential drop. Trapped ions undergo a collision that leads to their energy loss. The subsequently fall towards the particle along the electric field lines. As the collisions continue to increase with pressure, the current begins to be inhibited by them. This results in a higher

particle potential an a high standard deviation of the IEDFs.

However, two different types of collisions were considered in the above simulations: the charge exchange, and the elastic scattering. A charge exchange collision in the vicinity of the particle leads to the creation of a low energy ion. On the other hand, elastic scattering collision changes causes loss of angular momentum of the ion. So it is not clear how these collisions individually contribute to particle charging.

Two understand the individual effect of each type of collision, three sets of simulations were performed. (1) Only the $Ar - Ar^+$ charge exchange collisions were effective in the discharge, (2) Only the $Ar - Ar+$ elastic scattering collisions were active, and (3) both were active. Of the ions that impacted the nanoparticle, histograms of collisions inside the capture sphere in each case were plotted in Figure 5.7 at three different pressures. The ion flux is normalized. Note that the collision cross sections of charge exchange collision (henceforth cex.) and elastic collisions (henceforth elas.) are approximately equal ($80 \times 10^{-20}\ m^{-2}$). At 10 Pascal, the cex. have begun to contribute to charging but elas. have not. At 100 Pa there is a peak of the collision histogram for the cex. case. This shows the ion trapping effect inside the capture sphere. An ion inside the sphere has higher kinetic energy because of the influence of electric field. When it undergoes a charge exchange collision, a low energy ion is created which is trapped in the potential inside the sphere. It is eventually captured by the ion. Such a peak is absent in the case of elas. The highest fraction of ions impacting the particle are still the ones that underwent zero elastic collisions. This shows that current enhancement due to elastic scattering is not because of energy loss, but because of the loss of angular momentum. In the third column, the histograms represent either type of collision. Even though the collision frequency has doubled (due to both type of collisions activated), the collision histogram is not a 'sum' of the first two histograms. Figure 5.8 plots the energy distribution of ions impacting the nanoparticle for the fist two sets of simulations

discussed above. At low pressure the ions reach the nanoparticle mono energetically. The radial and tangential 'components' of the energy are widely distributed. However, in the case of cex. only, the radial component becomes higher and the tangential, lower with increased pressure. This indicates that the charge exchange collisions are producing low energy ions that travel along the filed lines and impact the nanoparticle. For the elas. only case, however, the radial and tangential components continue to be broadly distributed even at higher pressures.

Figure 5.9, the steady state particle potential is compared for the there sets of simulations. Charge exchange collisions are seen to have a greater contribution to particle charge. However, at 10,000 Pa, in highly collisional plasma, both contribute similarly to charging.Table 5.1 shows argon ion current (that is normalized to the current when both types of collisions are active) for the three sets of simulations at different pressures. Note that the ion current does not double due to the presence of both types collision, although the collision cross section doubles. Form the above discussion, it can be concluded that in pure argon discharge, charge exchange collisions have the most impact on particle charging.

Table 5.1: Normalized ion current to particle in pure argon discharge

Type of collisions present	10 Pa	100 Pa	316 Pa
Only charge exchange	0.87	0.88	0.96
Only elastic scattering	0.66	0.76	0.79
Both are present	1	1	1

5.3.2 PIC-MC simulations: Argon hydrogen discharge

To mimic a typical low pressure discharge in argon hydrogen mixture, equal fractions of argon and triatomic hydrogen ions (H_3^+) were considered to be present in argon gas. This mimics a situation where trace quantity of hydrogen mixed with argon has

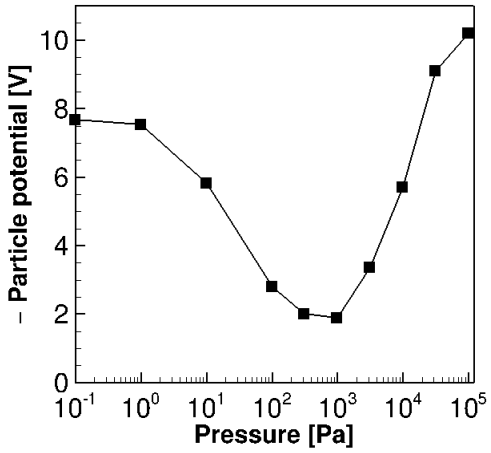

Figure 5.4: Floating potential versus pressure for a $R_p = 500nm$ particle, for a discharge containing $n_{Ar^+} = 1 \times 10^{16}\ m^{-3}$, $T_e = 3.4$ eV.

.

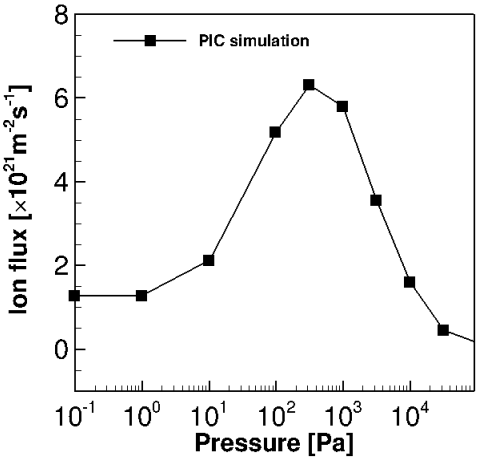

Figure 5.5: Steady state ion flux versus pressure for a $R_p = 500nm$ particle, for a discharge containing $n_{Ar^+} = 1 \times 10^{16}\ m^{-3}$, $T_e = 3.4$ eV.

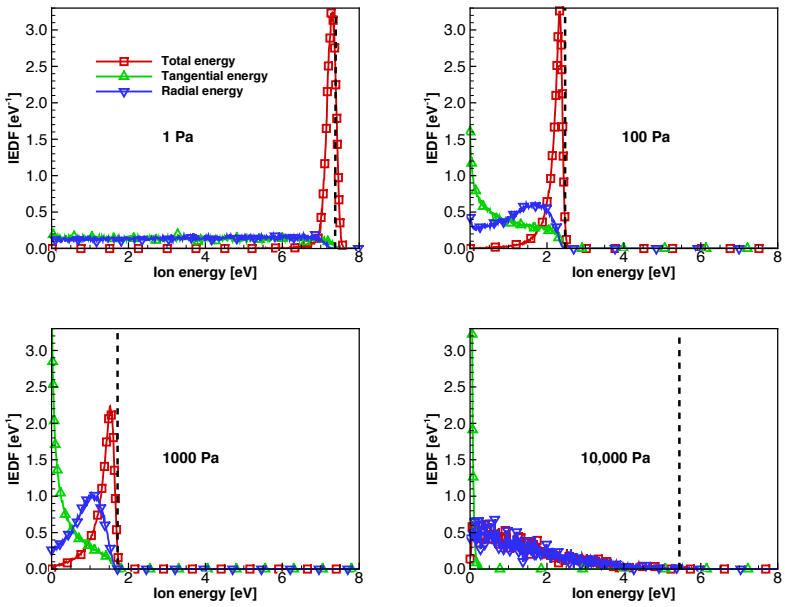

Figure 5.6: Ion energy distributions, and distributions of energy associated with radial and tangential ion velocity components for $500nm$ particle a pure argon discharge, $n_{Ar^+} = 1 \times 10^{16}\ m^{-3}$, $T_e = 3.4$ eV.

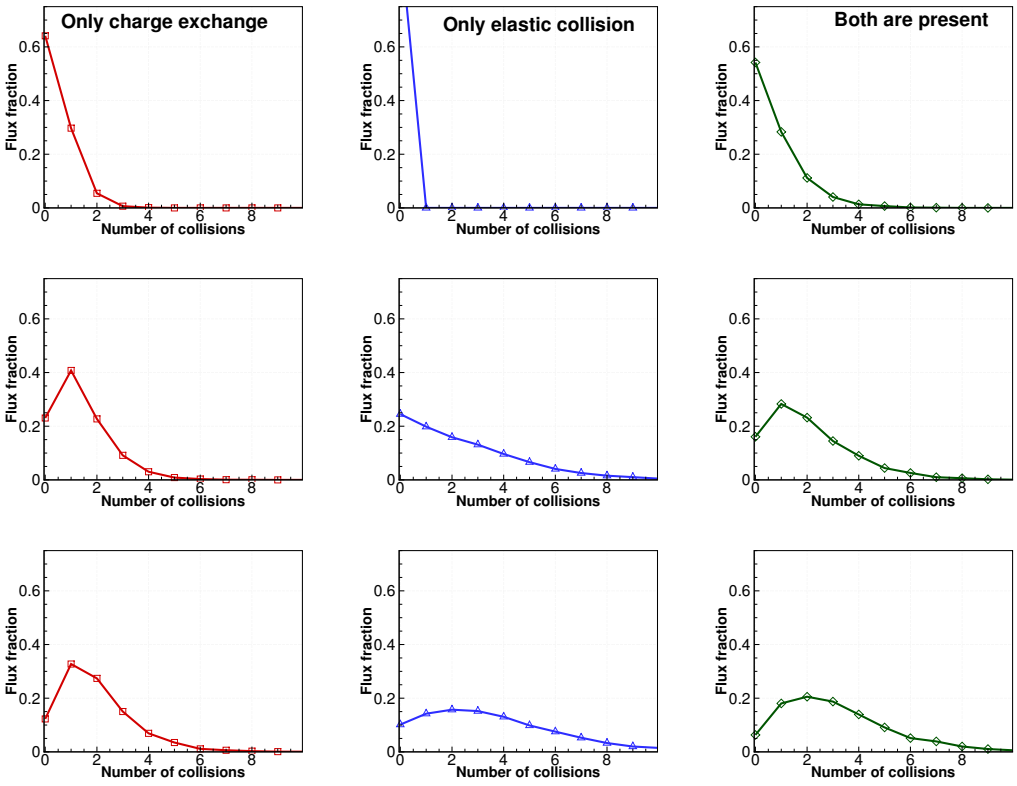

Figure 5.7: Histogram of collisions in the capture sphere undergone by ions constituting flux to the nanoparticle surface when only the charge exchange collision are present (column 1), only elastic scattering is present (column 2) and both are present. $500nm$ particle for the discharge containing $n_{Ar^+} = 1 \times 10^{16}\ m^{-3}$, $T_e = 3.4$ eV.

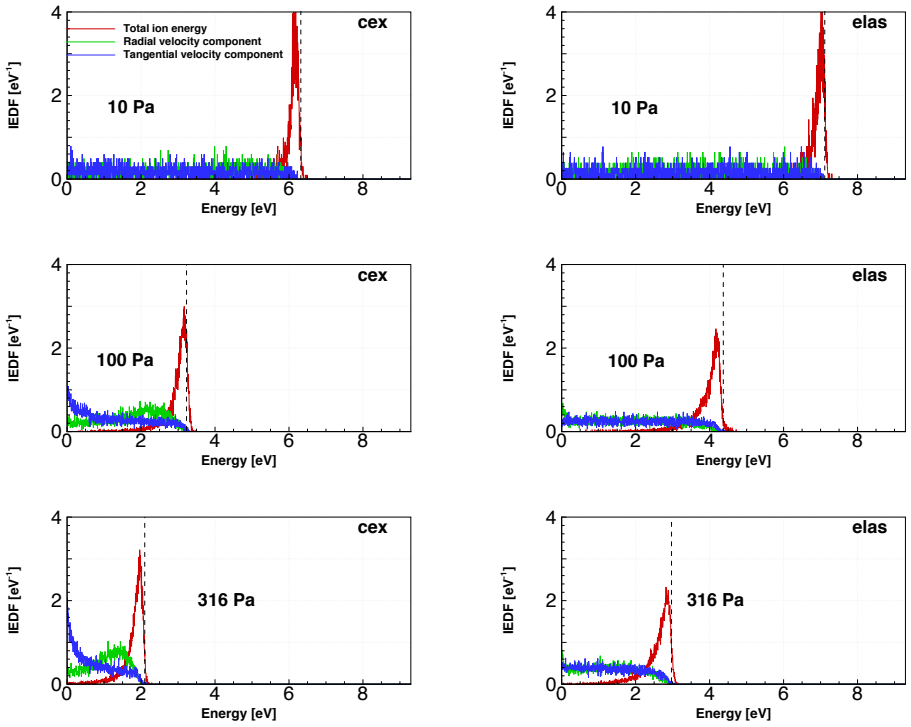

Figure 5.8: Ion energy distribution in pure argon discharge when only the charge exchange collisions are considered (left column) and only when elastic scattering is considered (right column).

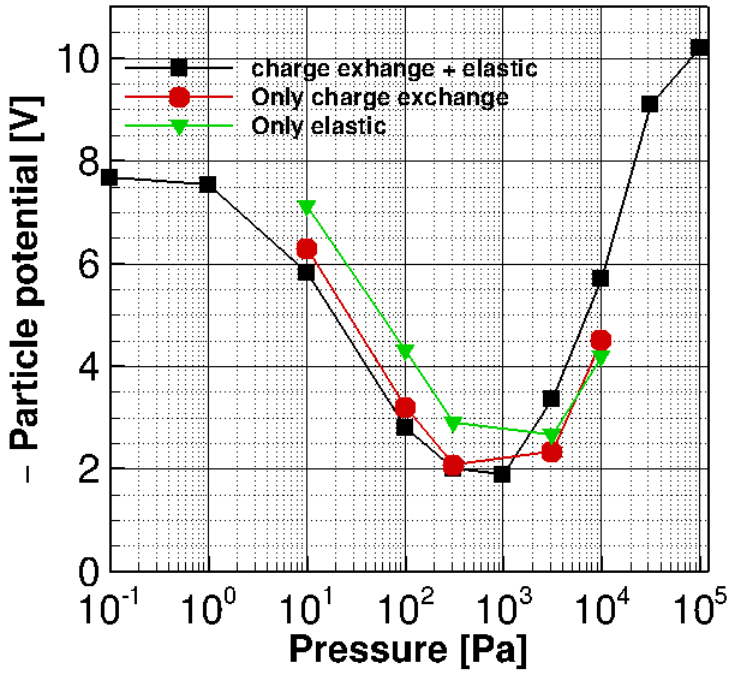

Figure 5.9: Floating potential versus pressure for a $R_p = 500nm$ particle, for a discharge containing $n_{Ar^+} = 1 \times 10^{16}\ m^{-3}$, $T_e = 3.4$ eV.

produced a considerable fraction of hydrogen ions. The main aim of this section is to study how the presence of two different types of ions in the plasma effects steady state nanoparticle charging. Figure 5.10 depicts the steady state floating potential of a $500nm$ particle in a discharge containing $n_{Ar^+} = 5\times10^{15}\ m^{-3}$, and $n_{H_3^+} = 5\times10^{15}\ m^{-3}$. Figure 5.11 compares the potential with that in pure argon discharge. However, Figure 5.12 reveals that the Ar^+ and H_3^+ currents peak at different pressures. The total collision cross section of Ar^+ with argon gas is $160\times10^{-20}\ m^2$, that of H_3^+ ions with argon gas is $80\times10^{-20}\ m^2$. The hydrogen ions are, however lighter. In 'collisionless' regime at below Pascal, the hydrogen ion current is higher because of their higher thermal velocity. At intermediate pressures, argon ion flux peaks first, followed by hydrogen flux. Hydrogen flux enhancement is completely because of elastic scattering.

Figure 5.13 plots the IEDF for individual ion fluxes to the particle at different pressures. Argon IEDF broadens with increasing pressure, indicating energy loss due to charge exchange collisions. Hydrogen IEDF is slower to broaden. The collision histograms in Figure 5.14 also indicate the ion trapping phenomenon of argon, showing a peak at 1 collision, at 100 Pascal. A single collision between H_3^+ and Ar on the other hand seems to prevent ion collection by particle; multiple elastic scattering events lead to current enhancement.

5.3.3 Analytical model

An analytical model was developed by Gatti and coworkers [60] to calculate the particle potential in pure argon discharge. In this chapter, the analytical model is modified and extended to accommodate the presence of two different species of ions in the plasma. The basis of this model is that ion-neutral collisions in the vicinity of the nanoparticle aid ion capture. It remains to define this distance around the nanoparticle. Also a relationship needs to be established between an ion-neutral collision and a probability

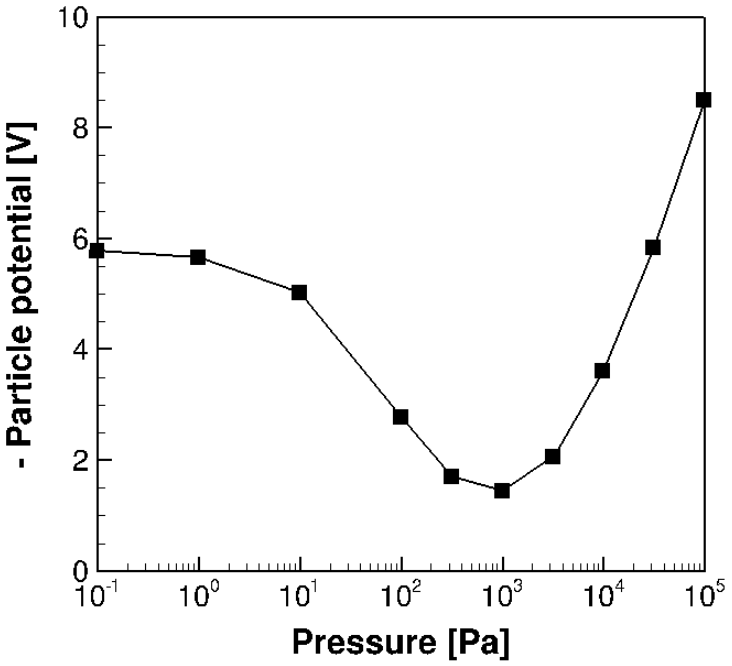

Figure 5.10: Steady state floating potential for a $500nm$ particle. $n_{Ar^+} = 5 \times 10^{15}\ m^{-3}$, and $n_{H_3^+} = 5 \times 10^{15}\ m^{-3}$, $T_e = 3.4$ eV.

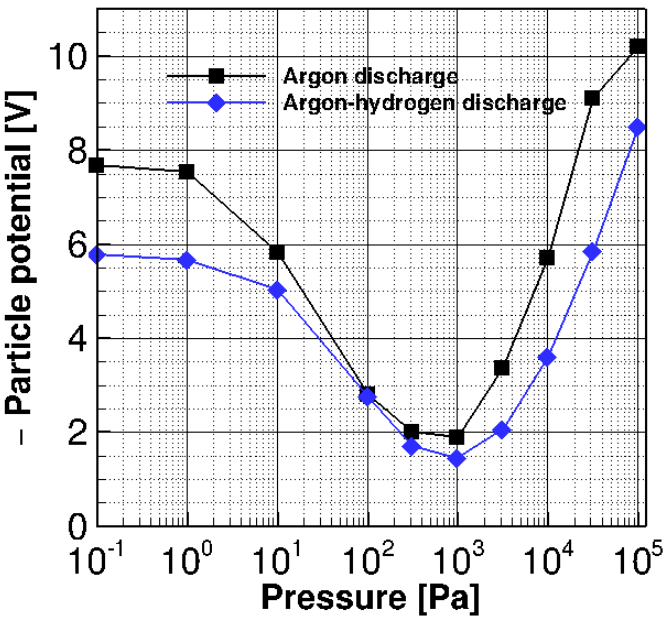

Figure 5.11: Steady state floating potential comparison for pure Ar discharge in Figure 5.4 , and $Ar - H_2$ discharge. $R_p = 500nm$ particle. $n_{Ar^+} = 5 \times 10^{15}\ m^{-3}$, and $n_{H_3^+} = 5 \times 10^{15}\ m^{-3}$, $T_e = 3.4$ eV.

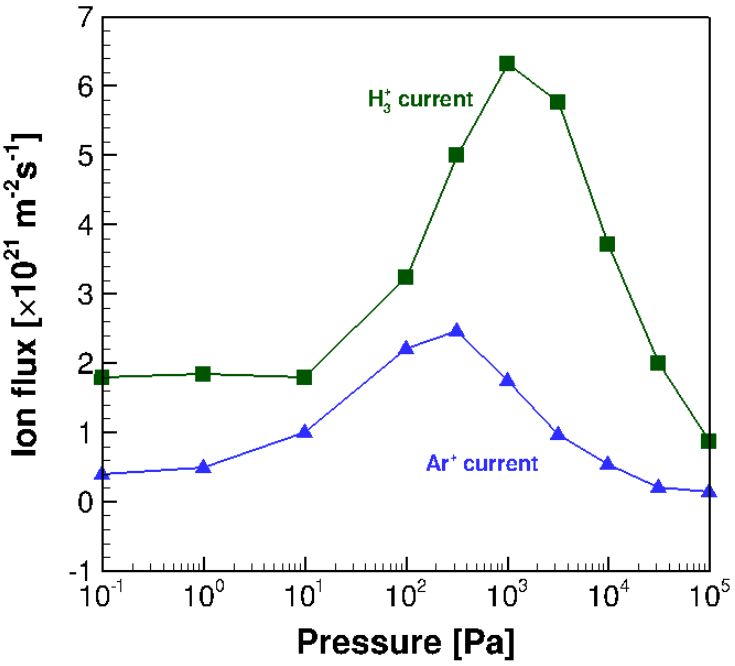

Figure 5.12: Steady state ion flux for a , $R_p = 500nm$ particle. $n_{Ar^+} = 5 \times 10^{15}\ m^{-3}$, and $n_{H_3^+} = 5 \times 10^{15}\ m^{-3}$, $T_e = 3.4$ eV.

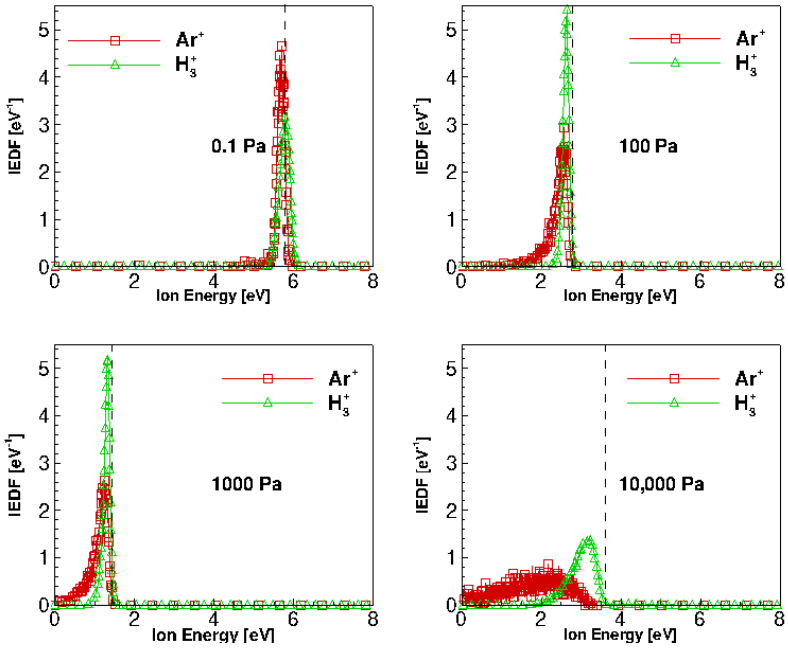

Figure 5.13: Ion energy distributions for each type of ion for a $500nm$ particle, $n_{Ar^+} = 5 \times 10^{15}\ m^{-3}$, $n_{H_3^+} = 5 \times 10^{15}\ m^{-3}$,$T_e = 3.4$ eV.

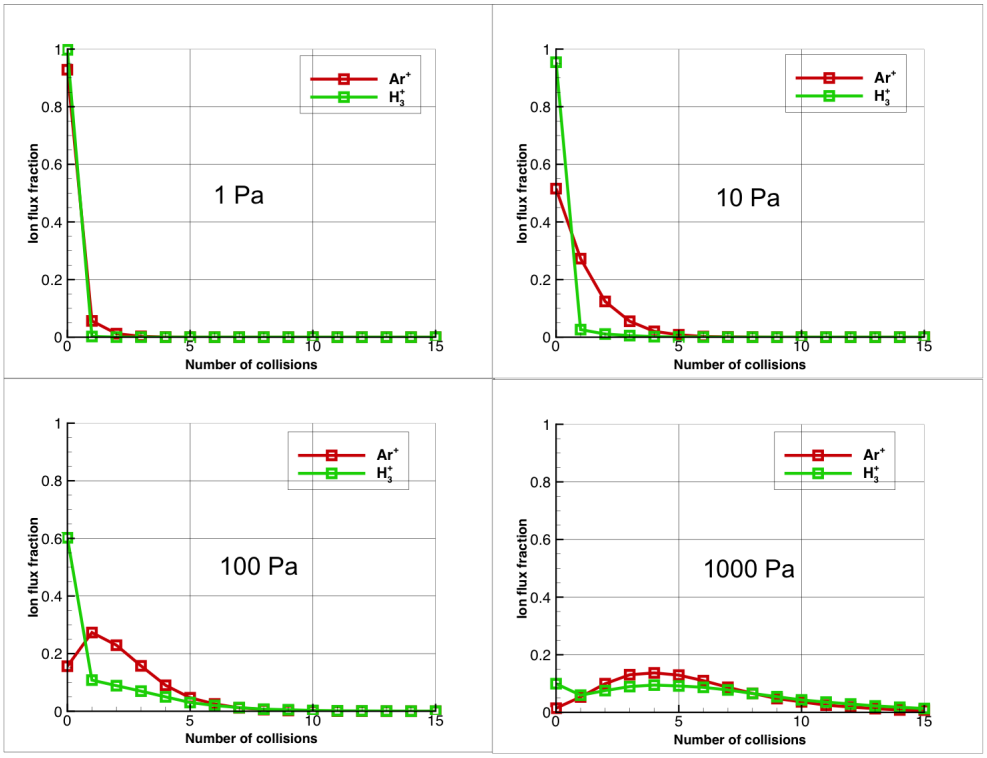

Figure 5.14: Histogram of collisions undergone by ions forming the current, inside the capture sphere for a $500nm$ particle. $n_{Ar^+} = 5 \times 10^{15}\ m^{-3}$, and $n_{H_3^+} = 5 \times 10^{15}\ m^{-3}$, $T_e = 3.4$ eV.

that it will lead to the ion impacting the nanoparticle.

Clearly, the region around the nanoparticle where collisions are important, needs to have a non negligible electric field. For a 500 nm particle in plasma with low degree of ionization, the Debye-Huckel potential describes the variation of potential with distance from the particle. We define a 'capture sphere' around the particle such that its radius is given by the distance from the nanoparticle at which the potential energy of a newly created ion is equal to the kinetic energy of the background gas. Let us define a 'trapping event' inside the capture sphere such that, if a trapping event occurs, then the ion cannot escape the capture sphere and eventually impacts the nanoparticle. For hydrogen ions in argon gas, elastic scattering is the most dominant type of interaction between the H_3^+ and Ar. In this case a trapping event would consist of the number of collisions needed for a hydrogen ion to lose enough kinetic energy such that it cannot escape the field anymore. Trapping is therefore associated with energy relaxation of the ion. Let $E_{v,0}$ be the initial kinetic energy of an ion inside the capture sphere, E_v^* be the kinetic energy of neutral gas atoms, and E_v be the kinetic energy of the ion after one collision. Fraction of energy lost after one collision is given by Equation 5.1 [62]. Here t_c is the time between two successive collisions and τ is the energy relaxation time.

$$\frac{E_v - E_v^*}{E_{v,0} - E_v^*} = \exp\left(\frac{-t_c}{\tau}\right) \tag{5.1}$$

Average kinetic energy loss of a single particle of mass m_1 traveling in a gas composed of particles of mass m_2 and average kinetic energy E_v^* is given by Equation 5.2 [63].Let the ratio be denoted by β.

$$\frac{E_v - E_{v,0}}{E_{v,0} - E_v^*} = -\frac{2m_1m_2}{(m_1 + m_2)^2} = -\beta \tag{5.2}$$

Combining Equations 5.1 and 5.2 gives us an expression for the energy relaxation time (Equation 5.3).

$$\tau = \frac{-t_c}{\ln(1-\beta)} \tag{5.3}$$

Root Mean Square (RMS) displacement during relaxation time τ is given by Equation 5.4 where D is the diffusivity of the particle in the gas [64].

$$\lambda_{rms} = \sqrt{2D\tau} \tag{5.4}$$

For an H_3^+ ions in argon gas whose masses are 3 and 40 a.m.u respectively, the ratio of RMS displacement to mean free path λ_{mfp} is equal to 2.33. The probability of zero, one or greater-than-one trapping events occurring in the capture sphere can therefore be calculated by replacing the mean free path with RMS displacement in the equations given by Gatti et al, as shown in equation 5.5. Here $K = 1.22$ is a numerical constant obtained by averaging the capture radius over Maxwellian distribution of the ions.

$$\begin{cases} P_{i,c=0} = exp\left(-\frac{KR_0}{\lambda_{rms}}\right) \\ P_{i,c=1} = \left(\frac{KR_0}{\lambda_{rms}}\right) exp\left(-\frac{KR_0}{\lambda_{rms}}\right) \\ P_{i,c>1} = 1 - P_{i,c=0} - P_{i,c=1} \end{cases} \tag{5.5}$$

While calculating the trapping probability for argon ions, we cannot however use the same formulation. Argon ions undergo both charge exchange and elastic scattering with equal likelihood. However these interactions result in different type of energy exchange between colliding particles. From the PIC-MC it is seen that the particle current increases only slightly when both the collisions are considered, compared to the cases when only either one of them is considered. The effect of charge exchange and elastic collisions occurring simultaneously is not a sum of the effects of each type of collision. From the normalized current calculations using PIC-MC, it is seen that the mean free path associated with argon ion trapping is approximately twice the mean free path of collision.

When the probability of trapping is zero, ion current to the particle is described by the OML current. At high pressures, the current is described by mobility limited

hydrodynamic ion flux. In intermediate pressures, there is a transition between the collisionless current and the highly collisional one. In order to describe the ion current over a wide range of pressures, the OML and the hydrodynamic currents can be weighted by zero probability of a trapping event and probability that more than one trapping event will occur in the capture sphere, respectively. A third component of this unifying expression consists of thermal current to capture sphere weighted by the probability that exactly one trapping event will occur inside the same. The current components are given by the expressions below.

$$I_{i,OML} = e\frac{1}{4}n_i\left(4\pi R_p^2\right)\sqrt{\frac{8k_BT_i}{\pi m_i}}\left(1-\frac{eV_p}{k_BT_i}\right) \tag{5.6}$$

$$I_{i,CEC} = e\frac{1}{4}n_i\left(4\pi R_0^2\right)\sqrt{\frac{8k_BT_i}{\pi m_i}} \tag{5.7}$$

$$I_{i,HYD} = e4\pi R_p n_i \mu_i \left|V_p\right| \tag{5.8}$$

The unifying expression of ion current is given by Equation 5.9.

$$I_i = \left(P_{i,c=0}I_{i,OML} + P_{i,c=1}I_{i,CEC} + P_{i,c>1}I_{i,HYD}\right) \tag{5.9}$$

Electrons are assumed to be in Maxwellian distribution. Their mean free path of collision with gas atoms remains larger than the characteristic length scales over a wide range of pressures. The OML expression for repulsive potential is used to describe the electron current to the nanoparticle.

$$I_e = e\frac{1}{4}\left(4\pi R_p^2\right)n_e\sqrt{\frac{8k_BT_e}{\pi m_e}}exp\left(\frac{eV_p}{k_BT_e}\right) \tag{5.10}$$

The steady state charge on the nanoparticle Z_k is calculated using Equation 5.11 and the corresponding particle potential is given by Equation 5.12.

$$\frac{dZ_k}{dt} = I_e - I_i \tag{5.11}$$

$$V_p = \frac{Z_k}{4\pi\epsilon_0 R_p} \tag{5.12}$$

Figures 5.15 and 5.16 display a good agreement between the floating particle potential and ion flux obtained via PIC-MC simulations and the analytical model for pure argon discharge. The nanoparticle size was $500nm$, electron temperature was 3.4 eV and Ar^+ ion density was $1 \times 10^{16} m^{-3}$.

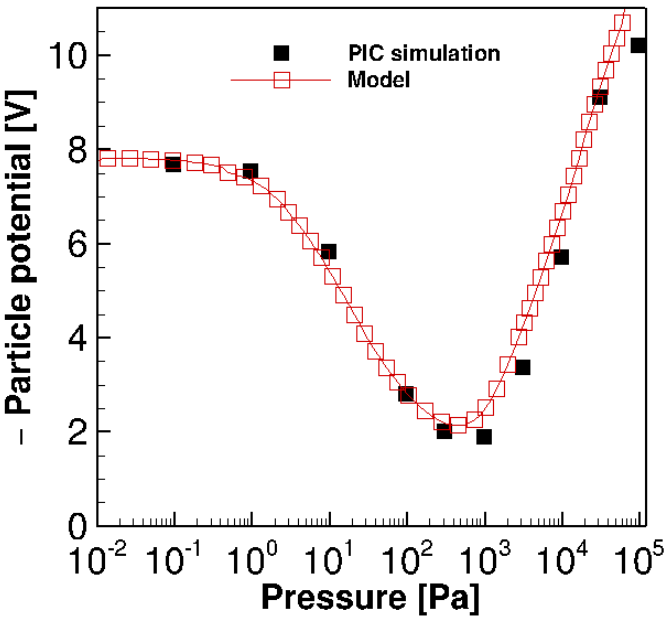

Figure 5.15: Comparison of particle potential obtained through PIC-MC simulations and analytical model for $500nm$ particle. $n_{Ar^+} = 1 \times 10^{16}\ m^{-3}$, $T_e = 3.4$ eV.

It was seen that Gatti's analytical model could be extended to accommodate multiple types of ions. In the extended model, the ion current is given by the summation currents

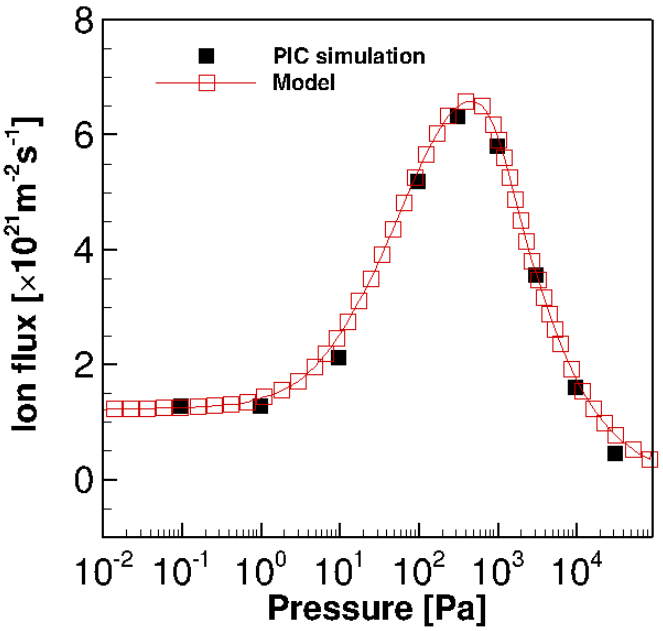

Figure 5.16: Comparison of steady state ion flux obtained through PIC-MC simulations and analytical model for $500nm$ particle. $n_{Ar^+} = 1 \times 10^{16}\ m^{-3}$, $T_e = 3.4$ eV.

of each individual species of ions, as follows.

$$\sum_{i=1}^{n} I_i = \sum_{i=1}^{n} (P_{i,c=0} I_{i,OML} + P_{i,c=1} I_{i,CEC} + P_{i,c>1} I_{i,HYD}) \tag{5.13}$$

$$\frac{dZ_k}{dt} = I_e - \sum_{i=1}^{n} I_i \tag{5.14}$$

Figures 5.17 and 5.18 show a comparison of the particle potential and fluxes of individual ion species for the argon hydrogen discharge, obtained from PIC-MC and from the analytical model.

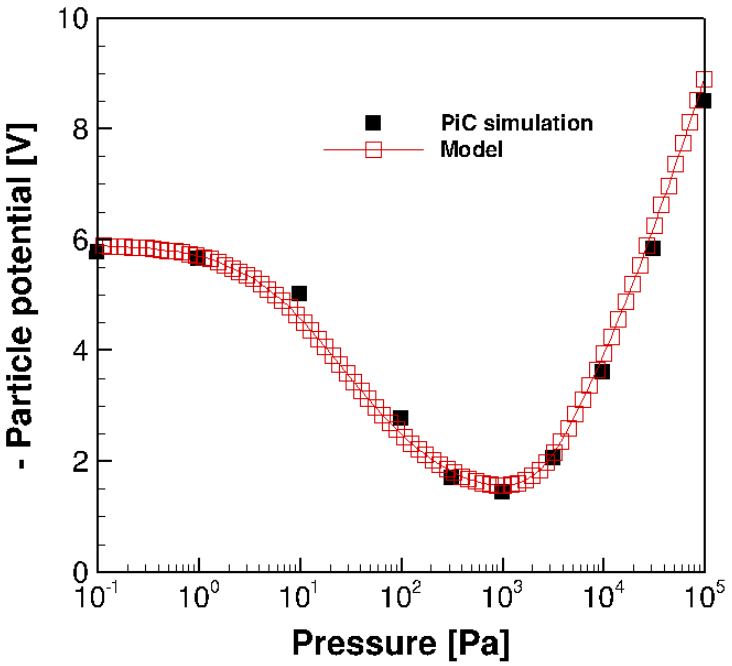

Figure 5.17: Comparison of particle potential obtained through PIC-MC simulations and analytical model for $500nm$ particle. $n_{Ar^+} = 5 \times 10^{15}\ m^{-3}$, and $n_{H_3^+} = 5 \times 10^{15}\ m^{-3}$,$T_e = 3.4$ eV.

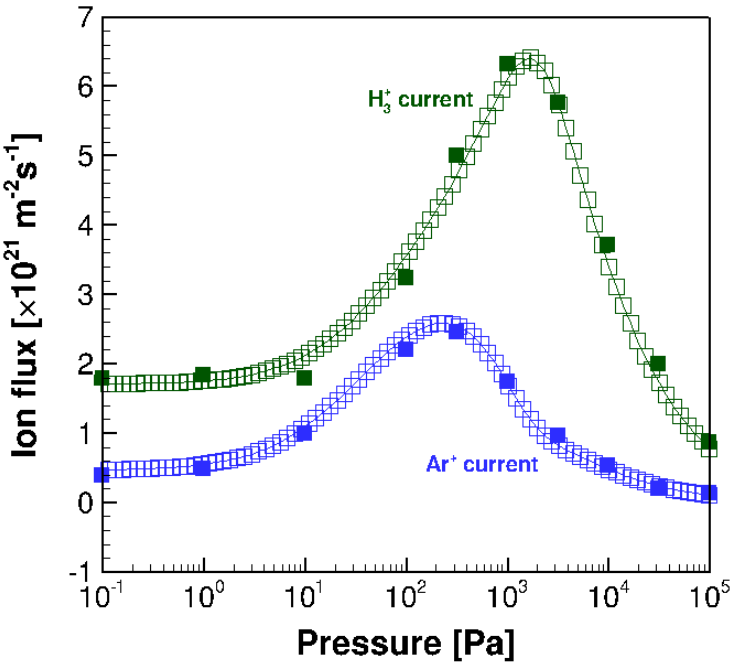

Figure 5.18: Comparison of steady state ion flux obtained through PIC-MC simulations and analytical model for $500nm$ particle. $n_{Ar^+} = 1\times10^{16}\ m^{-3}$, and $n_{H_3^+} = 5\times10^{15}\ m^{-3}$, $T_e = 3.4$ eV.

5.4 Conclusion and scope

In this chapter it was shown that hydrogen ions need to be considered while studying nanoparticle plasma interaction in $Ar : SiH_4$, and $Ar : H_2 : SiH_4$ discharges. Particle charging and constitution of ion current to the particle surface depend on the collisionality of the individual ion species within the discharge. Therefore the discharge pressure determines the fraction of each species of ions impacting the nanoparticle.

It was seen that at a given pressure, while the particle floating potential limits the maximum energy of ion impaction ,the standard deviation of ion energy distribution is influenced by the ion collisionality in the discharge. As a result, the IEDFs of individual species may vary. Argon ions have a wider distribution of ion impact energy compared to H_3^+ ions.

Heavy and light ions impact nanoparticles with different outcomes. A heavy ion like Ar^+ impacting the particle transfers its kinetic energy efficiently to the particle. Whereas, when a light ion like H_3^+, only a small fraction of the ion kinetic energy is transferred, due to the difference of masses between the particle and ion. The rest of the energy is consumed in scattering the ion, or dissociating it into atomic H radicals, or creating dangling bonds [58]. Heavy Ar^+ ion impaction can be hypothesized to disrupt the arrangement of Si atoms in the particle, thereby promoting rearrangement into a low energy lattice structure. Impaction of hydrogen ions, on the other hand, can be inferred to be useful for the delivery of H radicals to the particle surface, that work in multiple ways to promote crystallization [14, 65].

It can be said that pressure and gas composition can be used as parameters to control the constitution and IEDF of the ions impacting the nanoparticles in $Ar : H_2$ discharges, to enhance desirable properties of the resulting nanocrystals.

Chapter 6

Conclusion and Discussion

In summary, simulation of DBD plasma actuators showed the spatial characteristics of force generated by anode, and cathode directed discharges on the actuator. A cathode directed discharge produced a higher body force. This asymmetry was due the difference in charge accumulation characteristics of the dielectric when it is an anode and a cathode. The simulations support the hypothesis that charge drainage from the surface would enhance the thrust produced by the actuator, as was seen by experimental work.

A self consistent volume averaged simulation was developed to study discharge characteristics of a CCP RF argon hydrogen plasma in the presence of nano sized particles. This is a useful tool to estimate the plasma composition, power dissipation path ways, and electron energy distributions by fixing the operating parameters of the discharge, and the nanoparticle size and density. The simulation established the importance of considering hydrogen chemistry even if it is present in trace quantities in argon discharge.

An analytical model for particle charging in plasma in the presence of more than one species of ions which have different masses, and ion-neutral interaction characteristics was developed. Contribution of charge exchange and elastic scattering collisions to

particle charging was studied. Particle charging in pure argon discharge was compared to charging in a discharge containing argon and H_3^+ ions. It was shown that hydrogen ions tended to reduce the floating potential of nano sized particles, and the ion current was made up of hydrogen as well as argon ions. Via the potential, and current, hydrogen ion presence in argon dusty plasma influenced the energy distributions ions impacting the nanoparticle surface. It was shown via simulations that it is possible to control the constitution and energy distribution of ion impacting a nanoparticle surface by controlling the pressure and gas composition of the discharge. This capability would offer an additional means to control the surface processes occurring on the nanoparticle.

References

[1] M. L. Post, T. C. Corke, S. Wilkinson, D. Ashpis, D. Miller, and L. Ukeiley. Separation control on high angle of attack airfoil using plasma actuators. *AIAA Journal*, 42(11):2177–2184, 2004.

[2] M. G. McHarg C. L. Enloe and T. E. McLaughlin. Time-correlated force production measurements of the dielectric barrier discharge plasma aerodynamic actuator. *Journal of Applied Physics*, 103(7):073302–073302–7, 2008.

[3] M. A. Lieberman and A. J. Lichtenberg. Principles of plasma discharges and materials processing. *MRS Bull*, 30:899, 2005.

[4] J. A. Bittencourt. *Fundamentals of plasma physics*. Springer, 2004.

[5] Y. P. Raizer. *Gas discharge physics*. 1991.

[6] U. Kogelschatz. Dielectric-barrier discharges: their history, discharge physics, and industrial applications. *Plasma Chemistry and Plasma Processing*, 23(1):1, 2003.

[7] Akira Mizuno. Industrial applications of atmospheric non-thermal plasma in environmental remediation. *Plasma Physics and Controlled Fusion*, 49(5):A1, 2007.

[8] M. Laroussi. Low temperature plasma-based sterilization: Overview and state-of-the-art. *Plasma processes and polymers*, 2(5):391, 2005.

[9] J. Perrin. Possible routes for cluster growth and particle formation in rf silane discharges. *Plasma sources science technology*, 3(3):252, 1999.

[10] R. L. Merlino and J. A. Goree. Dusty plasmas in the laboratory, industry, and space. *Physics Today*, 57:32, 2004.

[11] U. Kortshagen, L. Mangolini, and A. Bapat. Plasma synthesis of semiconductor nanocrystals for nanoelectronics and luminescence applications. *Journal of Nanoparticle Research*, 9(1):39–52, 2007.

[12] R. J. Anthony. Routes to achieving high quantum yield luminescence from gas-phaseproduced silicon nanocrystals. *Advanced functional materials*, 21(21):4042, 2011.

[13] D. Das M. Jana and AK Barua. Role of hydrogen in controlling the growth of c-si: H films from argon diluted sih 4 plasma. *Journal of Applied Physics*, 91(8):5442–5448, 2002.

[14] S. Sriraman, M. S. Valipa, E. S. Aydil, and D. Maroudas. Hydrogen-induced crystallization of amorphous silicon thin films. i. simulation and analysis of film postgrowth treatment with hydrogen plasmas. *Journal of Applied Physics*, 100(5):053514–053514–11, 2006.

[15] E. Neyts. Particle-in-cell/monte carlo simulations of a low-pressure capacitively coupled radio-frequency discharge: Effect of adding h to an ar discharge. *Journal of Applied Physics*, 93(9):5025, 2003.

[16] T. C. Corke J. Huang and F. O. Thomas. Plasma actuators for separation control of low-pressure turbine blades. *American Institute of Aeronautics and Astronautics Journal*, 44(1):51, January 2006 2006.

[17] R. Van Dyken, H. Perez-Blanco, A. Byerley, and T. McLaughlin. Plasma actuator for wake flow control of high camber blades during part load operation. ASME, 2004.

[18] M. L. Post and T. C. Corke. Separation control using plasmas actuators- stationary and oscillating airfoils. In *42 nd AIAA Aerospace Sciences Meeting and Exhibit*, 2004.

[19] M. L. Post and T. M. Corke. Separation control on high angle of attack airfoil using plasma actuators. *American Institute of Aeronautics and Astronautics Journal*, 42(11):2177, November 2004 2004.

[20] C. L. Enloe. Mechanisms and responses of a single dielectric barrier plasma actuator: plasma morphology. *AIAA Journal*, 42(3):589, 2004.

[21] R. D. VanDyken C. L. Enloe, T. E. McLaughlin and J. C. Fischer. Plasma structure in the aerodynamic plasma actuator. *AIAA paper*, 844, 2004.

[22] T. E. McLaughlin C. L. Enloe C. O. Porter, J. W. Baughn and G. I. Font. Plasma actuator force measurements. *AIAA Journal*, 45(7):1562–1570, 2007.

[23] T. E. McLaughlin C. L. Enloe C. O. Porter, J. W. Baughn and G. I. Font. Temporal force measurements on an aerodynamic plasma actuator. In *44 th AIAA Aerospace Sciences Meeting and Exhibit*, pages 1–15, 2006.

[24] Y. Lagmich, Th Callegari, Th Unfer, L. C. Pitchford, and J. P. Boeuf. Electrohydrodynamic force and scaling laws in surface dielectric barrier discharges. *Applied Physics Letters*, 90(5), 1 Febuary 2007 2007.

[25] T. E. McLaughlin R. Van Dyken and C. L. Enloe. Parametric investigations of a single dielectric barrier plasma actuator. In *Proc. 42nd Aerospace Sciences Meeting and Exhibit (Reno, NV), Paper AIAA 2004*, volume 846, 2004.

[26] T. E. McLaughlin C. H. Enloe and G. I. Font. Parameterization of temporal structure in the single dielectric barrier aerodynamic plasma actuator. volume 43, 10-13 January 2005.

[27] G. Neretti D. F. Opaits, A. V. Likhanskii and S. Zaidi. Experimental investigation of dielectric barrier discharge plasma actuators driven by repetitive high-voltage nanosecond pulses with dc or low frequency sinusoidal bias. *Journal of applied physics*, 104(4):104, 27 August 2008 2008.

[28] D. M. Orlov and T. M. Corke. Numerical simulation of aerodynamic plasma actuator effects. volume 43, 10-13 January 2005 2005.

[29] Th Unfer, Y. Lagmich, F. Rogier, F. Thivet, and J. P. Boeuf. Dbd for aerodynamic flow control: numerical investigation and coupling with computational fluid dynamics. volume 28, 15-20 July 2007.

[30] J P Boeuf. Electrohydrodynamic force in dielectric barrier discharge plasma actuators. *Journal of Physics D: Applied Physics*, 40(3):652, 2007.

[31] J. P. Boeuf, Y. Lagmich, Th Callegari, L. C. Pitchford, and Th Unfer. New insights in the physics of dbd plasma actuators for flow control. volume 46, 7-10 January 2008.

[32] J. P. Boeuf, Y. Lagmich, and L. C. Pitchford. Contribution of positive and negative ions to the electrohydrodynamic force in a dielectric barrier discharge plasma actuator operating in air. *Journal of applied physics*, 106, 29 July 2009 2009.

[33] A. V. Likhanskii, M. N. Shneider, S. O. Macheret, and R. B. Miles. Modeling of dielectric barrier discharge plasma actuators driven by repetitive nanosecond pulses. *Physics of Plasmas*, 14(7):14, 9 July 2007 2007.

[34] W. S. Kang and Woo Seok Kang. Numerical study on influences of barrier arrangements on dielectric barrier discharge characteristics. *IEEE Transactions on Plasma Science*, 31(4):504, 2003.

[35] A. Bourdon, V. P. Pasko, N. Y. Liu, S. Celestin, P. Segur, and E. Marode. Efficient models for photoionization produced by non-thermal gas discharges in air based on radiative transfer and the helmholtz equations. *Plasma Sources Science and Technology*, 16(3):656, 2007.

[36] A. V. Likhanskii, V. V. Semak, M. N. Shneider, D. F. Opaits, R. B. Miles, and S. O. Macheret. The role of the photoionization in the numerical modeling of the dbd plasma actuator.

[37] M. N. Shneider R. B. Miles A. V. Likhanskii D. F. Opaits, S. S. Zaidi and S. O. Macheret. Suppression of dielectric barrier discharge charge buildup using a partially conducting thin film. In *39th AIAA Fluid Dynamics Conference*, 2009.

[38] S. Guo and U. Kortshagen. Thrust enhancing designs for single dbd plasma actuators. *Bulletin of the American Physical Society*, 54, 2009.

[39] A. Bogaerts. Hybrid monte carlo–fluid modeling network for an argon/hydrogen direct current glow discharge. *Spectrochimica acta.Part B, Atomic spectroscopy*, 57(6):1071, 2002.

[40] A. Bogaerts. Computer simulations of argonhydrogen grimm-type glow discharges. *Journal of Analytical Atomic Spectrometry*, 23(11):1476, 2008.

[41] J. T. Gudmundsson. Ion energy distribution in h2/ar plasma in a planar inductive discharge. *Plasma sources science technology*, 8(1):58, 1999.

[42] U. R. Kortshagen. Generation and growth of nanoparticles in low-pressure plasmas. *Pure and applied chemistry*, 71(10):1871, 1999.

[43] F. Galli, M. Mamunuru, and U. R. Kortshagen. The energy distribution function of ions impinging on nanoparticles in a collisional low-pressure plasma. *Plasma Sources Science and Technology*, 21(3), 2012.

[44] M. C. Bordage G. J. M. Hagelaar W. L. Morgan A. V. Phelps S. Pancheshnyi, S. Biagi and L. C. Pitchford. The lxcat project: Electron scattering cross sections and swarm parameters for low temperature plasma modeling. *Chemical Physics*, 398(0):148–153, 4/4 2012.

[45] M. A. Lieberman. Dynamics of a collisional, capacitive rf sheath. *IEEE Transactions on Plasma Science*, 17(2):338, 1989.

[46] J. E. Allen. Probe theory-the orbital motion approach. *Physica Scripta*, 45(5):497, 2006.

[47] M. C. Schlamp V. L. Colvin and A. P. Alivisatos. Light-emitting diodes made from cadmium selenide nanocrystals and a semiconducting polymer. *Nature*, 370(6488):354–357, 1994.

[48] J. J. Dittmer W. U. Huynh and A. P. Alivisatos. Hybrid nanorod-polymer solar cells. *Science*, 295(5564):2425–2427, 2002.

[49] D. J. Norris V. Noireaux A. H. Brivanlou B. Dubertret, P. Skourides and A. Libchaber. In vivo imaging of quantum dots encapsulated in phospholipid micelles. *Science*, 298(5599):1759–1762, 2002.

[50] Uwe Kortshagen. Nonthermal plasma synthesis of semiconductor nanocrystals. *Journal of Physics D: Applied Physics*, 42(11):113001, 2009.

[51] U. V. Bhandarkar, M. T. Swihart, S. L. Girshick, and U. R. Kortshagen. Modelling of silicon hydride clustering in a low-pressure silane plasma. *Journal of Physics D: Applied Physics*, 33(21):2731, 2000.

[52] T. Hbid B. V. Potapkin AA Fridman, L. Boufendi and A. Bouchoule. Dusty plasma formation: Physics and critical phenomena. theoretical approach. *Journal of Applied Physics*, 79(3):1303–1314, 1996.

[53] C. R. Seon K. B. Chai, W. Choe and C. W. Chung. Role of hydrogen in evolution of plasma parameters and dust growth in capacitively coupled dusty plasmas. *Applied Physics Letters*, 97:201503, 2010.

[54] R. L. Naone D. C. Marra, E. A. Edelberg and E. S. Aydil. Silicon hydride composition of plasma-deposited hydrogenated amorphous and nanocrystalline silicon films and surfaces. *Journal of Vacuum Science Technology A: Vacuum, Surfaces, and Films*, 16(6):3199–3210, 1998.

[55] J. C. Knights. Effects of inert gas dilution of silane on plasmadeposited asi: H films. *Applied Physics Letters*, 38(5):331, 1981.

[56] M. J. Kushner. A model for the discharge kinetics and plasma chemistry during plasma enhanced chemical vapor deposition of amorphous silicon. *Journal of Applied Physics*, 63(8):2532–2551, 1988.

[57] Y. H. Wang. Structural and optical properties of a-si: H/nc-si: H thin films grown from ar-h2-sih4 mixture by plasma-enhanced chemical vapor deposition. *Materials science engineering.A, Structural materials: properties, microstructure and processing*, 104(1-2):80, 2003.

[58] K. Satake. Molecular dynamics simulation of ion bombardment on hydrogen terminated si (001) 2 1 surface. *Journal of vacuum science technology.A.Vacuum, surfaces, and films*, 21(2):484, 2003.

[59] M. Lampe. Limits of validity for orbital-motion-limited theory for a small floating collector. *Journal of plasma physics*, 65(3):171–180, 2001.

[60] M. Gatti. Analytical model of particle charging in plasmas over a wide range of collisionality. *Physical review.E, Statistical, nonlinear, and soft matter physics*, 78(4):046402, 2008.

[61] U. Kortshagen. Comparison of monte carlo simulations and nonlocal calculations of the electron distribution function in a positive column plasma. *Physical review.E, Statistical physics, plasmas, fluids, and related interdisciplinary topics*, 54(6):6746, 1996.

[62] Walter Guido Vincenti and Charles H. Kruger. Introduction to physical gas dynamics. *Introduction to physical gas dynamics, by Vincenti, Walter Guido; Kruger, Charles H.New York, Wiley [1965]*, 1, 1965.

[63] Peter Banks Banks. Collision frequencies and energy transfer electrons. *Planetary and Space Science*, 14(11):1085–1103, 1966.

[64] MA Islam. Einsteinsmoluchowski diffusion equation: a discussion. *Physica Scripta*, 70(2-3):120, 2004.

[65] M. S. Valipa. Hydrogen-induced crystallization of amorphous si thin films. ii. mechanisms and energetics of hydrogen insertion into sisi bonds. *Journal of Applied Physics*, 100(5):053515, 2006.